TYPICAL RESPONSE OF THE ADXRS300 MICROELECTROMECHANICAL SYSTEMS GYROSCOPE IN ACOUSTICALLY HARSH ENVIRONMENTS

Except where reference is made to the work of others, the work described in this thesis is my own or was done in collaboration with my advisory committee. This thesis does not include proprietary or classified information.

Simon Thomas Castro

Certificate of Approval:

George T. Flowers
Professor
Mechanical Engineering

Robert Dean, Chair
Assistant Professor
Electrical and Computer Engineering

Thaddeus Roppel
Associate Professor
Electrical and Computer Engineering

George T. Flowers
Dean
Graduate School

TYPICAL RESPONSE OF THE ADXRS300 MICROELECTROMECHANICAL SYSTEMS GYROSCOPE IN ACOUSTICALLY HARSH ENVIRONMENTS

Simon Thomas Castro

A Thesis

Submitted to

the Graduate Faculty of

Auburn University

in Partial Fulfillment of the

Requirements for the

Degree of

Master of Science

Auburn, Alabama
August 10, 2009

TYPICAL RESPONSE OF THE ADXRS300 MICROELECTROMECHANICAL SYSTEMS GYROSCOPE IN ACOUSTICALLY HARSH ENVIRONMENTS

Simon Thomas Castro

Permission is granted to Auburn University to make copies of this thesis at its discretion, upon the request of individuals or institutions and at their expense. The author reserves all publication rights.

Signature of Author

Date of Graduation

VITA

Simon Thomas Castro, son of Thomas Frank Castro and Elizabeth Ann Hawkins was born September 26, 1981, in Nacogdoches, Texas. He graduated from Robertsdale High School as Valedictorian in 2000. He attended Auburn University in Auburn, Alabama for five years from September 2000 to August 2005. During this time, he spent three semesters in the cooperative education program working for VT Miltope in Hope Hull, Alabama. He graduated magna cum laude with a Bachelor of Science degree in Electrical and Computer Engineering and a cooperative education degree. In September of 2006, he enrolled in the Auburn University graduate school where he has been studying MEMS-based gyros and microfabrication techniques.

THESIS ABSTRACT

TYPICAL RESPONSE OF THE ADXRS300 MICROELECTROMECHANICAL SYSTEMS GYROSCOPE IN ACOUSTICALLY HARSH ENVIRONMENTS

Simon Thomas Castro

Master of Science, August 10, 2009
(B.S., Auburn University–Auburn, 2005)

188 Typed Pages

Directed by Robert Dean

Microelectromechanical systems (MEMS)-based gyroscopes have become increasingly commonplace in the last decade or so. With improvements in manufacturing techniques, MEMS-based gyroscopes have improved in reliability, sensitivity, and cost. This has lead to an abundance of commercially available MEMS gyroscopes. With an increased presence in the marketplace, these gyros have been subjected to an ever expanding landscape of harsh environments. One such typical environment exists in the presence of powerful acoustic noise. It will be shown that such an environment can have a great impact on the gyro's electrical output responses. Of singular focus will be the Analog Devices, Inc. ADXRS300. The ADXRS300 is one of the most common commercial gyroscopes in the global market as of this writing. The electrical output response will be fully characterized while in the presence of acoustic noise to simulate several harsh real-life situations such as loud music concerts, rocket firing scenarios, missile guidance systems, etc.

In this thesis, the basic theory behind vibratory MEMS gyroscopes will be discussed to show how some of the design parameters originate. Also, a survey of commercially available MEMS gyros will be presented. In addition, a further survey of new developments

in MEMS gyros that are taking place today will be put forth. Furthermore, the methods for data extraction and sound level manipulation will be described. Next, the typical electrical output response to various sound pressure levels will be shown. Finally, trends in the data such as mean and standard deviation will be presented followed by conclusions and ideas for further work.

ACKNOWLEDGMENTS

The author would like to thank Dr. Robert Dean for his guidance, wisdom, and patience without which this thesis would not exist. Also, gratitude goes to Dr. George Flowers for his support and knowledge of acoustics and vibrations. In no small way, many thanks also go to Grant Roth, Ran Zhou, Brian Grantham, Mike Palmer, Charles Ellis, Dr. Anwar Ahmed, John Crawford, Justin Russell, Nesha Hyatt, and Advanced Circuits for their invaluable assistance. The unconditional love and support of my family and closest friends made this research possible by giving me an unfathomable amount of happiness. “Happiness is nothing if not shared...” and I owe all the people closest to me for making me who I am today. Lastly, I’d like to thank the entire Auburn Family for the seven best years of my life. War Eagle!

“The most exciting phrase to hear in science,
the one that heralds the most discoveries,
is not “Eureka!” (I found it!) but “That’s funny...””
∼Isaac Asimov

Style manual or journal used IEEE Standards Style Manual (together with the style known as “aums”).

Computer software used LabView 8.6, Matlab R2008A, PentaLogix ViewMaster 8.4, NCH Tone Generator 2.11, Microsoft Word 2003, Microsoft Excel 2003, and AutoHotKey 1.0.47.06 along with the document preparation package TEX (specifically LATEX) together with the departmental style-file `aums.sty`.

TABLE OF CONTENTS

LIST OF FIGURES

CHAPTER 1

INTRODUCTION

In today's fast evolving technology market, microelectromechanical systems (MEMS) gyroscopes are becoming everyday appliances for both the common consumer and state-of-the-art applications. There are many causes for this phenomenon, none of which should be overlooked. Miniaturization, low cost, improved reliability, increased sensitivity, and ease of implementation are all combining to make MEMS-based gyros one of the most exciting and beneficial technologies to appear in quite some time.

1.1 Where Are MEMS Gyros Found?

MEMS gyros are so prevalent in today's world that many people may not even realize how often they interact with such devices. For instance, GPS navigation systems in the latest automobiles all use MEMS gyros to help the navigation software determine the direction of travel when the GPS signal itself is weak. Furthermore, many luxury vehicles utilize stability control features to sense yaw, and compensate for over-steering and under-steering on a slick road surface [1].

In the aeronautics industry, MEMS gyros are used for missile guidance, flight navigation, and radar stabilization. Likewise, in the consumer electronics industry MEMS gyros are used for accurate electronic image stabilization in digital cameras and camcorders. Segway Scooters also utilize MEMS gyros to provide natural steering based on the passenger's body movements [1]. All these applications and others on the horizon are relatively recent developments and are thus becoming more and more important in this new millennium.

1.2 Gyroscopic History

In 1850, French Physicist, Jean Foucault, first utilized the ability of a rotor's spin axis to remain fixed in space in seeking a method to demonstrate that the earth rotated. Foucault also coined the word which we now designate devices based on the properties of a spinning rotor. He chose the word gyroscope from the Greek words "gyros," meaning rotation, and "skopein," meaning to view. Hence, the word gyroscope literally means "to view rotation" [2].

The traditional macroscale gyroscope is basically a mechanical device, the essential element of which is a flywheel rotating at high angular velocity about an axis. The flywheel is mounted within gimbals which allow it one or two degrees of freedom. Gyroscopes derive their basic applications from two inherent properties, namely precession and gyroscopic inertia [2]. Figure 1.1 shows a wheel's tendency to precess while rotating and attached to only one end of its axis.

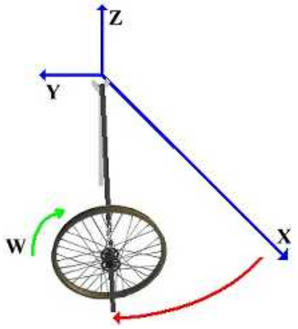

Figure 1.1: A Wheel's Tendency to Precess While Spinning

In other words, in its simplest form, the gyroscope is nothing more than a spinning top with both ends of its axis supported while allowing a platform to move [3]. A century ago these crude devices were used to steer torpedoes, steady vessels, travel along a single rail or on a wire, finding position at sea, proving the rotation of the earth, finding true North, and stabilizing planes [3].

1.3 Gyroscope Basics

The play top or the flywheel with its axle mounted to a fixed structure is the classic example of the gyroscopic effect [4]. When either device is spun with its axis out of the vertical, the device will appear to “rise” unaided. It will resist any attempt to make it fall, and seems never to respond to any external stimulus. In fact, the flywheel will look to be defying gravity if it is spun at a high enough angular velocity [4]. This is the essence of the gyroscopic effect.

Mathematically speaking, there are several fundamental relationships that describe the gyroscopic effect. One of the most important relationships, practically-speaking, is the relationship between precession (ϕ), the external moment (M), and the angular velocity of the spin (Ω). This relationships states that for a given external moment, the greater the spin velocity, the slower the precession. This is shown by the equation: $\Omega = \frac{M_y}{C\phi}$ where C is a constant [5]. Another fundamental relationship is that of angular momentum (H) and torque (M) of the gyroscope. The equation: $M = \frac{dH}{dt}$ describes this correlation [10]. A third common relationship is that of the single-axis rate gyroscope. This type of gyro is used to measure angular velocity. The fundamental equation for this gyro configuration is simply: $\alpha = -\frac{Cn}{k}\Omega$. Thus, when a platform is turned steadily about a single axis, the gimbal will adopt a steady-state deflection proportional to the rate of turn. This principle can be seen in aircraft turn-and-slip indicators, gunsights for tracking high-speed targets, stabilizing searchlights at sea, and anti-rolling devices on ships [11]. Many application specific design rules may be derived from these equations such as satellite attitude control, gyro blender phase stabilization, airplane propeller forces, optimally-balanced crankshafts, and even monorails [6][7][8][9][12]. The fundamental gyroscope equations are summarized in Equations 1.1 - 1.5.

$$\Omega = \frac{M_y}{C\phi} \tag{1.1}$$

$$M = \frac{dH}{dt} \tag{1.2}$$

$$\alpha = -\frac{Cn}{k}\Omega \tag{1.3}$$

$$H = I\omega \tag{1.4}$$

$$T = \frac{dH}{dT} + \Omega \tag{1.5}$$

A gyroscope as an inertial instrument is capable of sensing rotation in a number of ways. One such way was invented by Leon Foucault in 1852. This first gyroscope was based on the angular momentum of a spinning wheel. The angular momentum, H, is the product of the mass moment of inertia, I, and the angular velocity, ω, of the wheel: H = Iω. Due to Newton's laws of motion, the angular momentum of a body will remain unchanged unless acted on by a torque, T: T = $\frac{dH}{dT} + \Omega$ x H. If a torque is applied in the same axis as the angular velocity, the effect is to accelerate or decelerate the rotating body, which is denoted by the first term of the previous equation. However, if the torque is applied orthogonal to the spin axis, the rotating body will precess, Ω, denoted by the second term of the equation. These effects are illustrated in Figure 1.2 below.

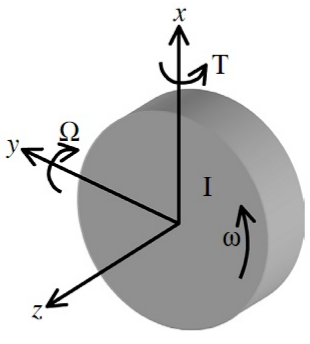

Figure 1.2: Precession of a rotating body

The cross-product in the second term generates the interesting gyroscopic effects (i.e., Ω, H, and T are related by the right-hand rule). Precession or the moments generated by precession are utilized by this form of gyroscope to measure angular rate. The spinning wheel gyroscope is used to implement a class of high-performance gyroscopes for inertial navigation as well as other lower performance applications. Because the fabrication of this type of gyroscope requires precision bearings, machining, drive motors, and electronics, it is very costly, large, and heavy. However, in the 1950's inertial navigation for missiles, aircraft, and submarines came to rely on this type of gyroscope [15].

1.4 Motivation For The Thesis

With advances in micromachining and other microfabrication techniques, the gyroscopes mentioned above were able to go from large, bulky devices with limited sensitivity to devices that are able to be implemented in integrated circuits sized packages with extremely high precision. This fact coupled with low costs has created a boom in MEMS-based gyroscope production.

One of the major differences between a traditional gyroscope and a MEMS gyro is the method of movement of the proof mass. In a traditional gyroscope, the proof mass was typically a spinning wheel or some such similar mechanical device. On the other hand, a MEMS gyro uses a high frequency vibration as a means to move the micro-sized proof mass. The frequency to which a proof tends to vibrate is called its natural frequency and is dependent on a number of factors which will be described later in the thesis. This natural frequency is often located in the acoustic spectrum which is from 0 to 20,0000 Hz.

Obviously, this could present a major problem. If a MEMS gyro finds itself in the presence of loud acoustic noise, it may artificially vibrate and cause the angular rate output to be erroneous. This could lead to system malfunction or complete failure of a desired objective.

For instance, imagine someone is trying to film a rock concert, a trip to Niagra Falls, or even a football game. If this person is using a digital camcorder with a MEMS gyro image stabilization feature, the resulting video could be completely ruined by the hardware ”stabilizing” the video when it was not necessary. A Segway scooter, GPS system, or dangerous-if-not-accurate rocket guidance system could be affected in a very similar manner. Each of these could fail in the presence of loud acoustic noise. This is one of the primary motivations of this thesis.

One of the most popular MEMS gyros on the market today is the Analog Devices ADXRSXXX-series of angular rate gyros. These gyros are used worldwide in an overwhelmingly large number of commercial, industrial, and military applications. This model was chosen as a basis for this thesis to be representative of a inexpensive, popular, commercially available MEMS gyro which could be ordered by anyone through Digi-Key, Newark, or many other common electronic supply retailers. Furthermore, a member of this ADI gyro family would be representative of the functionality of other types of low-cost commercially available MEMS gyros manufactured by other companies. As such, a complete evaluation of this product would benefit the large community of technical designers who are intimately familiar with it.

1.5 Thesis Statement

The primary purpose of this thesis is to present the results of a thorough evaluation of the Analog Devices ADXRS300 series angular rate gyro in a harsh acoustic environment. Before this is presented, a cursory review of vibratory MEMS gyroscopic theory will be presented. Then, a survey of commercially available MEMS gyros along with a survey of new MEMS gyro developments will be shown. Next, a detailed overview of the Analog Devices ADXRS300 will be presented. Furthermore, the performance of the ADXRS300 in the presence of acoustic noise will be presented with a discussion of the methods for data retrieval and analysis. Finally, the performance trends of the ADRXRS300 will presented with conclusions and further work.

CHAPTER 2

LITERATURE REVIEW OF MEMS GYROSCOPES

In this chapter, the general theory of vibratory MEMS gyroscopes will be presented. The fundamental principles and concepts of vibratory MEMS gyroscopes will be shown to gain needed background into the world of MEMS gyro design.

Next, a survey of commercially available MEMS gyroscopes will be presented along with some of their features and price points. These gyros will be examples of what consumers can expect to readily find when needed.

Finally, a detailed description of the Analog Devices ADXRS300 will be presented. This description will include a list of features, design elements, and other important characteristics of the device.

2.1 Theory Of Vibratory MEMS Gyroscopes

Vibratory gyroscopes are based on Coriolis acceleration, which is an acceleration produced due to the changing direction in space of the velocity of the body relative to the moving system. Another approach for rotation rate sensing lies in the dynamics of vibrating mechanical systems. The fact that vibrating objects are sensitive to rotation has been known since 1890 [15]. The initial concept for an implementable vibratory gyroscope was based on the vibration of a metal tuning fork [15]. By the 1960s, engineers were seeking alternatives to the spinning mass gyroscope due to its size, fragility, and expense. Subsequent technology developments enabled the realization of a functioning vibratory gyroscope. The vibratory gyroscope was also later discovered to be the mechanism utilized by biological systems such as a fly's ability to sense angular rotation [15].

2.1.1 Inertial Sensors

Micromachined inertial sensors can be classified into two groups: accelerometers and gyroscopes. Accelerometers measure translational acceleration along one or several axes. Gyroscopes measure angular velocity along one or several axes. The focus of this thesis is concentrated on micromachined gyroscopes. The first MEMS gyroscope was reported by Draper Labs in 1991 [13].

2.1.2 Principle of Operation

MEMS gyroscopes are based on a mechanical structure that forcibly resonates and excites a secondary oscillation in either the same structure or in a second one due to the Coriolis force. This is known as the Coriolis effect. The angular rate signal to be measured is directly proportional to the amplitude of this secondary oscillation [13]. All micromachined angular rate sensors have a vibrating element at their core. This is the moving body. In a frame of reference fixed to the body of the oscillating element, a point on this element oscillates with a certain velocity. If the frame of reference begins to rotate at a certain angular rate, this oscillating element is then subject to a Coriolis force and a corresponding acceleration [14].

Consequently, nearly all MEMS gyroscopes use a vibrating structure that couples energy from a primary, forced oscillation mode into a secondary, sense oscillation mode. In Figure 2.1, a lumped model of a simple gyroscope suitable for a micromachined implementation is shown.

The proof mass is excited to oscillate along the x-axis with a constant amplitude and frequency. Rotation about the z-axis couples energy into an oscillation along the y-axis

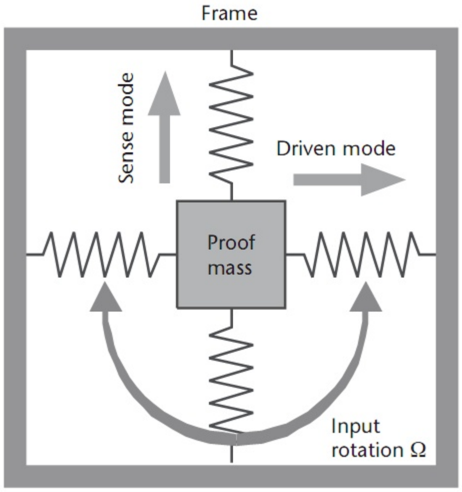

Figure 2.1: Lump model of a vibratory rate gyoscope

whose amplitude is proportional to the rotational velocity. Similar to closed loop micromachined accelerometers, it is possible to incorporate the sense mode in a force-feedback loop. Any motion along the sense axis is measured and a force is applied to counterbalance this sense motion. The magnitude of the required force is then a measure of the angular rate signal [13].

2.1.3 Coriolis Force and Acceleration

The Coriolis effect, named after the French physicist Gaspard Coriolis, manifests itself in numerous weather phenomena, including hurricanes and tornadoes, and is a direct consequence of a body's motion in a rotating frame of reference. Figure 2.2 below is an illustration of this phenomena in nature [14].

The Coriolis force is a force whose observability is dependent on the reference of the observer. The Coriolis acceleration that gives rise to a Coriolis force acts perpendicularly to the radial component of the velocity vector. Figure 2.3 below shows an example of this is action.

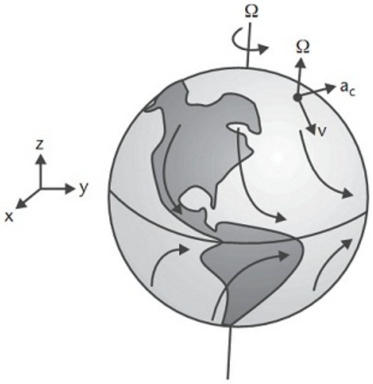

Figure 2.2: Rotion of the Earth

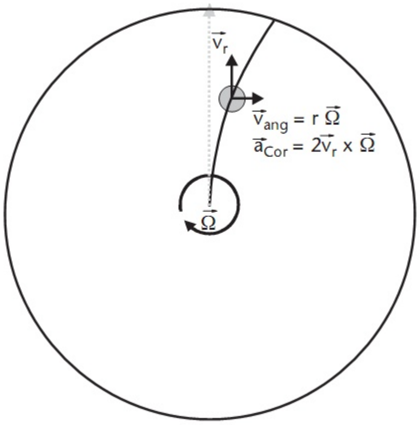

Figure 2.3: Curved trajectory of a ball rolling on a spinning disk

The Coriolis acceleration is given by: $\vec{a_C} = 2\Omega$ x $\vec{v_r}$. Likewise, the Coriolis force is given by: $F_C = 2m\Omega$ x $\vec{v_r}$ where F = m$\vec{a}$. The Coriolis Effect is summarized in Equations 2.1 - 2.4.

$$\vec{a_C} = 2\Omega\vec{v_r} \tag{2.1}$$

$$F_C = 2m\Omega\vec{v_r} \tag{2.2}$$

$$F = m\vec{a} \tag{2.3}$$

$$A_y = \frac{\Omega 2 A_d Q_y}{\omega_y} \tag{2.4}$$

For another example, Figure 2.4 shows the Coriolis acceleration, $\vec{a_C}$, produced on a body moving around an axis with a fixed angular velocity, Ω, and moving radially with a velocity $\vec{v_r}$ as well. The detection of the deflection of an object due to Coriolis acceleration is the basis for a vibratory gyroscope [15].

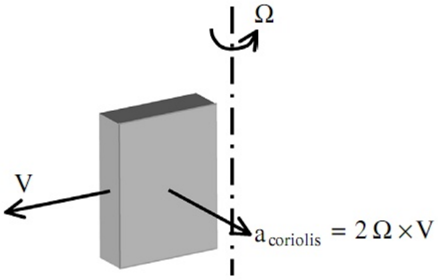

Figure 2.4: Coriolis acceleration on a moving body in a rotating system

2.1.4 Design

A vibratory gyroscope is composed of a resonator that will oscillate a body along one axis and measure the orthogonal movement or force on the body due to Coriolis acceleration. Figure 2.5 is a schematic of a plate being driven along the x-axis, the rotation rate to be measured; Ω is along the z axis and the Coriolis acceleration response is sensed along the y-axis. Although not indicated in the illustration, relative proof mass motion between the proof mass itself and the attached frame is limited to translational motion only. For a vibratory gyro, this results in a sinusoidal proof mass motion along the y-axis with an amplitude of $A_y = \frac{\Omega 2 A_d Q_y}{\omega_y}$.

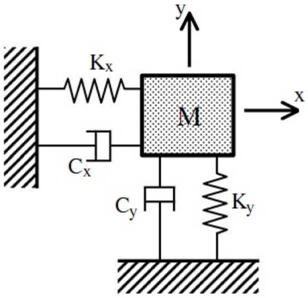

Figure 2.5: Single mass gyroscope schematic

The first two equations in Figure 2.6 show the equations of motion (force balance) for the body in the drive (x) and sense (y) axes, respectively. These are a system of coupled second-order equations coupled via Coriolis acceleration terms.

$$\ddot{x} + 2\zeta_x \omega_x \dot{x} + \omega_x^2 x = \frac{1}{M} F_x - 2\Omega \dot{y}$$

$$\ddot{y} + 2\zeta_y \omega_y \dot{y} + \omega_y^2 = 2\Omega \dot{x}$$

$$\omega_y = \sqrt{\frac{K_y}{M}} \qquad \omega_x = \sqrt{\frac{K_x}{M}}$$

Figure 2.6: Equations of motion and natural frequency

The physical mechanism for a vibratory gyroscope is the transfer of energy from one resonator axis to another via the Coriolis acceleration coupling. The suspension for this device can have a unique natural frequency, ω_x, ω_y and a unique damping ratio for ξ_x, ξ_y for each axis (equation 3 in Figure 2.6). The relative positioning of the proof mass-suspension system's natural frequencies is a gyroscope design decision. Frequently, the sense direction natural frequency, ω_y, is approximately 10 percent less than the drive direction natural frequency, ω_x. This will provide a modest mechanical gain without significant bandwidth or phase shift reductions. The damping ratio of the mass in the x and y axes depends on the orientation of the mass relative to the substrate, which will determine the damping mechanism involved (e.g., squeeze film vs. lateral shear damping). The implementation of the gyroscope will require the mass to be driven in the x axis by the force F_x. For many MEMS designs, F_x is electrostatic, such as an interdigitated electrostatic comb drive. The drive amplitude, x, must be maintained very accurately because any variation will directly contribute an error into the sense direction amplitude (equation 1 in Figure 2.6) and the gyroscope output. For this reason, the drive axis amplitude is controlled by an automatic gain control feedback loop. Because the oscillatory drive portion of the gyroscope (equation 1 in Figure 2.6) is fixed to a high degree of accuracy by the gain control loop, Equation 2 in Figure 2.6 governs the dynamics of the gyroscope response. Because the x-axis (drive axis) is an oscillator, the response of the y axis (sense axis) will also be oscillatory (equation 1 Figure 2.7).

$$x = Xe^{j\omega t} \qquad y = Ye^{j(\omega t + \varphi)}$$

$$\ddot{y} + \delta_M \ddot{x} + 2\zeta_y \omega_y \dot{y} + \omega_y^2 + \delta_K x = 2\Omega \dot{x}$$

Figure 2.7: X- and Y-axis oscillatory responses

The Coriolis term that is the input to equation 2 in Figure 2.6 is twice the product of the angular rate and the velocity of the x-axis oscillator, which produces a modulated signal. Therefore, the gyroscope output will need to be demodulated to extract the rotation rate signal. The velocity, $\dot{x}$, of the drive signal that is the input to the Coriolis term of equation 2 in Figure 2.6 is simple harmonic motion, which will be zero at the extremes of motion of the driven mass and a maximum as the mass passes through the undeflected position. The mass x displacement and the Coriolis force, which contains an x velocity term, have a 90 degree phase difference; therefore, the y displacement due to the Coriolis force will also have a 90 degree phase difference. These signals are said to be in quadrature. This will lead to an oval deflection path (symmetric about the x-axis) of the mass shown in Figure 2.8 when the gyroscope is subject to a constant rotation rate. With a zero rotation rate, the mass deflection pattern will not deflect in the y direction and oscillate entirely along the x-axis as shown in Figure 2.8. However, if mass or stiffness imbalances exist in the system dynamics as indicated in equation 2 of Figure 2.7, the mass deflection pattern will be as shown in Figure 2.8.

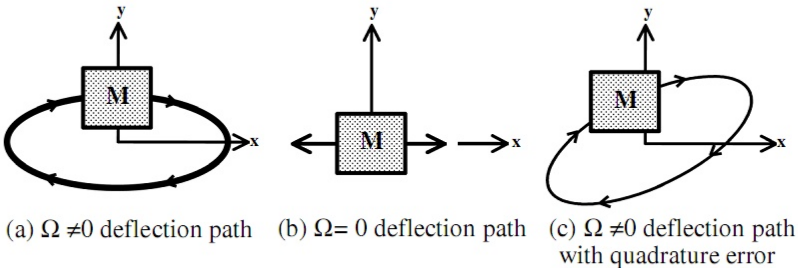

(a) $\Omega \neq 0$ deflection path (b) $\Omega = 0$ deflection path (c) $\Omega \neq 0$ deflection path with quadrature error

Figure 2.8: Gyroscope mass deflection response due to Coriolis acceleration

These subtle imbalances in the vibration of the sense mass produce a deflection in the y direction known as quadrature error, which contaminates the Coriolis force measurement signal, which is the measure of rotation rate. The effects of quadrature error can be minimized by a quadrature error cancellation scheme involving the use of electrostatic actuators with properly phased signals to cancel the imbalance, or by synchronous detection methods, which take advantage of the quadrature relationship to extract the Coriolis signal [15].

One problem is the relatively small amplitude of the Coriolis force compared to the driving force. Assuming a sinusoidal drive vibration given by $x(t) = x_0 \sin(\omega_d t)$, where x_0

is the amplitude of the oscillation and ω_d is the drive frequency, the Coriolis acceleration is given by a_C = 2v(t) x Ω = $2\Omega x_0 \omega_d$ cos (ω_dt). Using typical values of x_0 = 1 μm, Ω = 1 deg/s, and ω_d = 2π20 kHz, the Coriolis acceleration is only 4.4 mm/s^2. If the sensing element along the sense axis is considered as a second order mass-spring-damper system with a Q = 10, the resulting displacement amplitude is only 0.0003 nm. One way to increase the displacement is to fabricate sensing elements with a high Q structure and then tune the drive frequency to the resonant frequency of the sense mode. Very high Q structures, however, require vacuum packaging, making the fabrication process much more demanding. Furthermore, the bandwidth of the gyroscopes is proportional to ω_d/Q; hence, if a quality factor of 10,000 or more is achieved in vacuum, the bandwidth of the sensor is reduced to only a few Hz. Lastly, it is difficult to design structures for an exact resonant frequency, due to manufacturing tolerances. A solution is to design the sense mode for a higher resonant frequency than the drive mode and then decrease the resonant frequency of the sense mode by tuning the mechanical spring constant using electrostatic forces [13]. An acceptable compromise between bandwidth and sensitivity is to tune the resonant frequency of the sense mode close to the drive frequency (within 5 percent to 10 percent). A second fundamental problem with vibratory rate micromachined gyroscopes is due to the aforementioned so-called quadrature error. This type of error originates from manufacturing tolerances manifesting themselves as a misalignment of the axis of the driven oscillation from the nominal drive axis. As a result, a small proportion of the driven motion will be along the sense axis. Even though the misalignment angle is very small, due to the minute Coriolis acceleration, the resulting motion along the sense axis may be much larger than the motion caused by the Coriolis acceleration [13].

The vector cross product operation implies that the Coriolis acceleration and the resulting displacement at that point are perpendicular to the oscillation. This, in effect, sets up an energy transfer process from a primary mode of oscillation into a secondary mode that can be measured. It is this excitation of a secondary resonance mode that forms the basis of detection using the Coriolis effect. In beam structures, these two frequencies are distinct with orthogonal displacements. But for highly symmetrical elements, such as rings, cylinders, or disks, the resonant frequency is degenerate, meaning there are two distinct modes of resonance sharing the same oscillation frequency. This degeneracy causes the temporal excitation signal (primary mode) to be in phase quadrature with the sense signal (secondary mode), thus minimizing coupling between these two modes and improving sensitivity and accuracy [14]. Additionally, the degeneracy tends to minimize the device's sensitivity to thermal errors, aging, and long-term frequency drifts. A simple and common implementation is the tuning-fork structure (see Figure 2.9).

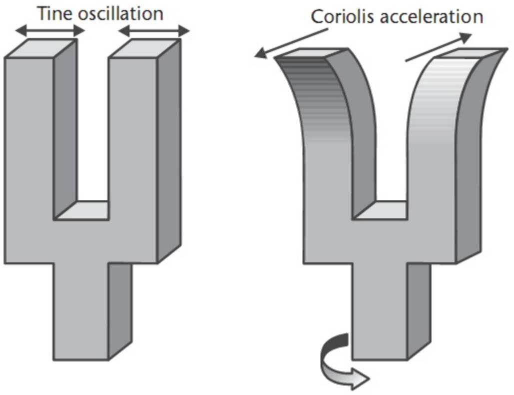

Figure 2.9: Tuning-fork structure for angular rate sensing

The two tines of the fork normally vibrate in opposite directions in the plane of the fork (flexural mode). The Coriolis acceleration subjects the tips to a displacement perpendicular to the primary mode of oscillation, forcing each tip to describe an elliptical path. Rotation, hence, excites a secondary vibration torsional mode around the stem with energy transferred from the primary flexural vibration of the tines. Quartz tuning forks such as those from BEI Technologies, Systron Donner Inertial Division of Concord, California, use the piezoelectric properties of the material to excite and sense both vibration modes.

The tuning-fork structure is also at the core of a micromachined silicon sensor from Daimler Benz AG that will be described later [14]. Other implementations of angular rate sensors include simple resonant beams, vibrating ring shells, and tethered accelerometers, but all of them exploit the principle of transferring energy from a primary to a secondary mode of resonance. Of all the vibrating angular-rate structures, the ring shell or cylinder is the most promising for inertial and navigational-grade performance because of the frequency degeneracy of its two resonant modes.

The main specifications of an angular-rate sensor are full-scale range (expressed in deg/s or deg/hr; scale factor or sensitivity [V/(deg/s)]; noise, also known as angle random walk [deg(s $\bullet$ $\sqrt{Hz}$)]; bandwidth (Hz); resolution (deg/s); and dynamic range (dB), the latter two being functions of noise and bandwidth. Short- and long-term drift of the output, known as bias drift, is another important specification (expressed in deg/s or deg/hr). As is the case for most sensors, angular-rate sensors must withstand shocks of at least 1,000 g. Micromachined angular-rate sensors have largely been unable to deliver a performance better than rate grade [14]. These are devices with a dynamic range of only 40 dB, a noise figure larger than 0.1 deg(s $\bullet$ $\sqrt{Hz}$), and a bias drift worse than 10 deg/hr. By comparison, inertial grade sensors and true gyroscopes deliver a dynamic range of over 100 dB, a noise less than 0.001 deg/(hr $\bullet$ $\sqrt{Hz}$), and a bias drift better than 0.01 deg/hr. The advantage of micromachined angular-rate sensors lies in their small size and low cost, currently less than 10 USD. They are slowly gaining acceptance in automotive applications, in particular, for vehicle stability systems. The sensor detects any undesired yaw of a vehicle due to poor road conditions and feeds the information to a control system, which may activate the antilock braking system (ABS) or the traction control system (TCS) to correct the situation. The Mercedes Benz ML series of sport utility vehicles incorporates a silicon angular rate sensor from Robert Bosch GmbH for vehicle stability [14].

2.1.5 Single-Axis MEMS Gyroscopes

Early micromachined gyroscopes were based on double-ended tuning forks. Two tines, which are joined at a junction bar, are excited to resonate in antiphase along one axis. Rotation causes the tines to resonate along the perpendicular axis. Different actuation mechanisms can be used to excite the primary or driven oscillation mode. Electromagnetic actuation have the advantage that large oscillation amplitudes are easily achievable. A severe disadvantage, however, is that it requires a permanent magnet to be mounted in close proximity to the sensing element, thereby making the fabrication process not completely compatible with that of batch processing [13]. Piezoelectric excitation has also been reported, for example, by Voss., who realized a double-ended tuning fork structure with the oscillation direction perpendicular to the wafer surface using bulk micromachining. The prevailing approach for prototype gyroscopes, however, is to use electrostatic forces to excite the primary oscillation. For detecting the secondary or sense oscillation, different position measurement techniques have been used such as piezoresistive, tunneling current, optical, and capacitive, the latter being by far the predominant method. Greiff from the Charles Stark Draper Laboratories presented a tuning fork sensor that can be regarded as one of the first micromachined gyroscopes suitable for batch-processing [13].

The two-gimbal structure is supported by torsional flexures. The outer gimbal structure is driven into oscillatory motion at 3 kHz out of the wafer plane by electrostatic forces. An automatic gain control (AGC) control loop ensures that the oscillation amplitude is constant. In the presence of a rotation about the axis normal to the sensing element plane, energy is transferred to the inner gimbal structure, which starts vibrating at the same frequency at an amplitude proportional to the angular spin rate. Maximum sensitivity is achieved when the drive frequency of the outer structure is equal to the resonant frequency of the inner gimbal. The sensing element could be operated in a force-balance mode. Electrostatic forces generated by voltages on the feedback electrodes counterbalance the movement of the inner gimbal. The fixed electrodes above the inner and outer gimbal structure were fabricated by an EDP wet-etch that removes sacrificial silicon dioxide. The lower electrodes underneath the structure were implemented as p-type buried electrodes and are electrically isolated by a reverse biased p-n junction from the substrate. The gap between the fixed electrodes and the movable electrodes on the resonators is between 8 and 10 μm. To increase the mass of the inner resonator, an inertial mass made from gold, of 25 μm height, was electroformed. The first polysilicon surface-micromachined vibratory rate gyroscope was presented in 1996 by Clark and Howe [13]. It is a direct implementation of the lumped model presented in Figure 2.1. Standard comb drive actuators were used to excite the structure to oscillate along one in-plane axis (x-axis), which allows relatively large drive amplitudes. Any angular rate signal about the out-of-plane axis (z-axis) excites a secondary motion along the other in-plane axis (y-axis). The sensing element consists of a 2 μm thick polysilicon structure.

In this reference, quadrature error is discussed in detailed and it is shown that a misalignment of the primary oscillation axis with the ideal x-axis of only one part in 3.6 million will result in a quadrature error equal to the signal of a 1 deg/sec rotation about the z-axis. No fabrication process can be accurate to such a degree, and hence, electrostatic tuning is used to alleviate this problem. The quadrature error is proportional to the position of the primary oscillation, whereas the Coriolis acceleration is proportional to the velocity of the primary oscillation; hence, the resulting forces are 90 degrees out of phase (this explains the term quadrature error). The inner interdigitated electrodes of the mechanical structure are used to exert an electrostatic force, which is proportional to the position of the primary oscillation. Applying a biasing voltage, together with a small differential voltage, results in an electrostatic force that allows counterbalancing of the unwanted motion of the proof mass of the primary oscillation due to quadrature error. The paper also discusses the required interface and control electronics for sustaining a constant amplitude and primary frequency oscillation. For the latter, a phase-locked loop is chosen; for the former an automatic gain control circuit is used. Furthermore, it is possible to tune the resonant frequencies of the primary and secondary oscillation modes by applying electrostatic negative springs. As a good compromise between bandwidth and sensitivity, a mismatch of about 5 percent to 10 percent is suggested. Another surface-micromachined gyroscope was presented by Geiger [13]. It was manufactured using the Bosch foundry process, which features a polycrystalline structural layer with a thickness of 10.3 μm. This relatively large thickness for a surface-micromachined process is achieved by epitaxial deposition of silicon. Under the freestanding structures a second thinner layer of polycrystalline silicon is used for electrodes and as interconnects. The sensing element has two decoupled rotary oscillation modes.

The primary drive mode is around the z-axis and is excited with electrostatic forces using the inner spoke electrodes of the inner wheel. Attached to the inner wheel, by torsional springs, is a rectangular structure, which, in response to rotation about the sensitive axis (x-axis), will exhibit a secondary rotary oscillation about the y-axis. Owing to the high stiffness of the suspension beam in this direction, the oscillation of the inner wheel is suppressed and only the rectangular structure can move due to a Coriolis force. With this approach the primary and secondary modes are mechanically decoupled, which suppresses mechanical cross-coupling effects such as quadrature error. The oscillation of the secondary mode is detected capacitively by electrodes on the substrate. The sensor reported a dynamic range of 200 deg/sec, a scale factor of 10 mV/(deg/sec), and a RMS noise of 0.05 deg/sec in a 50 Hz bandwidth, which makes it suitable for most automotive applications. Another popular implementation of a micromachined gyroscope, based on a single oscillating structure with two vibrating modes [13].

It is based on a ring supported by a number of semicircular springs and anchored in the middle. The ring is excited to vibrate electrostatically in-plane, the vibration having an elliptic shape. Any rotation about the axis normal to the ring structure transfers energy to a secondary mode, which is 45 degrees apart from the primary mode. In other words, the antinodes of the primary flexural mode are located at the nodes of the secondary flexural mode. Electrodes placed at these positions are used to capacitively measure the amplitude of the secondary mode, which is proportional to the angular rate to be measured. An obvious advantage of this design is the high degree of symmetry of the sensing element. An early version was presented by Putty and Najafi in 1994 [13]. It relied on a nickel electroplated ring structure, which was fabricated on a wafer containing standard CMOS circuitry for the control and interface electronics. Subsequently, this group presented more advanced versions of this approach. Another electroplated ring gyroscope was presented by Sparks, which mainly improved the signal and interface circuitry [13]. More recently, improved designs have been reported based on a high aspect ratio ring made from polysilicon [13]. The fabrication relies on the deep reactive dry etching of 50 μm- to 100 μm-deep trenches with near vertical sidewalls into a low-resistive silicon substrate. The trenches are subsequently refilled with highly doped polysilicon over a sacrificial silicon dioxide layer. After various patterning and etching steps of the oxide and the structural polysilicon, the sacrificial oxide is removed by a HF etch step to free the ring structure and form the air gaps between the electrodes and the ring. The ring is 1.1 mm in diameter, the support post in the middle has a diameter of 120 μm, and the width of the ring and support springs is 4 μm. Sixteen fixed electrodes are evenly located around the periphery of the ring; they are 60 μm tall, 150 μm long, and are separated from the ring by a 1.4-μm air gap. The fabrication technology has the advantage that the height of the ring structure and the electrodes can be made in the order of a hundred or more microns and the air gaps can be made in the submicron range. This results in high values of capacitance for vibration measurements;

thus, the sensitivity is increased considerably. The fabrication process also allows large air gaps, which can be used to excite the structure in the primary mode with high amplitude, again resulting in higher sensitivity. There is, however, a trade-off between the higher voltages required to electrostatically drive the ring using larger air gaps. Test results were reported for a structure 80 μm tall, operated at a low pressure (1 mTorr), which resulted in a quality factor for the oscillation of 1,000 to 2,000. This was lower than expected and was attributed to anchor losses and voids inside the polysilicon beams. Improved designs were expected to have a quality factor of up to 20,000. Similar to other micromachined gyroscopes, the resonant frequencies of drive and sense modes were designed to be equal in order to amplify the sense mode amplitude by the quality factor. Both resonant frequencies had a nominal value of 28.3 kHz. Any mismatch due to fabrication tolerances can be electrostatically tuned by applying suitable voltages to the electrodes around the periphery of the ring. A 63 Hz mismatch was observed between the sense and drive modes, which required a tuning voltage of only 0.9V. Other prototypes had a higher mismatch of up to 1 kHz for which a tuning voltage of 6V was required to match sense and drive mode resonant frequencies. The resolution of the device was measured to be less than 1 deg/sec for a 1 Hz bandwidth; however, with some changes in the interface circuitry this should be reduced to 0.01 deg/sec, which is then limited by the Brownian noise floor of the structure [13].

2.1.6 Dual-Axis Gyroscopes

It is also possible to design micromachined gyroscopes that are capable of sensing angular motion about two axes simultaneously. These devices are based on a rotor-like structure that is driven into a rotary oscillation by electrostatic comb-drives. Angular motion about the x-axis causes a Coriolis acceleration about the y-axis, which, in turn, results in a tilting oscillation of the rotor. Similarly, any rotation of the sensor about the x-axis causes the rotor to tilt about the x-axis.

An implementation of such a dual-axis gyroscope was reported by Junneau [13]. It was manufactured in a surface-micromachining process with a 2 μm thick proof mass. The interface and control electronics were integrated on the same chip. Underlying pie-shaped electrodes capacitively detect the tilting motion. To distinguish the two different output modes, a different voltage modulation frequency (200 and 300 kHz) is used for each sense electrode pair. The reported performance was 1 deg/sec in a 25 Hz bandwidth. The natural driving frequency of the rotor is about 25 kHz. Similar to single-axis devices, a high quality factor can be used to amplify the output motion. In a 60 mTorr vacuum, Junneau et al. report a quality factor of about 1,000. Electrostatic tuning of the different resonant frequencies can be used [13]. Cross-coupling between the two output modes is a major problem and was measured to be as high as 15 percent. This implies that for a commercially viable version, more research has to be done for such a dual-axis gyroscope. A conceptually similar implementation was reported by An [13]. The authors reported a higher resolution, of 0.1 deg/sec, which was mainly due to a thicker proof mass (7 μm) [13].

2.2 Survey of Commercially Available MEMS Gyroscopes

Here is brief survey of commercially available MEMS gyroscopes in the industry today. Product lines from the following companies will be considered: Analog Devices, Robert Bosch GmbH, Silicon Sensing, BEI Systron Donner, Melexis, InvenSense, Honeywell, Gladiator Technologies, Delphi Delco, Daimler-Benz, Northrop Grumman, NEC-Tokin, and GyroOptics.

2.2.1 Analog Devices (http://www.analog.com/)

The company has recently introduced the ADXRS family of integrated angular rate-sensing gyros, in which the mass is tethered to a polysilicon frame that allows it to resonate in only one direction. Capacitive silicon sensing elements interdigitated with stationary silicon beams attached to the substrate measure the Coriolis-induced displacement of the resonating mass and its frame [16].

One of these products is the ADXRS610 300 deg/sec Yaw Rate Gyro. This sensor is an electrostatically resonated surface micromachined polysilicon rate gyro with integrated electronics. The actual mechanical structure utilizes two resonating microstructure to cancel common mode effects, such as translational acceleration. This particular model has a measurement range of +/- 300 deg/sec and is intended for automotive and other applications. The proof mass structures are resonated at approximately 14 KHz, which is in the audio frequency range. The measurement bandwidth can be tuned over the range of 0.01 Hz to 2500 Hz. The sensor can be calibrated to achieve an accuracy of 40 deg/hour or better, with a typical rate noise density of 0.05 deg/sec/root(Hz). This sensor also includes built is self test (BIST) functions and is available in a BGA package [23].

2.2.2 Robert Bosch GmbH (http://www.bosch.com/)

Robert Bosch has been very active in the design and fabrication of silicon vibratory gyroscopes. They currently control 50 percent of the gyro market for the automotive industry and related applications. Bosch has developed both Z axis and X/Y axis rate sensors. Its Z-axis design was introduced in 1998 and uses electromagnetic drive with capacitive sensing.

The X/Y-axis gyro is a rotary vibrating mass. The MEMS sensor element along with its custom ASIC and all the discrete components are packaged in a hermetically sealed metal can which is then placed inside its automotive style plastic housing with integral connectors and mounting brackets [16].

This sensor is unique in its implementation of a mechanical resonant structure equivalent to a tuning fork. An oscillator system consists of two identical masses coupled to each other by a spring and suspended from an outer frame by two other springs.

Such a coupled system has two resonant frequencies: in phase, and out of phase. In the in-phase oscillation mode, the instantaneous displacements of the two masses are in the same direction. In the out-of-phase mode, the masses are moving, at any instant, in opposite directions. A careful selection of the coupling spring provides sufficient separation between the in-phase and out-of-phase resonant frequencies. Lorentz forces generated by an electric current loop within a permanent magnetic field excite only the out-of-phase mode. The oscillation electromagnetically induces a voltage in a second current loop that provides a feedback signal proportional to the velocity of the masses. The resulting Coriolis forces on the two masses are in opposite directions but orthogonal to the direction of oscillation. Two polysilicon surface-micromachined accelerometers with capacitive comb structures (similar in their basic operation to the Analog Devices ADXL family of sensors) measure the Coriolis accelerations for each of the masses. The difference between the two accelerations is a direct measure of the angular yaw rate, whereas their sum is proportional to the linear acceleration along the accelerometer's sensitive axis. Electronic circuits perform the addition and subtraction functions to filter out the linear acceleration signal. For the Bosch sensor, the out-of-phase resonant frequency is 2 kHz, and the maximum oscillation amplitude at this frequency is 50 μm. The measured quality factor of the oscillator at atmospheric pressure is 1,200, sufficiently large to excite resonance with small Lorentz forces. The stimulated oscillation subjects the masses to large accelerations reaching approximately 800G. Though they are theoretically perpendicular to the sensitive axis of the accelerometers, in practice, some coupling remains, which threatens the signal integrity.

However, because the two temporal signals are in phase quadrature, adopting synchronous demodulation methods allows the circuits to filter the spurious coupled signals with a rejection ratio exceeding 78 dB. This is indeed a large rejection ratio, but it is still insufficient to meet the requirements for inertial navigation. The peak Coriolis acceleration for a yaw rate of 100 deg/s is only 200 mG. This requires extremely sensitive accelerometers with compliant springs. The small Coriolis acceleration further emphasizes the need for perfect orthogonality between the sense and excitation axes. Closed-loop position feedback of the acceleration sense element compensates for the mechanical poles and increases the bandwidth of the accelerometers to over 10 kHz. The fabrication process simultaneously encompasses bulk and surface micromachining: the former to define the masses and the latter to form the comb-like accelerometers.

The process sequence begins by depositing a 2.5 μm layer of silicon dioxide on a silicon substrate. Epitaxy over the oxide layer grows a 12 μm thick layer of heavily doped n-type polysilicon. This layer forms the basis for the surface-micromachined sensors and is polycrystalline because of the lack of a seed crystal during epitaxial growth. In the next step, aluminum is deposited by sputtering and patterned to form electrical interconnects and bond pads. Timed etching from the back side using potassium hydroxide (KOH) thins the central portion of the wafer to 50 μm. Two sequential DRIE steps define the structural elements of the accelerometers and the oscillating masses. The following step involves etching the sacrificial silicon dioxide layer using a gas phase process (e.g., hydrofluoric acid vapor) to release the polysilicon comb structures. Finally, a protective silicon cap wafer that contains a recess cavity is bonded on the front side using a low temperature seal glass process. A glass wafer anodically bonded to the back side seals the device. The final assembly brings together the silicon sensor and the electronic circuits inside a metal can whose cover holds a permanent magnet. The sensitivity of the device is 18 mV/(deg/s) in the range of +/- 100 deg/s over 40 to +85 degrees C. The temperature dependence of the uncompensated sensor causes an offset amplitude of 0.5 deg/s over the specified temperature range, but signal conditioning circuits reduce this dependence by implementing appropriate electronic temperature compensation schemes [14].

Their most current product, the SMG040, is a micromachined angular rate sensor especially designed for roll-over automobile applications.

The sensor is based upon a two-chip concept: the micromachined sensing element and a separate evaluation ASIC. The sensing element is an oscillating polysilicon mass with the sensitive axis lying in the chip plane. The micromachined structure is sealed under vacuum at wafer level. The Sensor chip and read-out ASIC are packaged in a standard PLCC44 package. The sensing element has a symmetrical layout with only one suspension at the pivot point. By applying electrostatic forces to comb structures, the mass is forced to a rotational oscillation around this pivot point in the center of the mass. This oscillation is stabilized by an electronic control loop (drive control loop) [17].

2.2.3 Silicon Sensing (http://www.siliconsensing.com/)

Silicon Sensing Systems is a joint venture between Sumitomo and British Aerospace. They have brought to market an electromagnetically driven and sensed MEMS gyro with a permanent magnet that sits above the MEMS device. Current passing through the conducting legs creates a force that resonates the ring. This Coriolis-induced ring motion is detected by induced voltages as the legs cut the magnetic field [16].

Silicon Sensing Systems has also launched two new silicon MEMS angular rate sensors, the CRG20 and CRS09, which are based on a patented silicon ring gyro technology.

Derived from technology used in the automotive industry, the CRG20 device uses full digital closed-loop control, which the supplier claimed can eliminate any temperature and aging effects associated with analog devices. There is also built-in temperature compensation. The CRS09 angular rate sensor is targeted at applications such as stabilization, navigation and testing. It uses a combination of a silicon MEMS gyro and discrete electronics. The device's temperature stability combined with a provision of both internal temperature and silicon ring frequency data as additional outputs allow for very accurate calibration of the gyro over its operating temperature range. CRS09 is suitable for platform stabilization, measurement and test, and high-performance general aviation applications [18].

The CRS family of yaw-rate sensors from Silicon Sensing Systems, a joint venture between BAE Systems of Plymouth, Devon, England, and Sumitomo Precision Products Company of Japan, is aimed at commercial and automotive applications. It also uses a vibratory ring shell similar to the sensor from Delphi Delco but differs on the excitation and sense methods. Electric current loops in a magnetic field, instead of electrostatic electrodes, excite the primary mode of resonance. These same loops provide the sense signal to detect the angular position of the vibration pattern.

The ring, 6 mm in diameter, is suspended by eight flexural beams anchored to a 10-mm-square frame. Eight equivalent current loops span every two adjacent support beams. A current loop starts at a bond pad on the frame, traces a support beam to the ring, continues on the ring for one eighth of the circumference, then moves onto the next adjacent support beam, before ending on a second bond pad. Under this scheme, each support beam carries two conductors. A Samarium-Cobalt permanent magnet mounted inside the package provides a magnetic field perpendicular to the beams. Electromagnetic interaction between current in a loop and the magnetic field induces a Lorentz force. Its radial component is responsible for the oscillation of the ring in the plane of the die at approximately 14.5 kHz, which is the mechanical resonant frequency of the ring. The sensing mechanism measures the voltage induced around one or more loops in accordance with Faraday's law: As the ring oscillates, the area of the current loop in the magnetic flux changes, generating a voltage.

Two diametrically opposite loops perform a differential voltage measurement. One can simplistically view an actuating and a sensing loop as the primary and secondary windings of a transformer; the electromagnetic coupling between them depends on the ring vibration pattern and thus on the angular rate of rotation. Closed-loop feedback improves the overall performance by increasing the bandwidth and reducing the system's sensitivity to physical errors. Two separate feedback loops with automatic gain control circuits maintain a constant oscillation amplitude for the primary mode of resonance and a zero amplitude for the secondary resonance mode. The feedback voltage required to null the secondary mode is a direct measure of the rate of rotation. The fabrication of the sensor is relatively simple. A silicon dioxide layer is deposited on a silicon wafer, then lithographically patterned and etched. The silicon dioxide layer serves to electrically isolate the current loops. A metal layer is sputter deposited, patterned, and etched to define the current loops as well as the bond pads. A layer of photoresist is spun on and patterned in the shape of the ring and support flexural beams. The photoresist then serves as a mask for a subsequent DRIE step to etch trenches through the wafer. After removal of the photoresist mask, the silicon wafer is anodically bonded to a glass wafer with a previously defined shallow cavity on its surface. Little is available in the open literature on the packaging, but it is clear from the need to include a permanent magnet that the packaging is custom and specific to this application. The specification sheet of the CRS03-02 gives an output scale factor of 20 mV/(deg/s) with a variation of +/- 3 percent over a temperature range from 40 degrees to +85 degrees C. The noise is less than 1 mV rms from 3 to 10 Hz. The nonlinearity in a rate range of +/- 100 deg/s is less than 0.5 deg/s. The operating current is relatively large: 50 mA at a nominal 5 V supply [14].

Another Silicon Sensing model uses magnetic actuation and detection, which may prove to be problematic for further device size reduction. The ring has a diameter of 6 mm and is connected by eight radially compliant spokes to a support frame with the dimensions of 10 x 10 mm. It is fabricated by deep reactive ion etching of a 100 μm thick silicon wafer. Current-carrying conductor loops are deposited on the surface of the ring structure. These loops, together with the magnetic field, set up by the permanent magnet provide the signal pick-off and primary oscillation mode drive. This gyroscope has a resolution of 0.005 deg/sec, a bandwidth of 70 Hz, and a noise floor of 0.1 deg/sec/$\sqrt{Hz}$ in a 20 Hz bandwidth.

Currently, they are developing a capacitive sensor without a permanent magnet, thereby allowing for further size reduction [13].

2.2.4 BEI Systron Donner (http://www.systron.com/)

BEI Systron Donner is a major manufacturer of rate sensors for automotive applications. Their gyroscope design is based on using a one-piece quartz inertial sensor. These micromachined inertial sensing elements measure angular rotational velocity, using tuning fork vibratory principals and piezoelectric actuation and sensing. These sensors generate a signal output proportional to the rate of rotation sensed. Each sensor element is packaged in a hermetically sealed metal header which is then combined with discrete electronic to produce the finished modules products [16].

Systron Donner's family of quartz inertial sensors use a one piece, micromachined inertial sensing element to measure angular rotational velocity. These sensors produce a signal output proportional to the rate of rotation sensed. SDI's unique quartz inertial sensors are micromachined using photolithographic processes, and are at the forefront of MEMS (Micro Electro-Mechanical Systems) technology. These processes are similar to those used to produce millions of digital quartz wristwatches each year. The use of piezoelectric quartz material simplifies the sensing element, resulting in exceptional stability over temperature and time, and increased reliability and durability. The GyroChip uses vibrating quartz tuning tines to sense angular rate, acting as a Coriolis sensor, coupled to a similar fork as a pickup to produce the rate output signal. Each comprised of a pair of tuning forks, the GyroChip along with their support flexures and frames are batch fabricated from thin wafers of single-crystal piezoelectric quartz. The piezoelectric drive tines are driven by an oscillator to vibrate at a precise amplitude, causing the tines to move toward and away from one another at a high frequency. This vibration causes the drive fork to become sensitive to angular rate about an axis parallel to its tines, defining the true input axis of the sensor. Vibration of the drive tines causes them to act like the arms of a spinning ice skater, where pulling them in causes the skater's spin rate to increase, and pushing them out causes a decrease in rate. For vibrating tines (”arms”), an applied rotation rate causes a sine wave of torque to be produced, resulting from the oscillating torque at the frequency of the drive tines, in turn causing the tines of the pickup fork to move up and down (not toward and away from one another) out of the plane of the fork assembly. The pickup tines thus respond to the oscillating torque by moving in and out of plane, causing electrical output signals to be produced by the Pickup Amplifier. Those signals are amplified and converted into a DC signal proportional to rate by use of a synchronous switch (demodulator) which responds only to the desired rate signals. The DC output signal of the GyroChip is directly proportional to input rate, reversing sign as the input rate reverses, since the oscillating torque produced by the Coriolis force reverses phase when the input rate reverses [19].

2.2.5 Melexis (http://www.melexis.com/)

Melexis of Belgium recently has developed a MEMS angular rate sensor for use with GPS navigation systems. The gyroscope works in tandem with an electronic magnetometer (compass) to ensure vehicle position even when the GPS signal is lost. The system computes the direction, speed, and angular rate of the vehicle and maps this to the navigation software. The compass essentially ”zeros” the gyro to ensure proper initial heading after GPS signal is lost. The MLX90609 Angular Rate Sensor is a full gyroscopic system.

A single SMD package contains a high performance silicon micro-machined sensor with signal conditioning circuitry. It operates from 5V supply and is designed for demanding automotive applications. The MLX90609 delivers two output signals proportional to the angular rate parallel to the assembly surface. One of the output signals is in an analog voltage format (the output is 2.5V at zero angular rate and the full scale angular rate produces an output of 4.5V or 0.5V depending on direction of rotation) and the other one is in a digital SPI format [20].

2.2.6 InvenSense (http://www.invensense.com)

InvenSense provides motion sensing solutions for mobile applications. The company's patented motion sensing technology and its novel Nasiri-Fabrication addresses many emerging mass-market applications such as gaming, image stabilization, and smart user interfaces that use hand motion and gesture-based commands for mobile applications, such as smart phones, digital cameras, and 3D remote control devices. Their IDG-600 multi-axis MEMS rate gyroscope has started shipping in mass production quantities to Nintendo for its Wii MotionPlus accessory.

The addition of InvenSense's multi-axis rate gyroscope solution to the Wii MotionPlus accessory allows high precision 3D tracking of rapid gaming gestures. InvenSense pioneered its patented manufacturing platform, known as Nasiri-Fabrication, which enabled the company to bring the world's first and smallest integrated multi-axis gyroscopes to consumer products. Using Nasiri-Fabrication allows for the integration of MEMS and CMOS structures at the wafer level with a proprietary bonding technology resulting in several thousand gyroscopes simultaneously produced on a single wafer [21].

2.2.7 Honeywell(http://www.honeywell.com/)

The Honeywell GG5200 MEMS Rate Gyro Package is a two axis inertial sensor product for seeker stabilization, antenna pointing, gun/turret stabilization, and flight controls. The Honeywell GG5300 MEMS Rate Gyro Package is a three axis inertial sensor product [22].

This device has a specified angle random walk of 0.2 deg/root(Hr).

2.2.8 Gladiator Technologies (http://www.gladiatortechnologies.com/)

The G50Z High Performance Single Axis Gyro is a MEMS rate sensor.

Designed for commercial stabilization and aircraft applications, the unit utilizes standard +5V DC power and has a voltage output. The -200 model features a +/- VSG compatible signal. The signature features of the G50Z are low noise, impressive bias over temperature performance, low power consumption, excellent g-sensitivity and light weight. The unit is highly durable and can withstand environmental vibration and shock typically associated with commercial aircraft requirements. The unit has no inherent wear-out modes for long life and the rate output is also free from bias steps. The MEMS G50Z offers a standard angular rate range of +/- 20, 100, 175 or 350 deg/sec. Other angular rate ranges are available. The G50Z is designed for automotive testing, commercial aircraft applications, platform and antenna stabilization and pointing, and general aviation.

2.2.9 Delphi Delco (http://www.delphi.com/)

The sensor from Delphi Delco Electronics Systems of Kokomo, Indiana [29], a division of Delphi Corporation of Troy, Michigan, includes at its core a vibrating ring shell based on the principle of the ringing wine glass discovered in 1890 by G. H. Bryan. He observed that the standing-wave pattern of the wine glass did not remain stationary in inertial space but participated in the motion as the glass rotated about its stem. The complete theory of vibrating-ring angular-rate sensors is well developed [30]. The ring shell, anchored at its center to the substrate, deforms as it vibrates through a full cycle from a circle to an ellipse, back to a circle, then to an ellipse rotated at right angles to the first ellipse, then back to the original circle.

The points on the shell that remain stationary are called nodes, whereas the points that undergo maximal deflection are called antinodes. The nodes and antinodes form a vibration pattern or standing-wave pattern around the ring. The pattern is characteristic of the resonance mode. Because of symmetry, a ring shell possesses two frequency-degenerate resonant modes with their vibration patterns offset by 45 degrees with respect to each other. Hence, the nodes of the first mode coincide with the antinodes of the second mode. The external control electronics excites only one of the two modes, the primary mode. But under rotation, the Coriolis effect excites the second resonance mode, and energy transfer occurs between the two modes. Consequently, the deflection amplitude builds up at the antinodes of the second mode. The overall vibration becomes a linear combination of the two modes with a new set of nodes and antinodes forming a vibration pattern rotated with respect to the pattern of the primary mode. It is this lag that Bryan heard in his spinning wine glass. In an open-loop configuration, the deflection amplitude at the nodes and antinodes is a measure of the angular rate of rotation. Alternatively, the angular shift of the vibration pattern is another measure. In a closed-loop configuration, electrostatic actuation by a feedback voltage applied to the excitation electrodes nulls the secondary mode and maintains a stationary vibration pattern. The angular rate becomes directly proportional to this feedback voltage. A total of 32 electrodes positioned around the suspended ring shell provide the electrostatic excitation drive and sense functions. Of this set, eight electrodes strategically positioned at 45 degrees intervals, at the nodes and antinodes, capacitively sense the deformation of the ring shell. Appropriate electronic circuits complete the system control functions, including feedback. A phased-locked loop (PLL) drives the ring into resonance through the electrostatic drive electrodes and maintains a lock on the frequency. Feedback is useful to electronically compensate for the mechanical poles and increase the closed-loop bandwidth of the sensor. Additionally, a high mechanical quality factor increases the closed-loop system gain and sensitivity. The fabrication process is similar to the electroplating and molding process described in Chapter 3, except that the substrate includes preprocessed CMOS control circuitry. The mold is made of photoresist, and the electroplated nickel ring shell is 15 to 50 μm thick. Finally, packaging is completed in vacuum in order to minimize air damping of the resonant ring and provide a large quality factor. Researchers at the University of Michigan demonstrated a polysilicon version of the sensor with improved overall performance. The demonstrated specifications of the Delphi Delco sensor over the temperature range of 40 degrees to +125 degrees C include a resolution of 0.5 deg/s over a bandwidth of 25Hz, limited by noise in the electronic circuitry. The nonlinearity in a rate range of +/- 100 deg/s is less than 0.2 deg/s. The sensor survives the standard automotive shock test: a drop from a height of one meter. The specifications are adequate for most automotive and consumer applications [14].

2.2.10 Daimler-Benz (http://www.daimler.com)

The sensor from Daimler Benz AG of Stuttgart, Germany, is a strict implementation of a tuning fork using micromachining technology.

The tines of the silicon tuning fork vibrate out of the plane of the die, driven by a thin-film piezoelectric aluminum nitride actuator on top of one of the tines. The Coriolis forces on the tines produce a torquing moment around the stem of the tuning fork, giving rise to shear stresses that can be sensed with diffused piezoresistive elements. The shear stress is maximal on the center line of the stem and corresponds with the optimal location for the piezoresistive sense elements. The high precision of micromachining is not sufficient to ensure the balancing of the two tines and the tuning of the two resonant frequencies. The vibration modes of a tuning fork are not degenerate. An imbalance in the tines produces undesirable coupling between the excitation and sense resonant modes, which degrades the resolution of the device. A laser ablation step precisely removes tine material and provides calibration of the tuning fork. For this particular design, all resonant modes of the fork are at frequencies above 10 kHz. To minimize coupling to higher orders, the primary and secondary modes are separated by at least 10 kHz from all other remaining modes. The choice of crystalline silicon for tine material allows achieving a high quality factor (approx. 7,000) at pressures below 0.01 mbar. The fabrication process is distinct from that of other yaw-rate sensors in its usage of SOI substrates.

The crystalline silicon over the silicon dioxide layer defines the tines. The thickness control of the tines is accomplished at the beginning of the process by the precise epitaxial growth of silicon over the SOI substrate. The thickness of the silicon layer, and consequently of the tine, varies between 20 and 200 μm, depending on the desired performance of the sensor. Lithography followed by a shallow silicon etch in tetramethyl ammonium hydroxide (TMAH) defines 2 μm deep cavities in two mirror image SOI substrates. Silicon fusion bonding brings these substrates together such that the cavities are facing each other. The cavity depth determines the separation between the two tines. An etch step in TMAH removes the silicon on the front side and stops on the buried silicon dioxide layer which is subsequently removed in hydrofluoric acid. The following steps define the piezoelectric and piezoresistive elements on the silicon surface. Diffused piezoresistors are formed using ion implantation and diffusion. Piezoelectric aluminum nitride is then deposited by sputtering aluminum in a controlled nitrogen and argon atmosphere. This layer is lithographically patterned and etched in the shape of the excitation plate over the tine. Aluminum is then sputtered and patterned to form electrical interconnects and bond pads. Finally, a TMAH etch step from the back side removes the silicon from underneath the tines. The buried silicon dioxide layer acts as an etch stop. An anisotropic plasma etch from the front side releases the tines. The measured frequency of the primary, flexural mode (excitation mode) was 32.2 kHz, whereas the torsional secondary mode (sense mode) was 245 Hz lower. Typical of tuning forks, the frequencies exhibited a temperature dependence. For this particular technology, the temperature coefficient of frequency is 0.85 Hz/degrees C [14].

2.2.11 Northrop Grumman (http://www.northropgrumman.com/)

Northrop Grumman is another U.S. based commercial manufacturer of MEMS gyroscopes. Their MAG-16 is a single axis MEMS gyro designed for applications such as platform stabilization and inertial navigation.

This MEMS gyro has an angular rate measurement range of 150 deg/sec and a bandwidth of 350 Hz (min). It has a specified angle random walk of 1.8 deg/root(Hr). This MEMS gyro is designed and/or packaged to operate in environments possessing unfriendly acceleration, mechanical shock and vibration conditions [24].

2.2.12 NEC-Tokin (http://www.nec-tokin.com/)

NEC-Tokin is a Japanese company that produces a MEMS gyro consisting of a miniature ceramic rod that is piezoelectrically vibrated to induce sinusoidal motion along one axis. Application of an angular rate about an orthogonal axis results in sinusoidal motion along a third orthogonal axis. Electrical circuitry, printed onto the column's surface, detects the sinusoidal motion along the sense axis due to the Coriolis effect [25].

2.2.13 GyroOptics (http://www.gyro.ru/)

Gyrooptics LTD is a Russian company that produces a MEMS electrostatic rotary gyro [15]. In a MEMS rotary gyro, the actuator assembly vibrates the proof mass about a torsional suspension system so that it experiences a rotary sinusoidal motion instead of a translational sinusoidal motion. Otherwise, it operates in a similar fashion to other MEMS vibratory gyros [26].

2.3 Survey of New Developments in MEMS Gyros

It is believed that in future years, major innovations will involve multiaxis sensors, both for linear and angular motion. Three-axis accelerometers using a single proof mass have been presented already as prototypes, but a commercial version has not yet been implemented. As an ultimate goal, a single sensor capable of measuring linear and angular motion for six degrees of freedom is envisioned. Such a sensor can be fully integrated with the control and interface electronics on the same chip. There are reports of a five-axis capacitive motion sensor [13]. Linear acceleration is sensed in this way: out-of-plane acceleration causes the proof mass to move along the z-axis, and in-plane acceleration along either the x- or y-axes makes the proof mass tilt. Additionally, the proof mass is vibrated along the z-axis with electrostatic forces. Angular motion about the x- or y-axes induces a Coriolis-based tilting oscillation of the proof mass. The oscillatory signals are of much higher frequency (about 2 kHz) as the signals caused by linear acceleration, and hence, they can be separated easily in the frequency domain using electronic filters. In this way, linear acceleration and angular rate signals can be measured concurrently. Another very promising approach towards such a sensor is to use a micromachined disk that is levitated by electrostatic or magnetic forces and spun about its main axes. This is similar to macroscopic flywheel type gyroscopes; however, the lack of a good bearing in the microworld has excluded this approach so far for micromachined gyroscopes. Using a levitated object alleviates this problem. Any angular motion perpendicular to the spin axis of the disk will cause it to recess, and this can be detected by a capacitive position measurement to provide a measure of the angular velocity. Force feedback is used with this type of gyro to keep the flywheel in the same position relative to the surrounding frame. The angular rate measurement is embedded in the control signal(s). Using a levitated object for inertial sensing has several advantages. First, since there is no mechanical connection from the substrate to the disk, the effective spring constant is solely dependent on the electrostatic forces set up by voltages or currents applied to surrounding electrodes or coils; hence, the characteristics of the sensor, such as bandwidth and sensitivity, can be adjusted in the control electronics, according to the application requirements. Second, when used as a gyroscope, quadrature error is inherently eliminated in this sensor architecture. The comparable effect, due to the imbalance of the mass, will manifest itself at the rotation frequency, whereas the Coriolis force will cause the disk to recess at the rotational speed of the body of interest. These two frequencies are several orders of magnitude apart and are therefore easy to separate. Furthermore, there is no need to tune the drive and sense resonant frequencies since the scale factor does not depend on the matching of different modal frequencies. Linear acceleration along the three axes can be measured simultaneously by measuring the displacement of the disk [13]. Levitation of gyros using magnetic forces has been investigated and successfully demonstrated. The electromagnetic forces are produced by currents up to 1A, which precludes the use of standard integrated electronics, which is a severe disadvantage of this approach. A more promising approach is to use electrostatic forces to levitate and spin a disk [13]. A prototype of such a device has demonstrated the feasibility of using it for simultaneously detecting linear and angular motion [13]. There is also a design and simulation of a similar device for three-axis acceleration measurement, which is also suitable to detect angular motion about two axes if rotated. Here, the micromachined disk is incorporated in a multipath sigma-delta modulator control system [13].

A number of researchers at U.S. universities are conducting research to improve MEMS gyros. Charles Ellis at Auburn University is developing a MEMS gyro that consists of an electrostatically levitated and rotating micromachined proof mass structure, similar in operation to a traditional rotating proof mass gyroscope. As previously discussed, a levitated and rotating proof mass gyro could possibly result in a better performing MEMS gyro than is currently available in vibratory MEMS gyro technology [27].

The University of California at Berkley has been involved in was the development of a low-noise vibratory MEMS gyro with integrated electronics to yield a digital output. This gyro had a measured noise floor of 3 deg/s/root(Hz) [27].

The University of California at Irvine also has a successful MEMS gyro research program. Dr. Shkel has been investigating the possibility of realizing extremely robust vibratory MEMS gyros with significantly improved performance achieved by utilizing an improved mechanical architecture instead of trying to correct for mechanical imperfections with feedback controllers. In this particular design, multiple drive-mode and sense-mode oscillators were utilized to realize a highly complex and robust mechanical system [27].

Dr Garry Fedder, a professor at Carnegie Mellon University, has developed a MEMS gyro with a microfabrication process that realized the structural components of the MEMS gyro as post processing to a fabricated CMOS ASIC. This technique allows the support electronics to reside on the same chip as the mechanical elements of the gyro, thus minimizing the size of the sensor [27].

Dr. Rajesh Rajamani, a professor at the University of Minnesota, has been researching the development of a MEMS vibratory gyro that can not only measure angular rate, but also absolute angular position. The operating principle is based on measuring the angle of free vibration of the suspended proof mass with respect to the surrounding casing of the gyro structure. This is very difficult to accomplish due to the limitations and tolerances in microfabrication technology, as well as the underlying physics of the problem. Dr. Rajamani proposed an innovative nonlinear control system to compensate for these limitations [27].

Dr. Farrokh Ayazi is a professor at the Georgia Institute of Technology. He has conducted a lot of research in the development MEMS gyros, both in regard to mechanical device design and fabrication, and in regard to support electronics development. A tuning fork style MEMS gyro was fabricated in an SOI process. The gyro was designed to use quadrature error to achieve and maintain perfect mode matching. This was accomplished through both the mechanical design of the gyro element and the use of a control loop implemented in a CMOS ASIC. This exceptional gyro achieved an unprecedented 0.003 deg/root(hr) angle random walk (ARW) [27].

Dr. Tayfun Akin is a professor at Middle East Technical University in Turkey. His goal is to improve the quality of MEMS gyros, and especially those MEMS gyros packaged at atmospheric pressure. This research has resulted in a MEMS gyro architecture that utilizes a symmetric design which is intended to minimize resonant frequency mismatch of the structure between the drive and sense axes. Otherwise, frequency mismatch between the drive and sense modes will cause mechanical coupling which leads to unstable operation and increased zero-rate output drift. This technique was utilized to realize a symmetric and decoupled silicon microgyroscope structure that has varying-gap type sense electrodes for improved rate sensitivity, post-processing electrostatic frequency tuning capability, symmetric and folded suspensions for mechanical decoupling and a large drive-mode amplitude [27].

Dr. Minhang Bao is a professor at Fudan University in China. He has developed several MEMS gyros based on variants of a two-beam vibratory MEMS gyroscopic sensor architecture that used piezoresistive off-axis motion sensing instead of the more widely used capacitive off-axis sensing. These gyros were designed to operate at atmospheric pressure instead of in hermetically sealed packages at low or high vacuum.. The two large proof mass structures were electrostatically vibrated out of plane with the substrate using an electrode beneath each proof mass, where each proof mass is connected to the substrate using a single cantilevered beam. Application of an angular rate resulted in sinusoidal in plane motion, which was detected by piezoresistors embedded in the neck of the cantilevered beam for each proof mass. By using two proof mass structures in one gyro, common mode effects, such as a translational acceleration, could be cancelled out. Additionally, Dr. Bao has been developing novel sensing techniques for MEMS gyros, such as an architecture that used phase detection instead of the more popular amplitude detection to measure off-axis motion. This technique could potentially improve performance over amplitude detection techniques, as well as improve immunity to interference and temperature sensitivity [27].

Dr. Alfredo Cigada, professor at Politecnico di Milano in Italy, has yielded a fast, efficient, and reliable measurement method that allows the identification of the modal parameters of a MEMS tuning fork gyroscope both in the design phase (for statistical analysis), and in the verification phase, when MEMS gyros have already been installed in their final package. Additionally, the developed technique could be applied to any resonating MEMS device. The electrical measurement technique was based on the measurement of the ground currents flowing in different parts of the device when it was excited through a step excitation. This technique was used to identify the primary mechanical parameters (resonant frequency and quality factor) of the gyroscope and its quadrature error. There are many uses for a technique like this, including initial performance verification, performance optimization through autocalibration, and in-field built-in self test (BIST) [27].

Honglong Chang is a researcher at Northwestern Polytechnical University in China. He has investigated the optimization of MEMS based systems by considering the coupling effects in the fabrication process, the parameters of the physical structure of the device, the packaging/operating environment and the interface electronics. This technique is called "Multidisciplinary Design Optimization (MDO)" and uses a genetic algorithm. A MEMS gyro was used as the demonstration vehicle for this approach. Chang has also been involved in the development of a z-axis MEMS gyroscope that had a novel architecture (proof mass suspension system) utilized to decouple the drive mode from the sense mode. Additionally, the sensor was realized as a bulk micromachined gyroscope (a DRIE etched Si wafer anodically bonded to glass) instead of a surface micromachined gyroscope, in order to achieve greater sensitivity. Dr. Chang has also developed a bulk micromachined single chip IMU containing three orthogonally arranged accelerometers and three orthogonally arranged gyroscopes. However, the sensor interface electronics did not reside on the same chip as the micromachined sensor elements. The unpackaged micromachined chip was approximately 9mm by 9mm [27].

Dr. Dong-il Cho is a professor at Seoul National University in South Korea. Dr. Cho has developed several MEMS gyros using various modifications to a MEMS fabrication process called SBM (Surface/bulk micromachining). With this process, a solid (111) Si wafer or an SOI wafer with a (111) Si device layer is used. The wafer is patterned and DRIE etched down to some desired depth. Then the wafer is conformally coated with silicon dioxide or silicon nitride. Next the wafer is further DRIE etched to define a “release gap.” The sidewalls in the etched trenches where the release gap will be formed are now coated with the silicon dioxide or silicon nitride coating. The wafer is then placed in an orientation dependent etchant, such as TMAH, which etches along the (111) crystal plane (but only very slowly in the (111) direction), which is in the horizontal direction and below the protective coating. This undercuts the protected features. The time dependent etch runs horizontally and is allowed to etch until the desired features are released, but is stopped before the desired anchor points are fully released. Several advantages are claimed for this process, such as avoidance of the undercutting or footing problems possible in SOI processes, a smooth bottom surface on the defined features, being able to set an arbitrary depth for the release gap and the avoidance of stresses inherent in SOI wafers. Dr. Cho’s researchers made various modifications to the SBM process and fabricated MEMS vibratory gyroscopes. The most notable gyroscope developed was one where the SBM process was used with multiple passivation and DRIE etch steps in order to realize Si teeth that were vertically offset, which realized a vertical comb-drive actuator that was demonstrated in the fabrication of an x-axis gyroscope. By using this technique, however, three orthogonal gyroscopes could be realized on the same substrate, resulting in 3-axis angular rate measurement. The fabricated gyro was tested in a 60 mTorr vacuum chamber by applying a 20 deg/s 30Hz angular rate. A measured bandwidth of over 100Hz was achieved, and an equivalent angle random walk of 0.01 deg/s/root(Hz) was achieved [27].

Dr. Dzung Viet Dao is a post doctoral fellow at the Micro Nano Integrated Devices Laboratory at Ritsumeikan University in Japan. Dr. Dao has developed a miniature two axis gyroscope that used a forced gas flow to detect rotation, by using the resulting Coriolis force to deflect the gas flow with regard to two micromachined Si thermistor half Wheatstone bridges, which detected the change in flow direction by a temperature change in the thermistors. Neon gas was used as the fluid in the sensor. A gyroscope sensitivity of 0.15 mV/deg/s was achieved in a prototype unit, over an evaluation range of nearly +/- 400 deg/s. The thermistors were fabricated by micromachining them in Si. The completed sensor used MEMS components (the thermistors) but was not implemented as a completely micromachined gyroscopic sensor. The stated intended use of this two axis gyroscopic sensor was for ship anti-rolling and stabilization systems [27].

Tohoku University in Japan has had some role in the development of electrostatically levitated and rotated ring and sphere inertial sensors. A Si to glass anodic bonding procedure is utilized. Electrical feedthroughs were realized in the glass substrate by RIE etching through the glass and then plating Ni up though the vias. In this particular gyro, the 1.5 mm diameter micromachined ring that served as the rotor was levitated and rotated at 74,000 RPM. The sensor was capable of two axis angular rate measurement (150 deg/s) and three axis acceleration measurement (5 g) [27].

Dr. Weileun Fang is currently a professor at National Tsing Hua University in Taiwan. Dr. Fang has designed a dual-axis sensing decoupled vibratory wheel gyroscope. The basic architecture is that of an electrostatically driven rotary MEMS gyro. This design, however, realizes a decoupled gyroscope that can sense angular rotation about two axes instead of one. Since the design is decoupled, there will be no sensing interference and this eliminates the need for feedback detection and compensation. A triple-beam-shaped torsional spring is used to suppress the undesired in-plane linear motion of the outer ring. The natural frequency of the device is approximately 4600 Hz. Also, the device has a quality factor of 2000 and a sensitivity of 7.4 fF/deg/s. In the range of +/- 150 deg/s the dual-axis sensing mode has a nonlinearity of 0.04 percent [27].

Dr. Barry J. Gallacher and Dr. James Burdess are professors at the University of Newcastle Upon Tyne in the UK. They have worked together for a number of years to develop on a 3-axis vibrating microring gyroscope. The basic structure consisted of a tethered micromachined ring that was designed to possess degenerate modes. Two of these modes would possess the same natural frequency, but would have minimas and maximas around the ring that were spatially offset by 30 degrees along the ring. Plate electrodes below the ring would be used to detect out of plane vibration while in-plane electrodes would be used to excite the ring into vibratory motion. A key to achieving the desired goals was the use of (111) orientation Si wafers to approximate isotropic material properties in the ring structure, which was necessary for the sensor to function well. The functionality of this MEMS gyro architecture requires extremely tight and usually unachievable manufacturing and material property tolerances. Therefore active tuning algorithms were developed to compensate for this issue. One example was the use of active control of the damping to increase the quality factor of the gyro. Another example was the implementation of a method of correcting for mass and stiffness "imperfections" in the micromachined microring gyroscope by tuning the device with electrostatic forces generated by adding additional electrodes at specific locations relative to the ring structure. This active tuning method could be used in conjunction with or in place of “hardware tuning” during fabrication with methods such as laser ablation or focused ion beam (FIB) trimming. Another example was the use of an excitation and control scheme (combined parametric excitation and harmonic forcing) to significantly reduce signal feedthrough from the primary or driven motion to the secondary or detection motion of the vibrating structure. The researchers claimed that this improvement would be a factor leading to a true low-cost inertial grade micro gyro [27].

Dr. Mohamed Toriq Kahn is a professor at Cape Peninsula University of Technology in South Africa. Dr. Kahn has been investigating the realization of a FOG (fiber optic gyroscope) in MEMS technology. Dr. Kahn theorized the realization of a MEMS FOG system based on using ultra fine fiber optic cable. This type of fiber optic cable could be as small as 2nm across and is based on a technique developed at the University of California where very fine spider silk was utilized as a mold or template for creating extremely small diameter optical fibers. By utilizing optical fiber of this size with optical MEMS and micro-optical components, he theorized that a single chip FOG sensor could be realized where the tiny optical fiber would be wound around a micromachined structure on a MEMS chip. Many issues remain to be solved before such a MEMS gyro could be realized, such as optical signal injection into the tiny fiber and propagation losses of the optical signal in the fiber [27].

Dr. Michael Kraft is a professor at Southampton University in the U.K. His primary research interest is the development of closed-loop MEMS sensors that employ sigma-delta modulation (SDM) based force feedback, where the proof mass is held in a nearly constant position by an SDM controller utilizing electrostatic forces. The SDM control signal, a digital pulse density modulated bitstream, then contains the measurement of interest (applied acceleration(s) and/or angular rate(s)). In particular, Dr. Kraft has sought to apply this technology to MEMS gyros. For example, he was involved in the development of a DARPA funded project to design and build a 5V, CMOS z-axis gyroscope chip. The MEMS gyro used an SDM controller, which is a common theme to much of Kraft's research. For several years, Kraft has also been involved in an on-going project to develop a multi-axis inertial sensor consisting of a micromachined levitated and rotating disk proof mass that utilizes an SDM controller in a force feedback configuration with electrostatic forces to keep the levitated proof mass in approximately the same location. The potential advantages of this approach, if successful, would probably be an inertial sensor at least as good as the best MEMS gyros today and probably a gyroscope far superior to current state-of-the-art MEMS vibratory gyros. This approach avoids many of the limitations of commercially available vibratory MEMS gyros, such as fabrication tolerances in the mechanical springs (Dr. Kraft's gyro architecture uses a fully controllable electrostatic spring), quadrature errors in vibratory gyros (this design uses a levitated rotating proof mass) and large motion induced nonlinearities (this design uses SDM force feedback to limit the proof mass motion to small displacements) [27].

Dr. Jang Gyu Lee is a professor at Seoul National University in South Korea and has been developing advanced control loops for MEMS gyros, such as a digital rebalance loop for a dynamically tuned gyroscope using a Linear Quadratic Gaussian / Loop Transfer Recovery method; an H2-based controller for a digital rebalance loop [40]; an H2 control scheme to fabricate an analog closed-loop condition to enlarge the bandwidth, enhance linearity and provide robustness over unmodeled dynamics; and a Kalman filter to reduce the deterministic and random errors of a vibrating gyroscope used in GPS navigation systems and autonomous mobile robots. Dr. Lee has also developed an electrostatically-driven and electromagnetically-sensed vibratory MEMS gyro. The fabrication process is based on a surface-bulk micromachining process. This MEMS gyro can be operated at atmospheric pressure with good output characteristics as opposed to typical hermetically sealed low pressure packaging [27].

Dr. Sheng Liu is the Director of the Institute of Microsystems and Director of MOEMS Division at Wuhan National Laboratory of Optoelectronics which is maintained by Huazhong University of Science and Technology in China. Dr. Liu has been developing a micro thermo-fluidic gyroscope utilizing bidirectional liquids. The proposed gyroscope consisted of two main flow channels that each split into two symmetrical outlet ports. Each outlet port had a thermistor for measuring the temperature of the fluid as it flowed through that outlet port. When the device experienced an angular rate, the mass flow rate of the symmetric microchannels became unequal, resulting in a temperature difference between the two ports. By measuring the temperature difference between the symmetric thermistors, the angular rate was obtained [27].

Dr. Helmut Seidel is a professor at Saarland University in Germany. He conducts research in MEMS tuning fork style gyros and in particular for automotive safety applications. His research team has developed a silicon micromachined tuning fork gyroscope that is driven by two piezoelectric thin film actuators. The applied external angular rate was determined by sensing the resulting torsional motion around the structure's sensitive axis that resulted from the Coriolis effect. The shear strain was proportional to the angular rate and was detected by piezoresistive read-out sensing. The sensor output voltage was adversely affected by certain parasitic effects such as mechanical imbalance, actuation imbalance and drive motion parasitics. To combat these factors, the researchers suggested several methods of minimizing these parasitic effects, such as phase-locked loop (PLL) electronic circuitry, tight production tolerances, post-process trimming of the sensor mass at specific locations, stem design optimization, electrical actuator compensation and read-out element beam positioning. The testing results showed that this tuning fork gyroscope had outstanding behavior under external shock. It also had a CMOS-compatible fabrication process and a relatively small chip-size of less than 15 mm x 15 mm [27].

Dr. Yung Ting is an associate professor at Chung Yuan Christian University in Taiwan. Dr. Ting has been investigating the effects of a polarized electric field on the sensitivity, mechanical quality factor, and resonant frequency of a piezoelectric solid-beam cylinder-type vibratory gyro. The gyro utilized for this investigation was ceramic and had the advantage of material uniformity. His simulation analysis and experimental results of the ceramic cylinder gyro revealed that the resonant frequency of the primary and secondary modes of the cylinder gyroscope were nearly equal. This indicated that the axis-symmetry of the cylinder gave it the advantage of having increased sensitivity. Besides the effect on resonant frequency, it was also determined that the polarized electric field was proportional to the sensing voltage, thus it was proportional to the sensitivity. From the ANSYS simulation, it was concluded that a cylinder with a small diameter would easily achieve a high polarized electric field, and a large diameter cylinder would need a higher applied polarized voltage to preserve complete polarization. Furthermore, equal width of the electrodes and the clearance between the adjacent electrodes would yield a better polarized electric field. Since it was determined that a linear relationship between the sensing voltage and the rotation speed existed, the ceramic cylinder gyro would be suitable for measurement of rotation speed in low and medium speed applications [27].

Dr. Xue Zhong Wu is with the Laboratory of Precision Engineering and MEMS at the National University of Defense and Technology in China. Dr. Wu has been developing a MEMS interdigitated transducer (IDT) surface acoustic wave (SAW) two axis gyroscope. The sensor consisted of two orthogonally mounted SAW resonators that can each act as a SAW resonator and as a SAW sensor. When a standing wave is generated in a SAW device, particles on the substrate in the standing wave experience oscillatory motion and respond to the Coriolis force when the substrate experiences an angular rotation. This effect can be detected using an orthogonally located SAW sensor. However, if the orthogonally mounted SAW resonators are used as both SAW generators and as sensors, then two-axis angular rate detection is possible. Dr. Wu used this architecture in developing his MEMS gyro and speculated that this architecture would be resistant to mechanical shock and vibration, at least compared to traditional MEMS vibratory gyros.

Dr. Bin Xiong is a professor at the Shanghai Institute of Microsystem and Information Technology (SIMIT) in China. Dr. Xiong has developed a vibratory MEMS gyro designed to operate at ambient pressure. The sensor consisted of an anchored Si proof mass that was forced to oscillate along the in-plane x-axis by the tangential force produced by applying a voltage waveform between the proof mass structure and offset electrodes located beneath it. When the device was subjected to an angular rotation about the z axis (normal to the device surface), the proof mass would experience motion along the in-plane y-axis due to the Coriolis force, which was detected by a change in capacitance between the proof mass and other electrodes located beneath it. A motivating factor for the development of this gyro architecture was a desire to avoid vacuum packaging [27].

Dr. Yishen Xu is a researcher at Southeast University in China. He developed a monolithic triaxial micromachined capacitive gyro that consisted of two uniaxial in-plane (x and y axis) gyros and one uniaxial out-of-plane (z axis) gyro. All three gyros utilized electrostatic force actuators and capacitive detection methods. A 300 deg/sec prototype was fabricated using bulk micromachining technology and evaluated. Testing indicated only a 5 percent error between the estimated resonant frequency and the realized resonant frequency. Dr. Xu has also been developing signal processing techniques for improving the performance of MEMS gyros. For example, he used an adaptive Kalman filter to actively compensate for any drift signal in a particular MEMS gyro. He has also investigated the use of a folded-flexure spring design based suspension system to minimize quadrature error in MEMS gyros [27].

Dr. Sang Sik Yang is a professor at Ajou University in South Korea. Dr. Yang has developed a micro rate gyroscope (MRG) based on the surface acoustic wave (SAW) gyroscopic effect, for use in extremely high-shock military applications. The gyro (called the SAWMRG) consisted of two SAW delay-line oscillators. The two surface acoustic waves were generated by separate SAW oscillators and propagated in opposite directions on the substrate. When the substrate experienced an angular rate about the out-of-plane z axis, the resulting Coriolis force would cause an opposite frequency shift in the frequencies of the two oscillators. Demodulation was used to recover an output signal whose frequency was proportional to the applied angular rate. The 9 x 9 mm^2 SAWMRG was fabricated on a ST-cut quartz substrate and loaded into a specially designed low temperature co-fired ceramic (LTCC) package to ensure good RF characteristics. The center frequency and the insertion loss of the delay line were measured at 98.6 MHz and 15.2 dB, respectively. Using a rate table and stochastic noise analysis, a sensitivity of 0.431 Hz/deg/s was measured in angular rates up to 2000 deg/s and a white noise of 0.55/deg/s/root(Hz), respectively. A SAW-based gyroscope has an inherent shock robustness due to having no moving mechanical parts. Also, the fabrication process uses only lithography and a metallization processes like that of a conventional SAW filter [27].

Dr. Weiping Zhang is a professor at the Institute of Micro and Nano Science and Technology at Shanghai Jiao Tong University in China. Dr. Zhang has developed an electromagnetic micromotor with an alumina rotor. It was levitated, rotated, sensed, and controlled by independent coils and a capacitance structure. Levitated force with lateral stability was produced by the electromagnetic interaction between the rotor and four groups of levitation planar coils with inner and outer conductors carrying opposite phase high frequency AC current. The rotation was realized by a four-phase induction micromotor composed of the rotor and eight rotation planar coils carrying AC current. Eight sense electrodes and the rotor created a non-contact capacitive displacement sensing system. The torque returning the rotor to its equilibrium position was produced by four groups of planar coils. A prototype device with a rotational speed of 3035 RPM, a levitation height of 200 μm, and a scale factor of 0.212 V/deg, has been designed, fabricated and successfully tested. This project illustrated that the micromotor could be used to construct a MEMS levitated and rotating proof mass gyro [27].

Dr. Rong Zhu is a professor at Tsinghua University in China. Dr. Zhu has developed a micromachined gas inertial sensor based on the principle of convective heat transfer that was capable of sensing acceleration in two axes and angular rate about one axis. The sensor consisted of a small silicon etched cavity, a suspended central heater and four suspended thermistor wires, all of which were assembled and packaged in a hermetically sealed chamber. The sensor measured temperature gradients induced by inertial forces acting on the gas flowing in the sealed chamber. The temperature gradients were detected using the four thermistors, and the applied two axis acceleration and one axis rotational rate were then determined from the output signals from the thermistors [27].

2.4 The Analog Devices ADXRS300 Angular Rate Sensor

Analog Devices (ADI) is home to the ADXRS family of integrated angular rate-sensing gyroscopes, which contains the ADXRS300 (with dynamic range of +/- 300 deg/sec) and the ADXRS150 (with dynamic range of +/- 150 deg/sec). It is the first fully integrated commercial gyroscope. A picture of the chip is shown in Figure 2.10.

It operates from a 5V supply over the industrial temperature range of 40 degrees C to +85 degrees C and is available in a space-saving 32-pin Ball Grid Array surface-mount package measuring 7 x 7 x 3 mm. Both are priced at approximately 30 dollars per unit in thousand-piece quantities. Because the internal resonators require 14V to 16V for proper operation, ADI includes on-chip charge pumps to boost an applied TTL-level voltage. Both

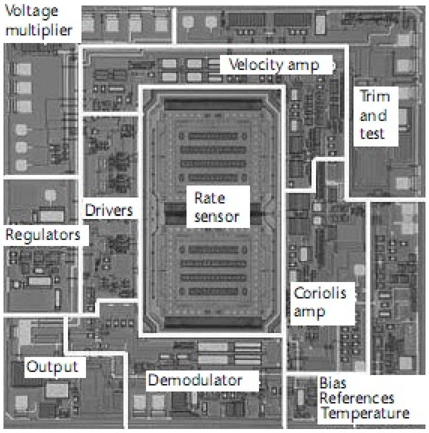

Figure 2.10: Die photo of the Analog Devices ADXRS300 [28]

the ADXRS150 and ADXRS300 are essentially z-axis devices based on the principle of resonant-tuning-fork gyroscopes. In these systems, two polysilicon sensing structures each contain a so-called dither frame that is driven electrostatically to resonance. Interestingly, the gyroscope includes two identical structures to enable differential sensing in order to reject environmental shock, vibration, and effects from translational motion. Figure 2.11 shows one structure schematically.

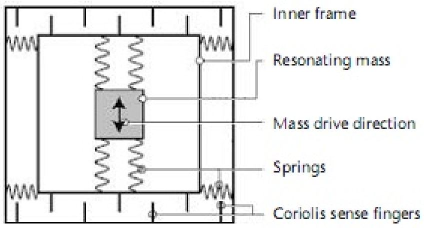

Figure 2.11: Schematic of the gyroscope elements

A rotation about the z-axis, normal to the plane of the chip, produces a Coriolis force that displaces the inner frame perpendicular to the vibratory motion. This Coriolis motion is detected by a series of capacitive pick-off structures on the edges of the inner frame. The resulting signal is amplified and demodulated to produce the rate signal output [13].

The ADXRS300 is a complete angular rate sensor (gyroscope) that uses Analog Devices' surface-micromachining process to make a functionally complete and low cost angular rate sensor integrated with all of the required electronics on one chip. The manufacturing technique for this device is the same high volume BiCMOS process used for high reliability automotive airbag accelerometers. The output signal, RATEOUT (pins 1B, 2A), is a voltage proportional to angular rate about the axis normal to the top surface of the package (see Figure 2.12).

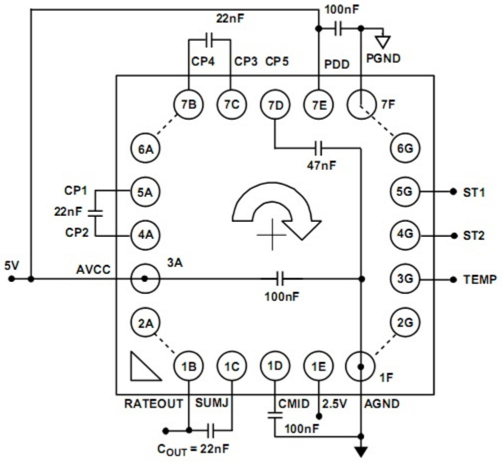

Figure 2.12: ADXRS300 application circuit

A single external resistor can be used to lower the scale factor. An external capacitor is used to set the bandwidth. Other external decoupling and charge pump capacitors are required for operation (see Figure 2.13).

A precision voltage reference for using an external A/D converter and a temperature output are also provided for compensation techniques. Two digital self-test inputs electromechanically excite the sensor to test proper operation of both sensors and the signal conditioning circuits. The ADXRS300 is available in a 7 mm x 7 mm x 3 mm BGA chip-scale package.

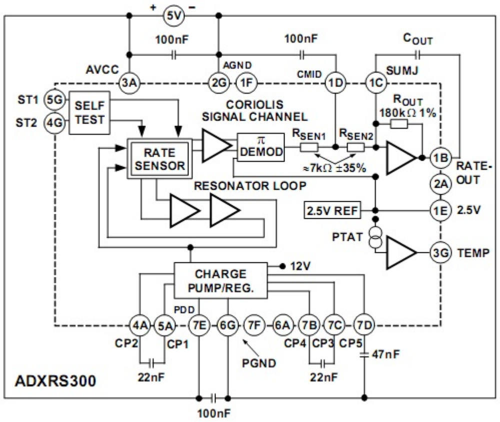

Figure 2.13: Block diagram with external components

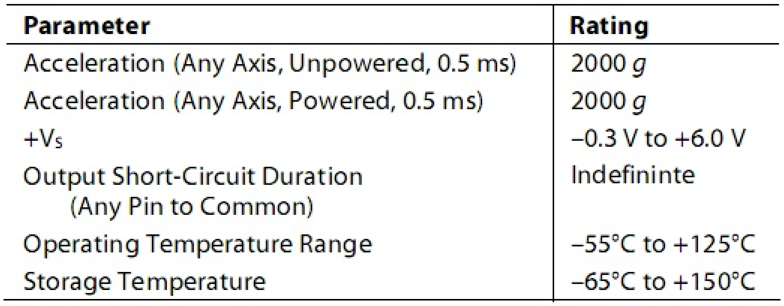

Parameter	Rating
Acceleration (Any Axis, Unpowered, 0.5 ms)	2000 *g*
Acceleration (Any Axis, Powered, 0.5 ms)	2000 *g*
$+V_S$	−0.3 V to +6.0 V
Output Short-Circuit Duration (Any Pin to Common)	Indefininte
Operating Temperature Range	−55°C to +125°C
Storage Temperature	−65°C to +150°C

Figure 2.14: Absolute maximum ratings

Stresses above those listed under the Absolute Maximum Ratings in Figure 2.14 may cause permanent damage to the device. This is a stress rating only; functional operation of the device at these or any other conditions above those indicated in the operational section of this specification is not implied. Exposure to absolute maximum rating conditions for extended periods may affect device reliability. Applications requiring more than 200 cycles to MIL-STD-883 Method 1010 Condition B (55 degree C to +125 degrees C) require underfill or other means to achieve this requirement. Drops onto hard surfaces can cause shocks of greater than 2000 g and exceed the absolute maximum rating of the device.

This is a Z-axis rate-sensing device that is also called a yaw rate sensing device. It produces a positive going output voltage for clockwise rotation about the axis normal to the package top, i.e., clockwise when looking down at the package lid.

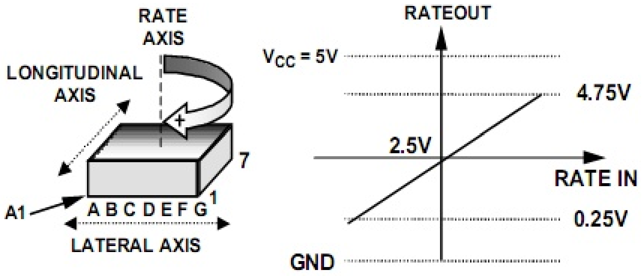

Figure 2.15: RATEOUT signal v. clockwise rotation

The ADXRS300 operates on the principle of a tuning fork resonator gyro. Two polysilicon sensing structures each contain a dither frame, which is electrostatically driven to resonance. This produces the necessary velocity element to produce a Coriolis force when the device experiences angular rate. At two of the outer extremes of each frame, orthogonal to the dither motion, there are movable fingers that are interdigitated with fixed pickoff fingers to form a capacitive pickoff structure that senses Coriolis motion. The resulting signal is fed to a series of gain and demodulation stages that produce the electrical

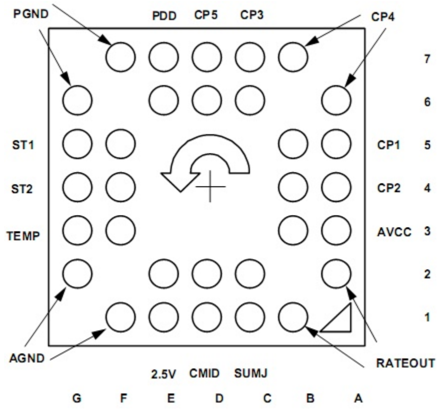

Figure 2.16: BGA pin diagram

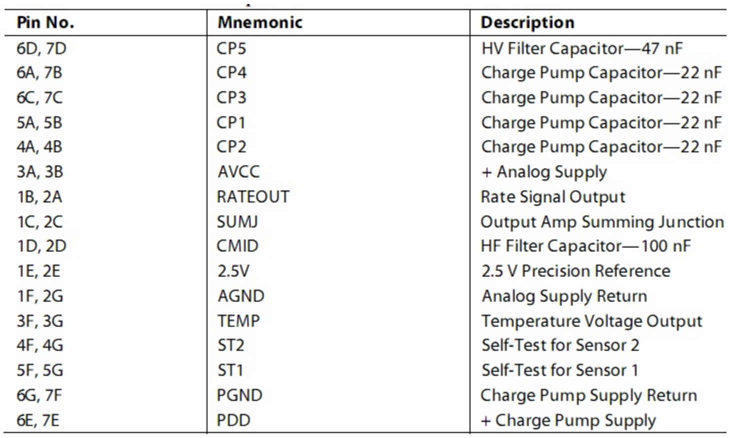

Pin No.	Mnemonic	Description
6D, 7D	CP5	HV Filter Capacitor—47 nF
6A, 7B	CP4	Charge Pump Capacitor—22 nF
6C, 7C	CP3	Charge Pump Capacitor—22 nF
5A, 5B	CP1	Charge Pump Capacitor—22 nF
4A, 4B	CP2	Charge Pump Capacitor—22 nF
3A, 3B	AVCC	+ Analog Supply
1B, 2A	RATEOUT	Rate Signal Output
1C, 2C	SUMJ	Output Amp Summing Junction
1D, 2D	CMID	HF Filter Capacitor—100 nF
1E, 2E	2.5V	2.5 V Precision Reference
1F, 2G	AGND	Analog Supply Return
3F, 3G	TEMP	Temperature Voltage Output
4F, 4G	ST2	Self-Test for Sensor 2
5F, 5G	ST1	Self-Test for Sensor 1
6G, 7F	PGND	Charge Pump Supply Return
6E, 7E	PDD	+ Charge Pump Supply

Figure 2.17: Pin Functions

rate signal output. The dual-sensor design rejects external g-forces and vibration. Fabricating the sensor with the signal conditioning electronics preserves signal integrity in noisy environments. The electrostatic resonator requires 14 V to 16 V for operation. Since only 5 V is typically available in most applications, a charge pump is included on-chip. A charge pump is a simple voltage multiplier. If an external 14 V to 16 V supply is available, the two capacitors on CP1 through CP4 can be omitted and this power supply can be connected to CP5 (Pin 7D) with a 100 nF decoupling capacitor in place of the 47 nF capacitor. After the demodulation stage, there is a single-pole low-pass filter consisting of an internal 7 kΩ resistor (RSEN1) and an external user-supplied capacitor (CMID). A CMID capacitor of 100 nF sets a 400 Hz +/- 3-5 percent low-pass pole and is used to limit high frequency artifacts before final amplification. The bandwidth limit capacitor, COUT, sets the pass bandwidth.

Only power supplies used for supplying analog circuits are recommended for powering the ADXRS300. High frequency noise and transients associated with digital circuit supplies may have adverse effects on device operation. Fig. 2.12 shows the recommended connections for the ADXRS300 where both AVCC (+ analog supply) and PDD (charge pump supply) have a separate decoupling capacitor. These should be placed as close to the their respective pins as possible before routing to the system analog supply. This minimizes the noise injected by the charge pump that uses the PDD supply. It is also recommended to place the charge pump capacitors connected to the CP1 through CP4 pins as close to the part as possible. These capacitors are used to produce the on-chip high voltage supply switched at the dither frequency at approximately 14 kHz. Surface-mount chip capacitors are suitable as long as they are rated for over 15 V.

External capacitors CMID and COUT are used in combination with on-chip resistors to create two low-pass filters to limit the bandwidth of the ADXRS300's rate response. The 3 dB frequency set by ROUT and COUT is shown in Equation 2.5.

$$f_{OUT} = 1/(2 * \pi * R_{OUT} * C_{OUT}) \tag{2.5}$$

The bandwidth can be well controlled since ROUT has been trimmed during manufacturing to be 180 kΩ +/- 1 percent. Any external resistor applied between the RATEOUT (1B, 2A) and the output amplifier summing junction, SUMJ (1C, 2C) pins, results in Equation 2.6.

$$R_{OUT} = (180,000 * R_{EXT})/(180,000 * R_{EXT}) \tag{2.6}$$

The 3 dB frequency is set by RSEN (the parallel combination of RSEN1 and RSEN2) at about 3.5 kΩ nominal; CMID is less well controlled since RSEN1 and RSEN2 have been used to trim the rate sensitivity during manufacturing and have a +/- 35 percent tolerance. Its primary purpose is to limit the high frequency demodulation artifacts from saturating the final amplifier stage. Thus, this pole of nominally 400 Hz @ 0.1 μF need not be precise. Lower frequency is preferable, but its variability usually requires it to be about 10 times greater (in order to preserve phase integrity) than the well-controlled output pole. In general, both 3 dB filter frequencies should be set as low as possible to reduce the amplitude of these high frequency artifacts and to reduce the overall system noise.

The full-scale measurement range of the ADXRS300 can be increased by placing an external resistor between the RATEOUT (1B, 2A) and SUMJ (1C, 2C) pins, which would parallel the internal ROUT resistor that is factory-trimmed to 180 kΩ. For example, a 330 kΩ external resistor will give approximately a 50 percent increase in the full-scale range. This is effective for up to a 4X increase in the full-scale range (minimum value of the parallel resistor allowed is 45 kΩ). Beyond this amount of external sensitivity reduction, the internal circuitry headroom requirements prevent further increase in the linear full-scale output range. The drawbacks of modifying the full-scale range are the additional output null drift (as much as 2 deg/sec over temperature) and the readjustment of the initial null bias.

The ADXRS300's RATEOUT signal is nonratiometric, i.e., neither the null voltage nor the rate sensitivity is proportional to the power supply voltage. Rather, they are nominally constant for dc supply changes within the 4.75 V to 5.25 V operating range. If the ADXRS300 is used with a supply-ratiometric ADC, the ADXRS300's 2.5 V output can be used to make corrections in software for the supply variations.

Null adjustment is possible by injecting a suitable current to SUMJ (1C, 2C). Adding a suitable resistor to either ground or to the positive supply is a simple way of achieving this. The nominal 2.5 V null is for a symmetrical swing range at RATEOUT (1B, 2A). However, a nonsymmetric output swing may be suitable in some applications. Note that if a resistor is connected to the positive supply, then supply disturbances may reflect some null instabilities. Digital supply noise should be avoided, particularly in this case. The resistor value to use is approximately shown in Equation 2.7.

$$R_{NULL} = (2.5 * 180,000)/(V_{NULL0} - V_{NULL1}) \tag{2.7}$$

VNULL0 is the unadjusted zero rate output, and VNULL1 is the target null value. If the initial value is below the desired value, the resistor should terminate on common or ground. If it is above the desired value, the resistor should terminate on the 5 V supply. Values are typically in the 1 MΩ to 5 MΩ range. If an external resistor is used across RATEOUT and SUMJ, then the parallel equivalent value is substituted into Equation 2.7. The resistor value is an estimate since it assumes VCC = 5.0 V and VSUMJ = 2.5 V.

The ADXRS300 includes a self-test feature that actuates each of the sensing structures and associated electronics in the same manner as if subjected to angular rate. It is activated by standard logic high levels applied to inputs ST1 (5F, 5G), ST2 (4F, 4G), or both. ST1 causes a voltage at RATEOUT equivalent to typically 270 mV (-60 deg/s), and ST2 causes an opposite +270 mV (+60 deg/s) change. The self-test response follows the viscosity temperature dependence of the package atmosphere, approximately 0.25 percent/degrees C. Activating both ST1 and ST2 simultaneously is not damaging. Since ST1 and ST2 are not necessarily closely matched, actuating both simultaneously may result in an apparent null bias shift [28].

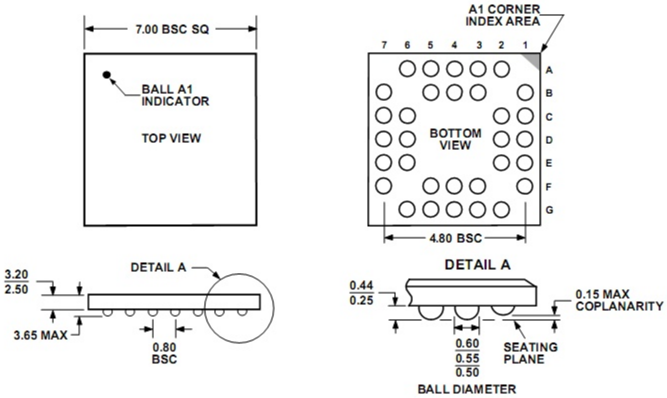

Figure 2.18: ADXRS300 dimensions

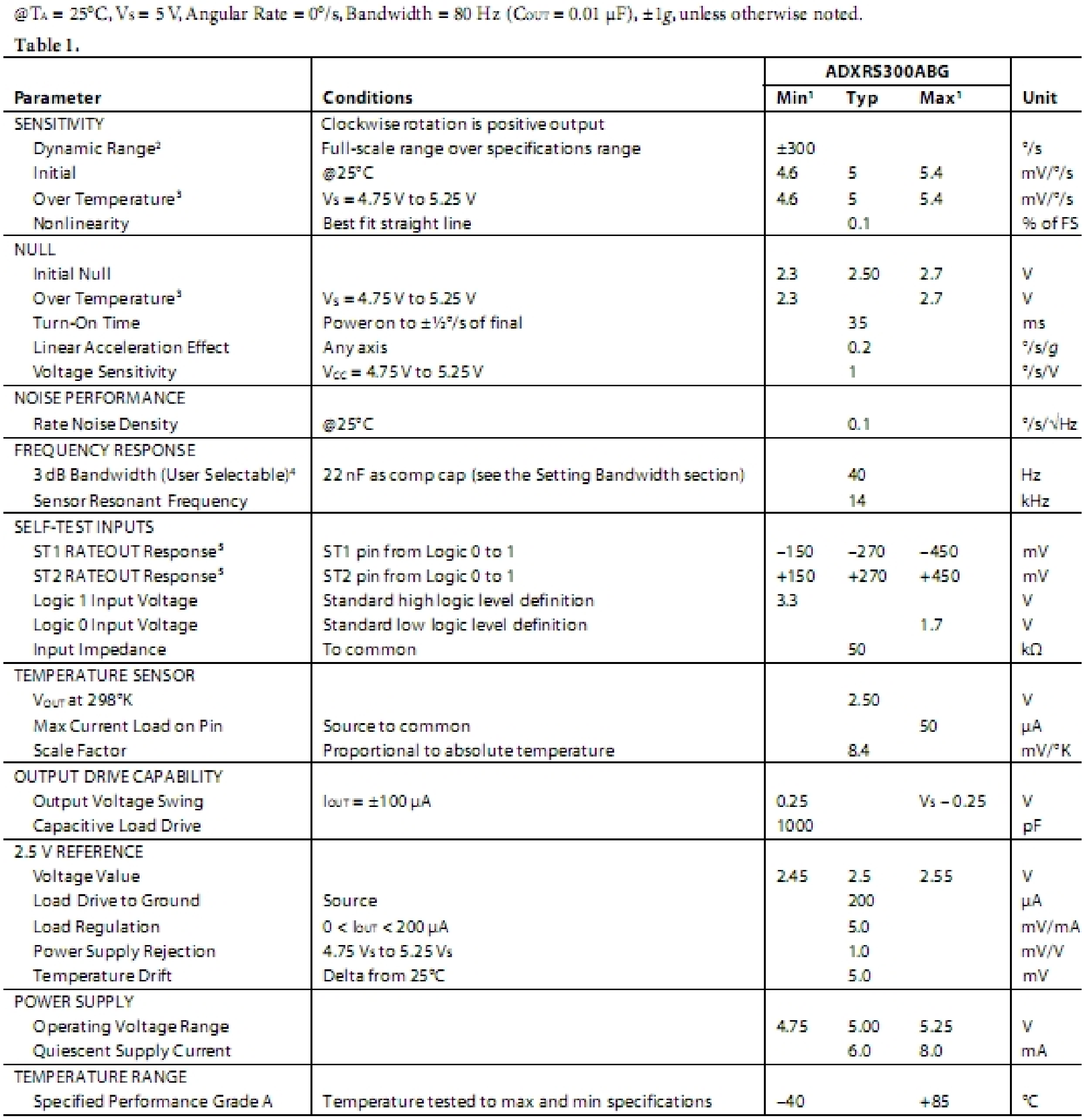

@T_A = 25°C, V_S = 5 V, Angular Rate = 0°/s, Bandwidth = 80 Hz (C_{OUT} = 0.01 µF), ±1g, unless otherwise noted.

Table 1.

Parameter	**Conditions**	**ADXRS300ABG**			**Unit**
		Min[1]	**Typ**	**Max**[1]	
SENSITIVITY	Clockwise rotation is positive output				
Dynamic Range[2]	Full-scale range over specifications range	±300			°/s
Initial	@25°C	4.6	5	5.4	mV/°/s
Over Temperature[3]	V_S = 4.75 V to 5.25 V	4.6	5	5.4	mV/°/s
Nonlinearity	Best fit straight line		0.1		% of FS
NULL					
Initial Null		2.3	2.50	2.7	V
Over Temperature[3]	V_S = 4.75 V to 5.25 V	2.3		2.7	V
Turn-On Time	Power on to ±½°/s of final		35		ms
Linear Acceleration Effect	Any axis		0.2		°/s/g
Voltage Sensitivity	V_{CC} = 4.75 V to 5.25 V		1		°/s/V
NOISE PERFORMANCE					
Rate Noise Density	@25°C		0.1		°/s/√Hz
FREQUENCY RESPONSE					
3 dB Bandwidth (User Selectable)[4]	22 nF as comp cap (see the Setting Bandwidth section)		40		Hz
Sensor Resonant Frequency			14		kHz
SELF-TEST INPUTS					
ST1 RATEOUT Response[5]	ST1 pin from Logic 0 to 1	−150	−270	−450	mV
ST2 RATEOUT Response[5]	ST2 pin from Logic 0 to 1	+150	+270	+450	mV
Logic 1 Input Voltage	Standard high logic level definition	3.3			V
Logic 0 Input Voltage	Standard low logic level definition			1.7	V
Input Impedance	To common		50		kΩ
TEMPERATURE SENSOR					
V_{OUT} at 298°K			2.50		V
Max Current Load on Pin	Source to common			50	µA
Scale Factor	Proportional to absolute temperature		8.4		mV/°K
OUTPUT DRIVE CAPABILITY					
Output Voltage Swing	I_{OUT} = ±100 µA	0.25		V_S − 0.25	V
Capacitive Load Drive		1000			pF
2.5 V REFERENCE					
Voltage Value		2.45	2.5	2.55	V
Load Drive to Ground	Source		200		µA
Load Regulation	0 < I_{OUT} < 200 µA		5.0		mV/mA
Power Supply Rejection	4.75 V_S to 5.25 V_S		1.0		mV/V
Temperature Drift	Delta from 25°C		5.0		mV
POWER SUPPLY					
Operating Voltage Range		4.75	5.00	5.25	V
Quiescent Supply Current			6.0	8.0	mA
TEMPERATURE RANGE					
Specified Performance Grade A	Temperature tested to max and min specifications	−40		+85	°C

Figure 2.19: ADXRS300 specifications taken from [28]

CHAPTER 3

PERFORMANCE OF THE ADXRS300 IN HARSH ACOUSTIC ENVIRONMENTS

In this chapter, a discussion of how the ADXRS300 is affected by mechanical shock, vibration, and acoustic energy is presented. These factors can all impact a MEMS gyro's performance.

3.1 Harsh Acoustic Environments

This section will provide some background information on how harsh environments affect MEMS devices in general and how the ADXRS300 compensates for this in its design.

3.1.1 Design Considerations

When considering vibration, acoustic noise, and mechanical shock levels, we must pay attention to frequency bandwidth. Often the specified and/or measured environments are limited to a bandwidth of less than 10 kHz. However, for the purpose of designing for MEMS sensors, we need to measure frequency content to more than 10 kHz. For most applications a 20 kHz bandwidth is sufficient. Measurement of shock and vibration in this frequency range requires special care because much of the equipment in the industry is designed for less than 5 kHz. It is important to know what steady-state acceleration (g) levels the IMU will be exposed to. The isolated body requires sufficient space to move within the part of the system that is rigidly mounted. This amount of space, or sway space, is a function of the natural frequency of the isolator and the magnitude of the input acceleration. The lower the natural frequency of the isolator and the higher the g level, the more sway space that is required. Also, the need for increased sway space implies increased stress and strain on the isolator at full load. We can easily predict how much sway space is required if we assume that the isolated system will behave like a single-degree-of-freedom, second order system. Bottoming out of the isolation system not only eliminates the benefit of isolation but it can also send an unattenuated shock pulse directly into the MEMS sensors. This may result in severally degraded system performance as well as damage to the MEMS sensors. The equation for sway space is shown in Fig. 3.1.

$$X_S = \frac{A \cdot g}{(2\pi F_n)^2}$$

Where: X_s = sway space
A = acceleration in g units
g = Earth's gravity (in sway space units per seconds squared)
F_n = isolator natural frequency in cycles per second

Figure 3.1: Sway space equation

If the acoustic environment is particularly severe it may be necessary for the IMU to incorporate an internal isolation system. The choice between internal and external isolation may also be driven by size constraints. These two basic isolation schemes are shown in Fig. 3.2.

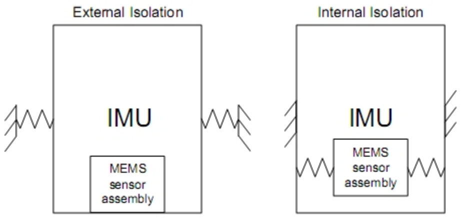

Figure 3.2: Isolation schemes

One very important aspect of isolator design is the elastomer formulation. When choosing the elastomer material it is very important to consider the operating temperature range. The material properties of elastomers have a much wider variation as a function of temperature than typical engineering materials (metals, epoxy resins, etc.). There are various choices of elastomers that will perform over a variety of temperature ranges. In general, an isolation system properly designed for a limited temperature range will have higher performance than an isolation system designed for extreme temperatures. Also, knowing the thermal rate of change is required since the isolation system can affect the thermal time constant and minimize thermal gradients across the MEMS sensors.

The second requirement is to determine the vibration frequencies and amplitudes to which the MEMS sensors are sensitive. Since MEMS sensors are mechanical systems, energy at certain frequencies can couple in and disrupt either the drive or sense loops. When enough energy is present, these loops can go unstable and performance can be degraded. At certain frequencies and levels these loops can be so unstable that temporary and permanent damage to the sensors can occur. Since each MEMS sensors has unique modes, each with a unique Q (or damping ratio), the designer must determine which MEMS sensors the IMU will use. When dealing with MEMS sensors that are highly dampened (low Q) and/or with sensitive excitation frequencies higher than the environment can excite, the need for isolation diminishes. Since low-damping is equal to a high Q, when dealing with MEMS sensors that have little damping (high Q's) and/or with sensitive frequencies within the frequency range of exposure, the need for isolation increases. Typically in these IMU's the lower the sensitive frequencies and the higher the Q's the more isolation is required. Additionally, when the MEMS sensors are underdamped (Q greater than 5,000) then the isolation system is extremely critical and requires increased design margin to assure proper IMU performance. Since a MEMS IMU can employ multiple technologies, different for accelerometers and rate sensors, the isolation system must be designed to maximize the performance of the entire IMU.

Mass properties are critical parameters since they play an important roll in the design of the isolation system. A 3-degree of freedom system can have different masses, but this is usually undesirable. The mass is used, in conjunction with the spring constant, to determine the three axial natural frequencies of the system. Since the goal is to minimize the delta between each of the axial natural frequencies, we need to design the isolation system to have the same spring constant in the 3 axial degrees of freedom. Therefore, to adjust the natural frequencies we can either adjust the material properties or adjust the mass of the isolated body. The equation for isolator natural frequency is shown in Fig. 3.3.

$$F_n = \frac{1}{2\pi}\sqrt{\frac{k}{m}}$$

Where: F_n = isolator natural frequency in cycles per second
K = spring rate of the isolator
M = mass of the isolated body (in units consistent with spring rate units)

Figure 3.3: Natural frequency equation

Inertia is also an important parameter since we need to control the three radial natural frequencies of the isolation system. These radial natural frequencies are less important than the axial natural frequencies but they still need to be known and controlled. The goal is to design the isolation system to minimize the delta between the 3 radial natural frequencies as well as place them near the axial natural frequencies. And since the inertias of the isolated portion are seldom symmetric in the 3 degrees of freedom, the isolation system geometry is the most appropriate method to adjust the radial frequencies. Also, note that larger isolation schemes allow for lower radial frequency systems and visa versa.

The center of gravity of the isolated body is also very important and needs to be known and controlled. We need to align this center of gravity with the isolation system's center of elasticity. The center of elasticity is the three dimensional point, or node, in which the isolation system reacts. We want to align these two points as best as possible. If these points are not aligned, axial vibration can generate rocking, coning, and/or skulling of the isolation system, which can degrade performance. By minimizing the offset between these two points we can maximize the MEMS IMU performance.

From knowing all the required information, a designer can determine the proper parameters of the isolation system. The most important parameters are the natural frequency of the isolation system and its Q, or damping, and how both these parameters vary as a function of all the others. Once these two parameters are established, everything else can be tweaked by changing the isolator's material properties and geometry. By using the transmissability equation in Fig. 3.4, the effects of altering the natural frequency or Q can be determined from the system's response [29].

$$T = \sqrt{\frac{1+\left(2\zeta\frac{\omega}{\omega_n}\right)^2}{\left(1-\frac{\omega^2}{\omega_n^2}\right)^2+\left(2\zeta\frac{\omega}{\omega_n}\right)^2}}$$

Where: T = transmissibility (unit less)
ζ = damping ratio (unit less) = $\frac{1}{2Q}$
ω = frequency in radians per second
ω_n = natural frequency in radians per second

Figure 3.4: System response

3.1.2 Error Sources in the ADXRS300

Analog Devices began their gyro development with the ground rules that the instrument should be inexpensive and it should satisfy automotive applications. To minimize expense, ADI's accelerometer CMOS and polysilicon process was mandated. In the mid-1990s, the process focused on 2-μm-thick suspended parts. Based on performance considerations, Analog has moved to 4-μm thick suspended polysilicon parts. The 4-μm thickness results in smaller moving parts, shorter beams, and smaller deflections compared to other commercially available tuning fork gyros (TFG's). To incorporate on-chip circuitry, the substrate must be silicon. The moving elements, electrical traces, and bonding pads are isolated from the conducting silicon substrate by an oxide layer. The gyro mechanism consists of two independent mechanical structures.

For each structure, the inner member is driven and sensed electrostatically. The sensing frame supports the driven member. An angular rate about an axis perpendicular to the substrate moves the driven mass along the sense direction, which is parallel to the substrate plane. As discussed below, the suspension is designed so that the sensing frame does not move in the drive direction, but follows the proof mass in the sense direction. Electrostatic combs detect the frame position. Eliminating trimming to reduce quadrature error was a dominant decision in ADXRS design. With crab leg or folded beam suspension, differing beam stiffnesses can cause sense-axis motion when driving the proof mass. Because this motion is in phase with displacement, it is in quadrature to the desired rate-induced motion. The ADXRS beam widths are 1.7 μm, and width tolerances are 0.2 μm so that quadrature reduction was a major design goal. Straight beams between the sense and drive elements result in very little sense-axis motion. The beams have stress relief at their ends to reduce longitudinal stresses from polysilicon thermal expansion and from drive motion. Although ADI has not employed it, a fine quadrature trim is possible by fingers excited to exert a sense force that is modulated by the drive motion. In the ADXRS, both the sense and drive motions are parallel to the substrate's plane; thus, all critical dimensions are done in one masking and etching operation. If the polysilicon thickness is off, all frequencies move together so that mode ordering is maintained. While the proof mass is driven at a 7-μm amplitude, the sense motion for angular rate is roughly 10^{-10} μm/rad/s, an order of magnitude lower than for TFG's. This smaller motion is attributed to smaller drive amplitude, the fact that the drive mass must also drive the additional sense mass, and 20 to 30 percent separation of sense and drive resonant frequencies. The greater separation is consistent with a 2-μm beam width and with a 4-μm thickness and the resulting proof mass and suspension dimensions. The gyro consists of two mechanically independent mechanisms whose drive frequency is roughly 14 kHz and whose quality factor is 45. The units are electrically cross-connected so that the proof masses move anti-parallel to common mode reject linear acceleration. To achieve common mode rejection with a Q of 45, the two drive resonant frequencies should be within 1 percent of each other. If the moving drive teeth are not centered with respect to the stationary teeth (i.e., the entire proof mass is moved relative to the stationary combs), a large coupling to sense force results. Since the drive force is large because of the high damping and since the drive force is in phase with the drive velocity and, hence, the Coriolis acceleration, the proof mass must be centered to very tight levels. With 1.7-μm-wide beams, achieving the geometric control for sense drive frequency separation, matching drive frequencies, and centering the combs is challenging. The ADXRS is hermetically sealed at 1 atmosphere. Because of the resulting damping, noise is limited by Brownian motion. To achieve drive amplitude, the 5-V supplies must be boosted to approximately 12 V. Damping adds phase shift between sense and drive axes. Electronics design and increasing separation between sense and drive frequencies reduce the effect of this additional phase shift. The resulting damping renders the ADXRS tolerant of operating shock. The ADXRS relies heavily on its on-chip electronics to overcome the small size and low scale factor of the mechanical parts. The sense displacement per rate input is 10 percent and the capacitance variation is 1 percent of the 20-μm thick TFG's. Analog measures displacement resolution similar to the TFG's, but with much smaller capacitors [30].

3.1.3 Shock and Vibration

The MEMS tuning fork gyro (TFG) is an electromechanical device that measures angular rotation rate. A proof-mass attached to springs is forced to oscillate in the horizontal plane.

A voltage is applied to a sensing electrode (sense plate) below the proof mass, creating an electrical field. The Coriolis force imparted by angular rotation causes the proof-mass to oscillate in the vertical direction, which, in turn, changes the gap between the proof mass and the sense plate. This generates an AC current with amplitude proportional to the rotation rate. The bias voltage also generates an electrostatic force between the proof mass and the sense plate. This force acts to pull the proof mass toward the sense plate as shown in Fig. 3.5.

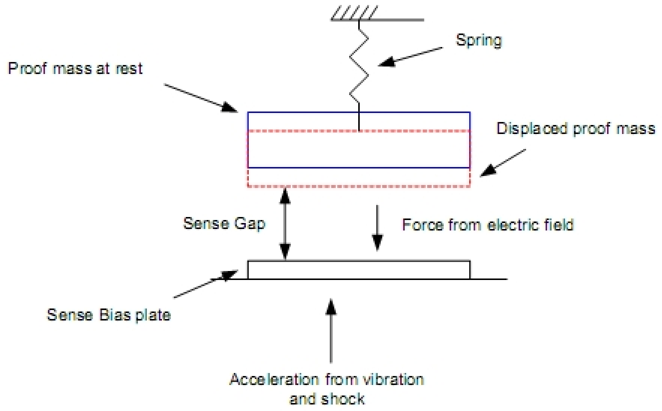

Figure 3.5: MEMS gyro schematic with forces

If the sense gap gets too small, a catastrophic failure will occur when the proof mass touches the sense plate. Since the gyro is a mechanical device, it is sensitive to external stimuli. These stimuli include vibration, acoustic excitation, and acceleration due to mechanical shock. For some applications, the acceleration levels at the gyro can be as large as 500 g's. These stimuli will increase or decrease the sense gap depending on amplitude and frequency. Additionally, as the rotation rate increases, the sense gap decreases. In order to successfully operate at high rates (up to 50 revolutions per second) and in high g environments, the maximum proof mass displacement (minimum sense gap) must be determined.

The sense bias voltage and the motor amplitude can be used to control the maximum displacement but, if the maximum displacement is exceeded, snap-down will occur. Proof mass snap-down is a catastrophic failure that occurs when the electrostatic force between the proof mass and the electrode is larger than the restoring force provided by the springs that suspend the proof mass. When this happens, the proof mass touches the sense plate and the gyro has snapped-down. The minimum sense gap required to prevent snap-down can be determined for each gyro design and is affected by the factors listed in Fig. 3.6 [32].

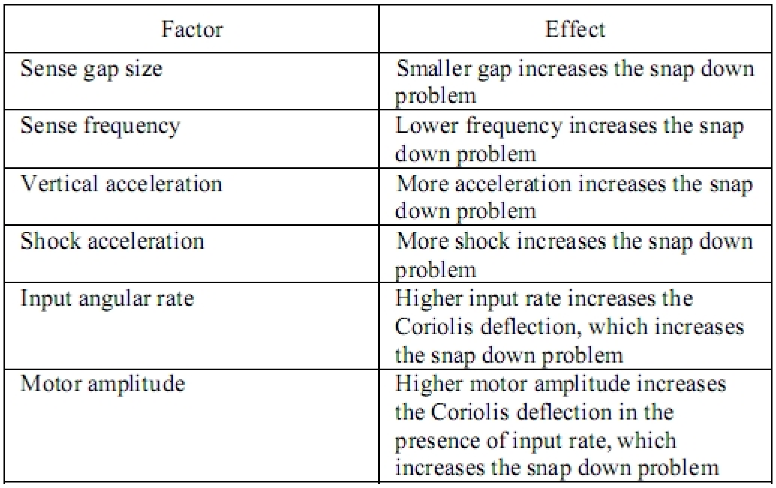

Factor	Effect
Sense gap size	Smaller gap increases the snap down problem
Sense frequency	Lower frequency increases the snap down problem
Vertical acceleration	More acceleration increases the snap down problem
Shock acceleration	More shock increases the snap down problem
Input angular rate	Higher input rate increases the Coriolis deflection, which increases the snap down problem
Motor amplitude	Higher motor amplitude increases the Coriolis deflection in the presence of input rate, which increases the snap down problem

Figure 3.6: Factors affecting snap-down phenomenon

The ADXRS gyros employ a novel approach to angular rate-sensing that makes it possible to reject shocks of up to 1,000 g. They use two resonators to differentially sense signals and reject common-mode external accelerations that are unrelated to angular motion. This approach is, in part, the reason for the excellent immunity of the ADXRS gyros to shock and vibration. The two resonators are mechanically independent, and they operate anti-phase. As a result, they measure the same magnitude of rotation, but give outputs in opposite directions. Therefore, the difference between the two sensor signals is used to measure angular rate. This cancels non-rotational signals that affect both sensors. Thus, extreme acceleration overloads are largely prevented from reaching the electronics, thereby allowing the signal conditioning to preserve the angular rate output during large shocks. This scheme requires that the two sensors be well-matched, precisely fabricated copies of each other [31].

3.2 Evaluation Goals

The main goal of this research effort is to determine the typical response of the ADXRS300 MEMS gyro in an acoustically harsh environment. It is commonly known that the ADXRS300 can be adversely affected by high frequency mechanical vibrations and sufficiently loud acoustic noise, but the average or typical response of this device in this harsh environment has not been quantified. The following sections will address this by attempting to answer these questions:

- Is the frequency or amplitude of the sine wave in the output signal sound level dependent?
- How close above and below the resonant frequency of the sensor does this occur?
- Does it occur at the two other minor resonant frequencies?
- What happens if a two-tone signal is applied, where one tone is above and one below the resonant frequency?
- Does a single tone far away from the resonant frequencies have any effect on the gyro output at any realistic sound power level?

For each test case, the mean and standard deviation for each set of gyros will be computed. The mean equates to the bias voltage and output signal components of the gyro output. The standard deviation would be related to the noise in the output signal. For all the tested gyros, a distribution plot of the standard deviation will be developed for each case.

This should then reveal the variance in the ADXRS300 performance in an acoustically harsh environment. From this set of graphs and data, performance trends can then be ascertained accordingly.

3.3 Evaluation Procedure and Setup

This section will describe in detail the procedures and equipment used for the experiments.

3.3.1 Overall Procedure

Twenty-four Analog Devices ADXRS300 were acquired for testing. These were standard packages ordered via Digi-Key. Once the gyros were gathered, an evaluation board was designed to accommodate the testing. Essentially, access to the gyro's rate output signal and self-test inputs were required. Also, the boards were designed to provide power and signal conditioning along with easy daisy-chaining of multiple boards. These boards were then fabricated externally. The ADXRS300 chips were then assembled on the boards in-house at Auburn University. One of the boards was designated as a control board and was labeled board "1". The boards were then separated into groups (A through E) of three or four, with the control board number "1" as a member of each group. The groups were then attached to an aluminum CDG plate via screws. Consequently, the plate was mounted on an industrial rate table which provided precision-controlled spinning of a group of boards to stimulate a rate output from the gyros.

An acoustic sound chamber in Wilmore Labs housed the rate table. The rate table is bolted to an aluminum slab to provide stability to the system. Once inside the chamber, the signal lines are fed through the rate table to a port which leads outside the chamber.

Connected to the lines inside the chamber are power and ground signals from an analog power supply. The outside lines are then interfaced to the data collection equipment.

Inside the chamber, a three-dimensional speaker mount encloses the rate table. From above the rate table, the speakers used to generate the acoustic noise are positioned for maximum sound levels and a minimum of sound wave cancellation. A powered microphone and digital thermometer are also mounted in close proximity to the boards. The microphone is used to measure the sound pressure levels that the gyros are experiencing. The microphone's signal line is also fed though the port to the data collection center. The chamber is then sealed from the outside.

The data collection center consists of four main components: rate signal data collection, sound level data collection, noise generation, and rate table control. All four components are processed by two personal computers, audio amplifiers, and National Instruments data acquisition devices. Various software packages are used to control the process and will be discussed in a later section.

In a typical procedure, the rate table was activated, noise was generated, and data was collected.

3.3.2 Evaluation Boards

The ADXRS300 evaluation board is two-layer printed circuit board (PCB). The board was designed using The board was manufactured by Advanced Circuits (www.4pcb.com) in Aurora, Colorado. Fig. 3.7 shows the schematic for the board. The capacitor values CP1 - CP4 are charge pump capacitors for a 5V source. These can be omitted with a 15V source. The power pins each have a decoupling capacitor. CMID and COUT are used to set the output frequency bandwidth.

The physical board layout is shown in Fig. 3.8.

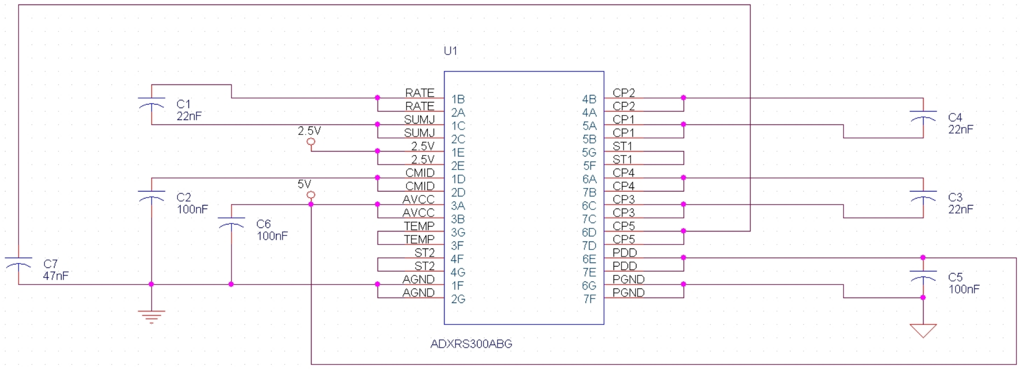

Figure 3.7: ADXRS300 board schematic

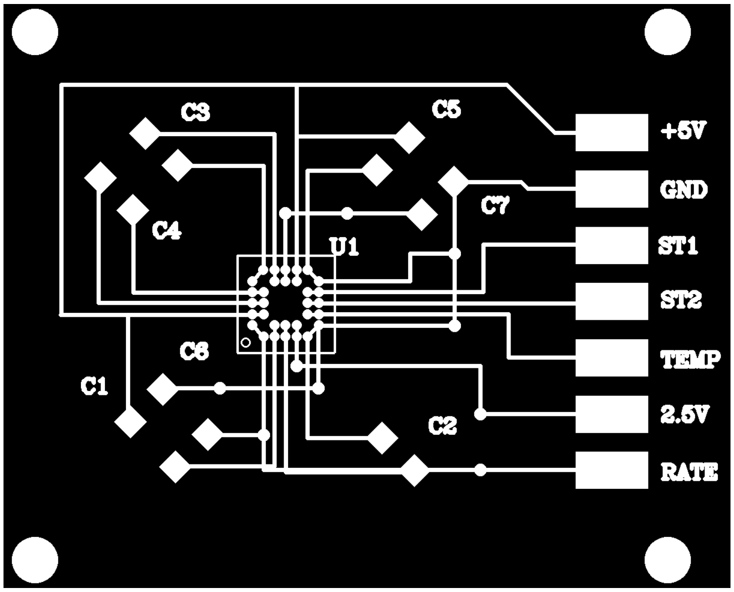

Figure 3.8: ADXRS300 board layout

The unpopulated evaluation board can be seen in Fig. 3.9. Each board is fitted with the appropriate 1206-size surface mount capacitors as shown in Fig. 3.10.

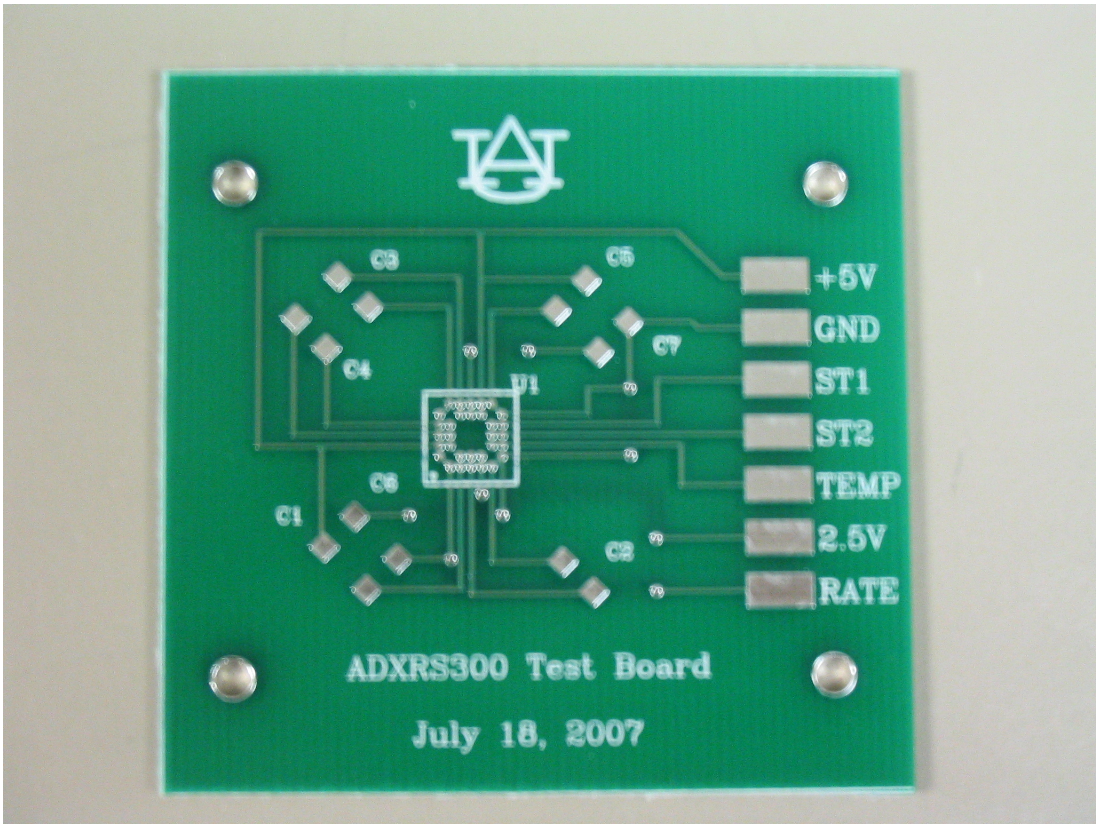

Figure 3.9: Unpopulated evaluation board photo

Next, a flip chip bonder with a split optic alignment system (Fig. 3.11) was used place the gyro on the board with solder balls accurately lined up on the pads.

Fig. 3.12 through Fig. 3.15 illustrate this process.

Next, the boards are sent through the reflow oven. The reflow oven melts the solder balls from the BGA array which self-align to the pads. The surface mount capacitors are attached in the same manner. The temperature profile shown in Fig. 3.16 was used.

The procedure for operating the reflow oven is shown in Fig. 3.17 through Fig. 3.21.

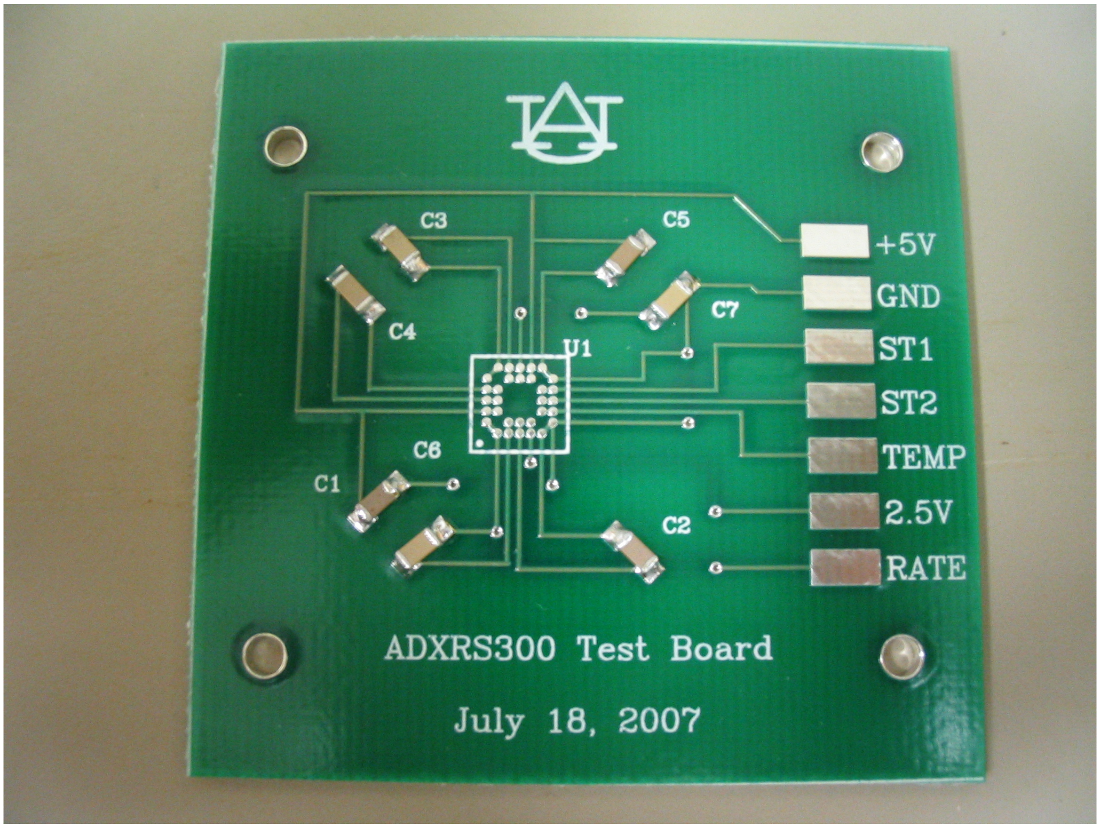

Figure 3.10: Evaluation board populated with capacitors

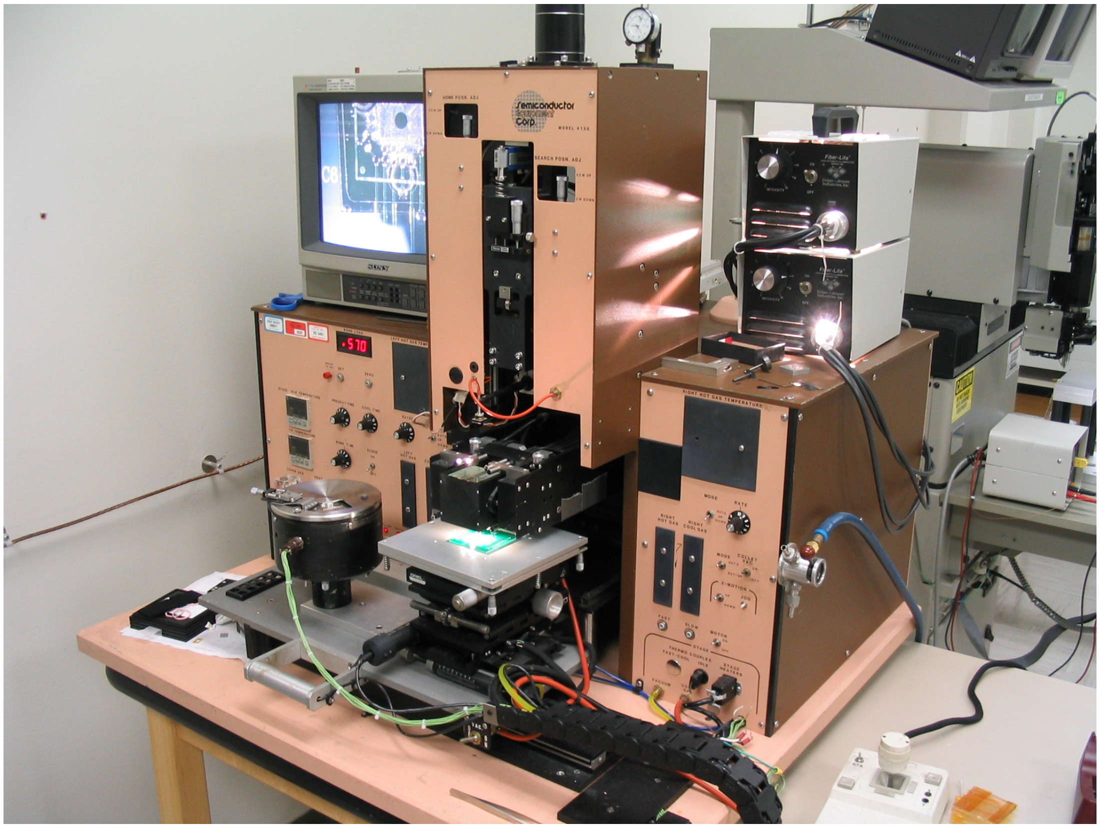

Figure 3.11: Flip chip bonder

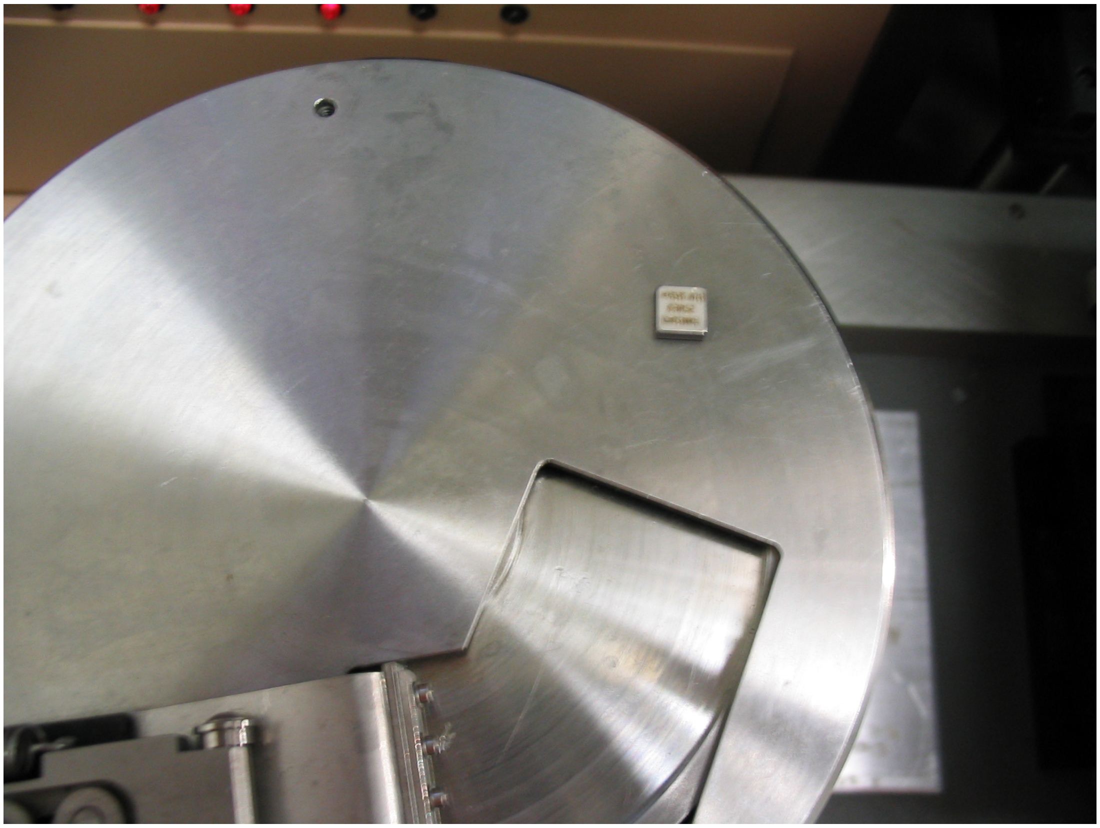

Figure 3.12: Chip placed on table

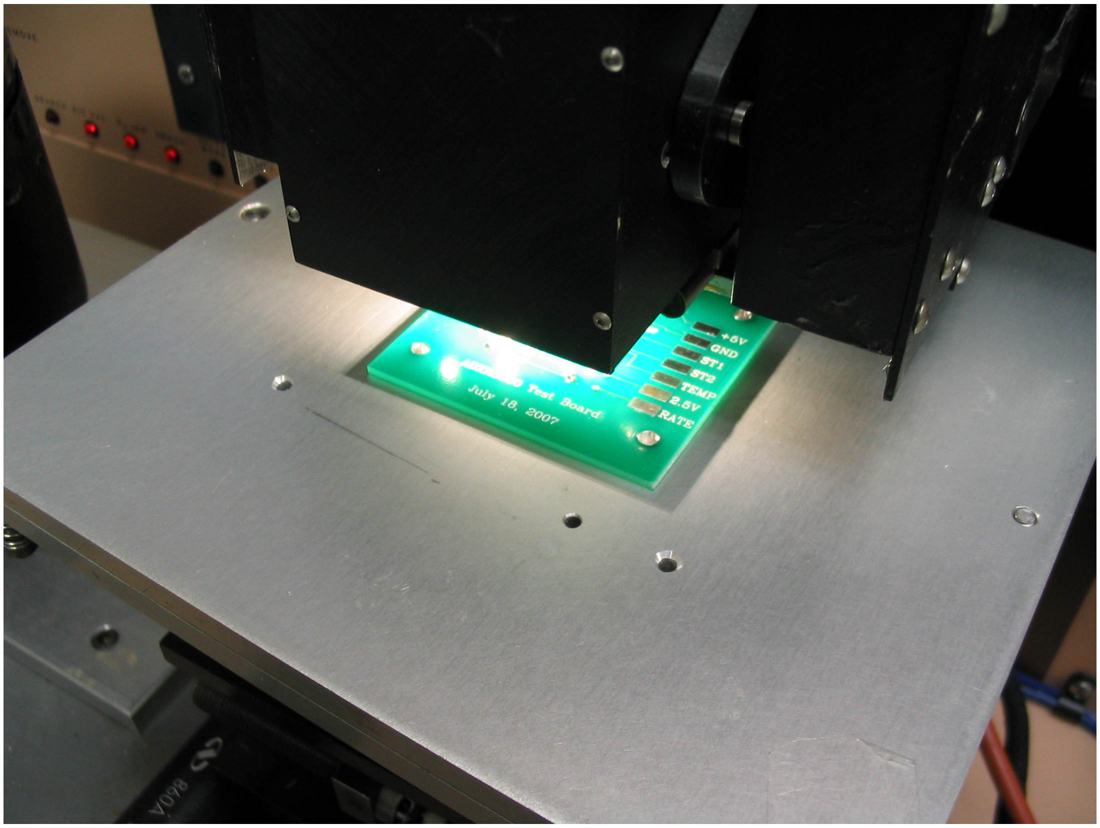

Figure 3.13: Board placed under camera

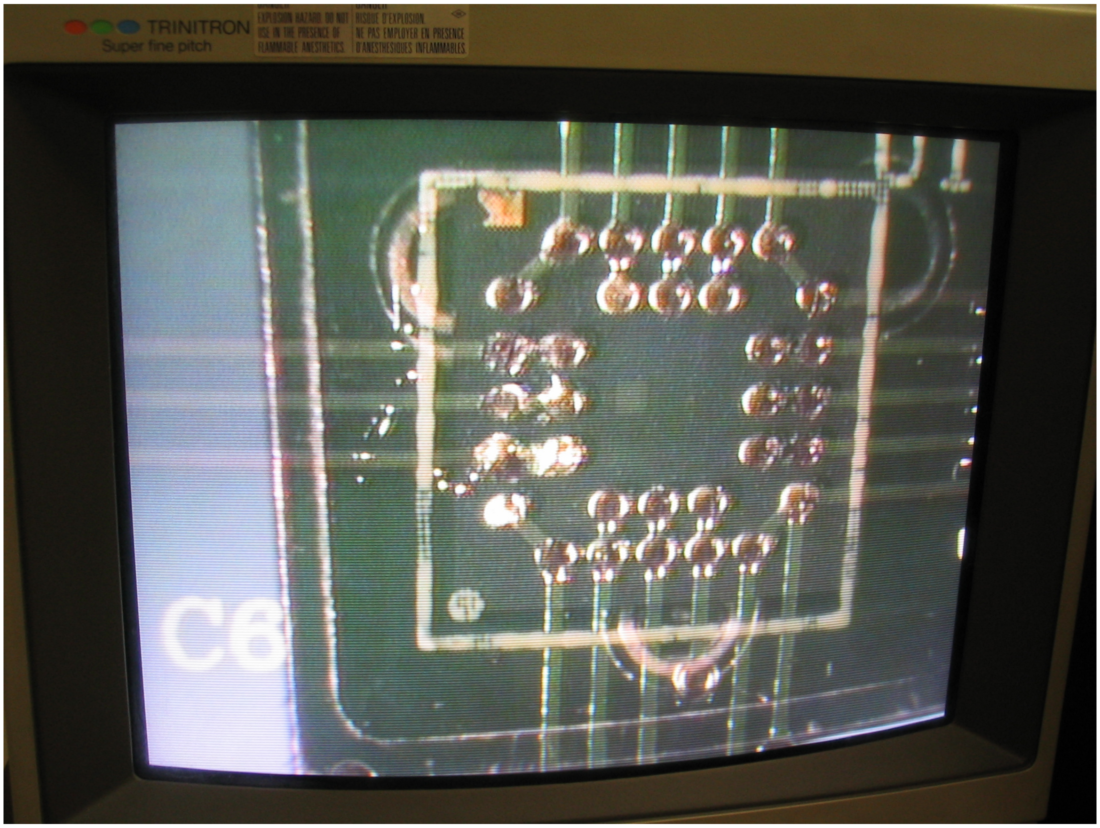

Figure 3.14: Aligning solder balls to the board pads

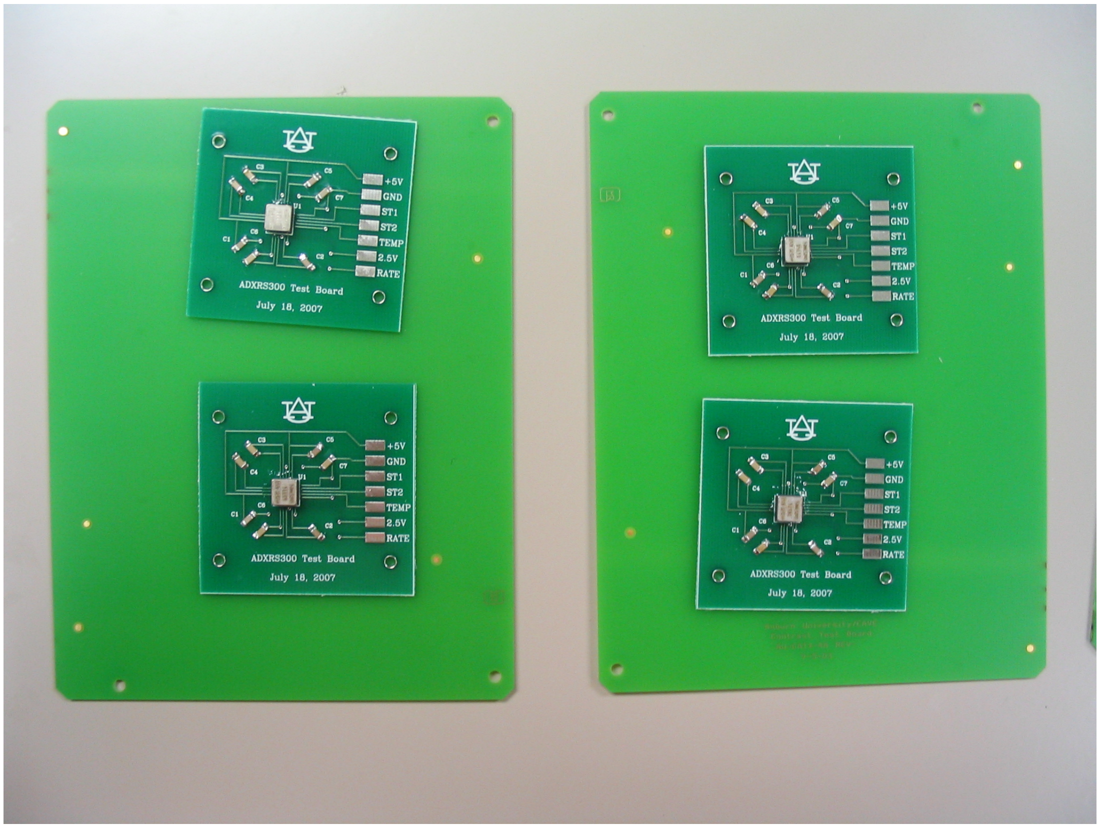

Figure 3.15: Chip successfully placed on board

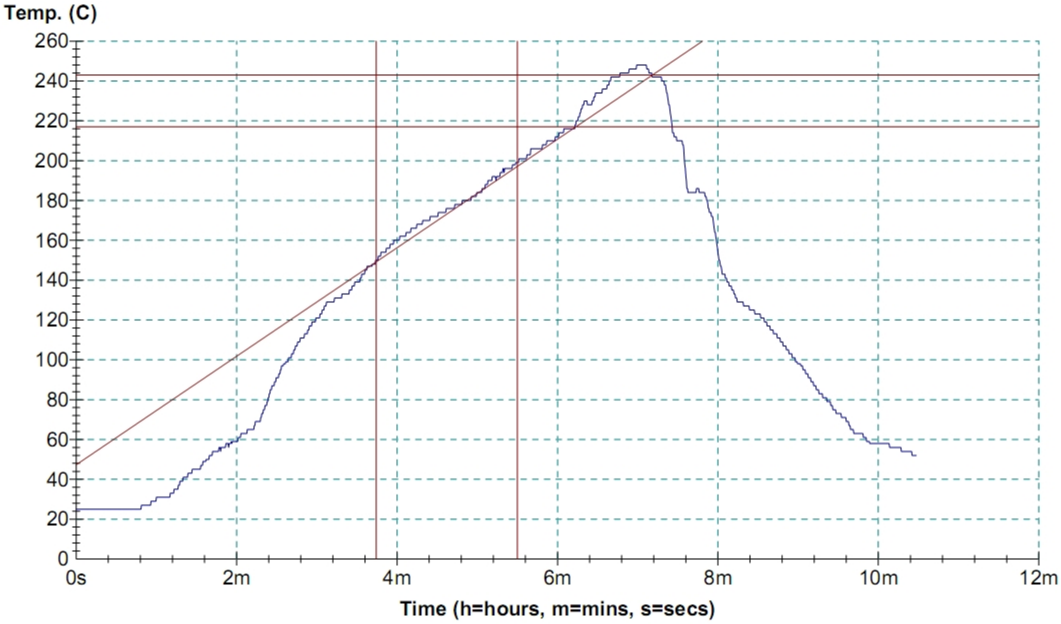

Figure 3.16: Reflow temperature profile

Figure 3.17: Packaging lab reflow oven

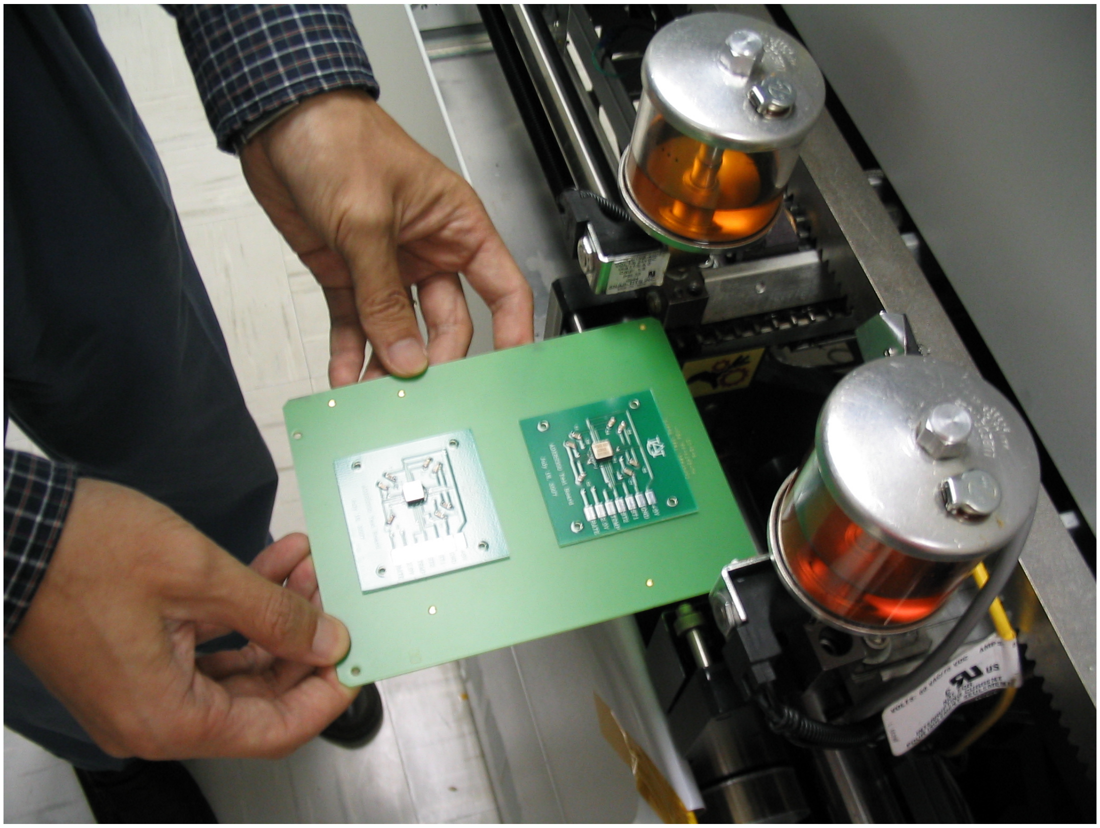

Figure 3.18: Ready for solder reflow

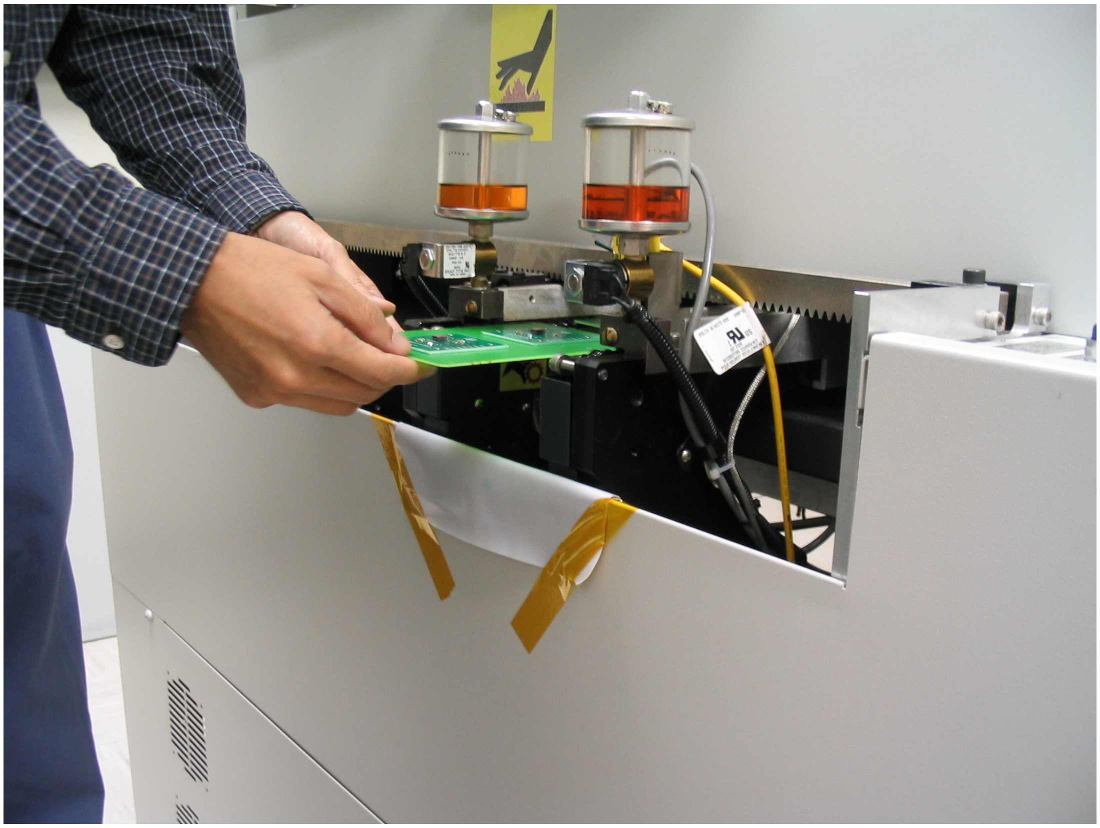

Figure 3.19: Placing board on the reflow oven belt track

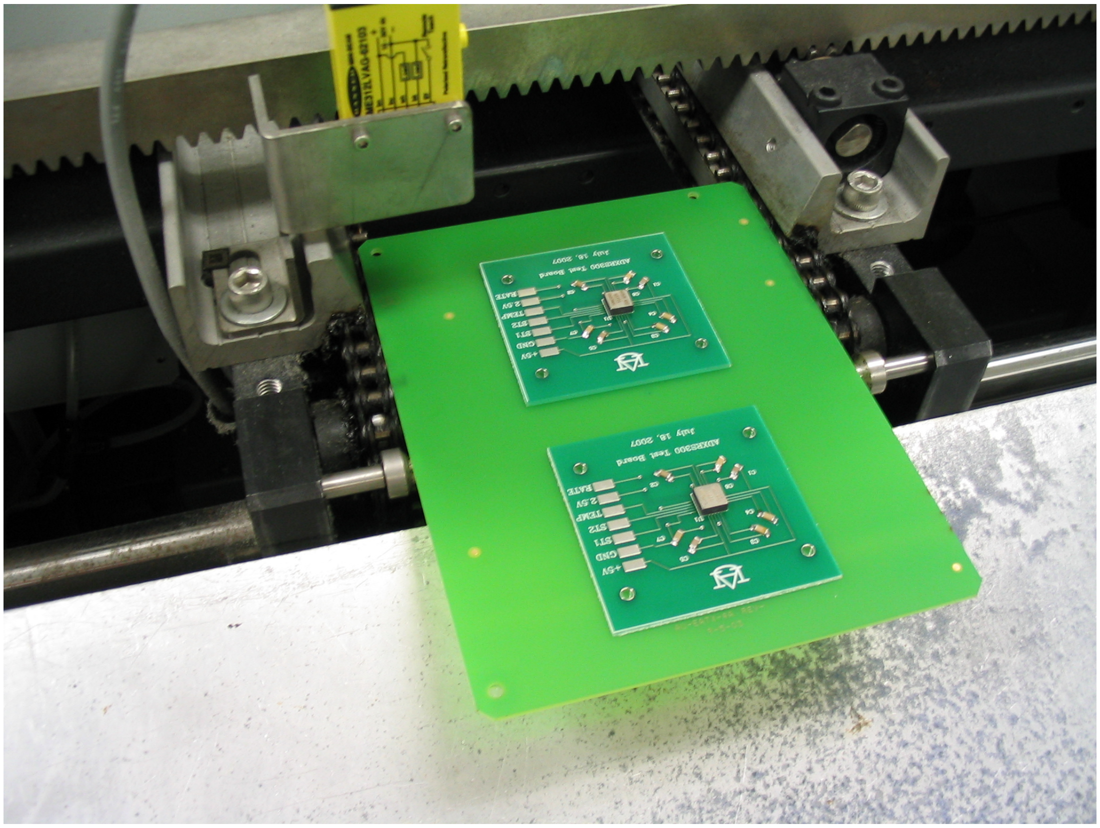

Figure 3.20: Finished boards exiting the reflow oven

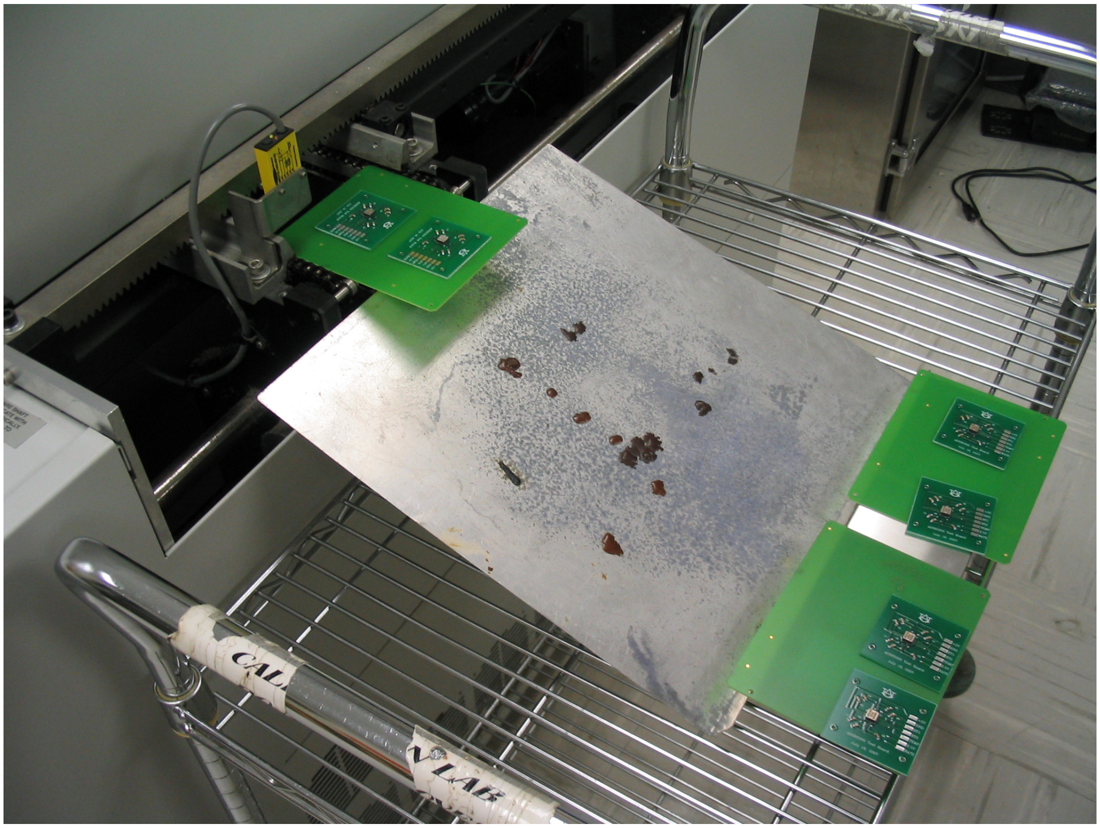

Figure 3.21: Boards cooling

Lastly, each board is tested to verify functional operation. Wires are soldered to all the signal and power lines. The boards are hooked up to a power supply and the output is measured with an oscilloscope. This is depicted in Fig. 3.22 and 3.24.

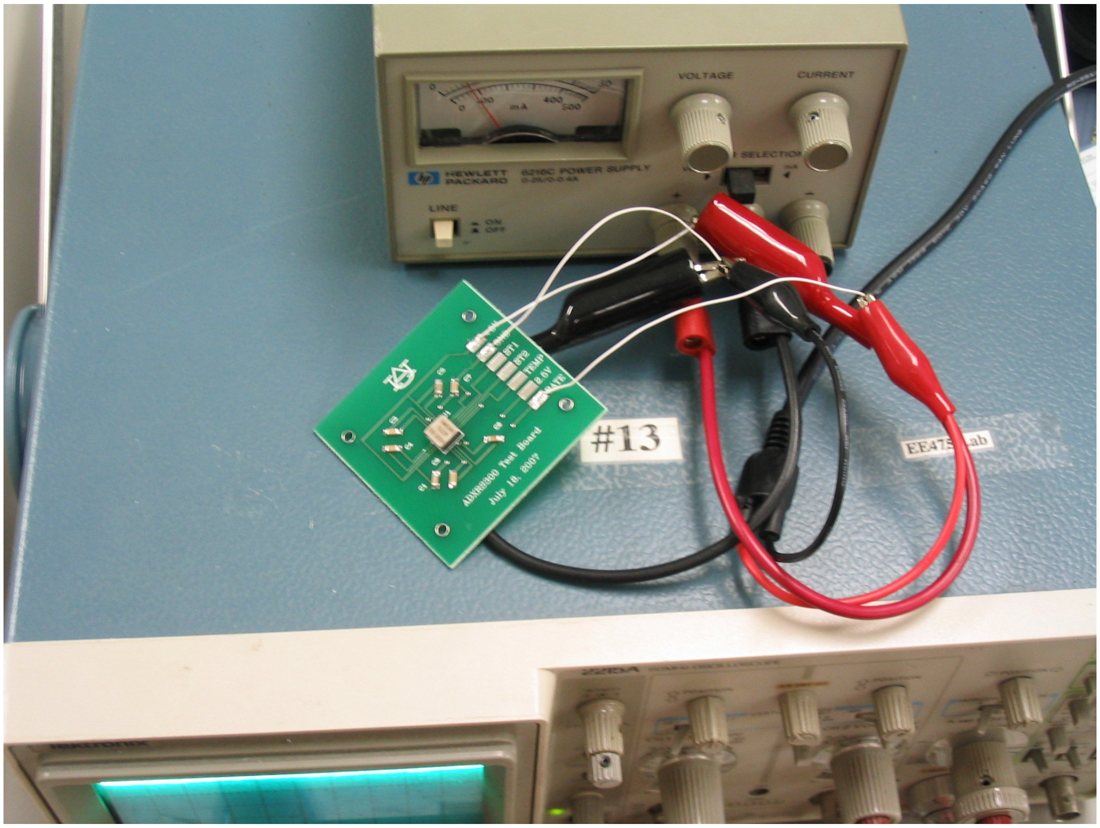

Figure 3.22: The board is connected to a voltage supply (5V)

3.3.3 Evaluation Facility

The acoustic chamber is located in Wilmore Labs on the Auburn University campus. The chamber itself is primarily made of wood. It is approximately 8 inches off the ground and is supported by a small number of legs to isolate the room from seismic and machine vibrations. The floor of the chamber rests on a bed of compressed air. This makes the chamber totally suspended from the ground. The chamber walls are insulated with fiberglass for further noise isolation. It also utilizes a double door system which has insulation

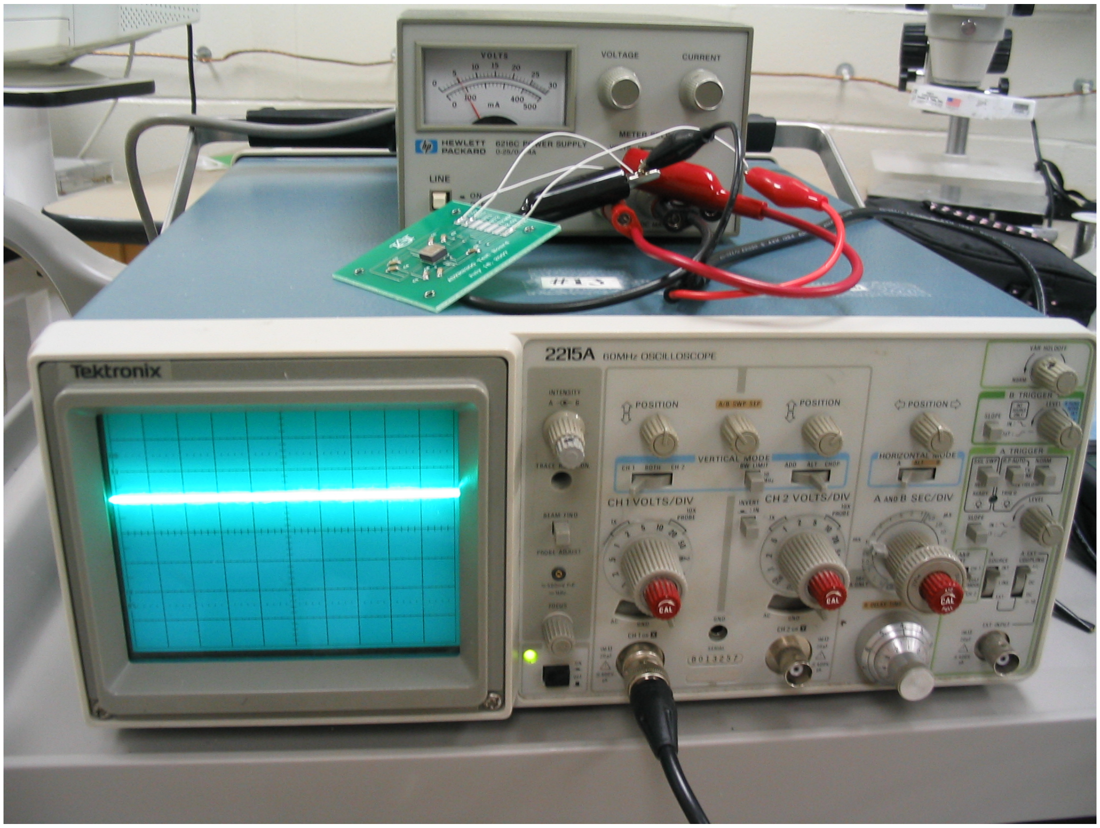

Figure 3.23: The rate output signal is measured with an oscilloscope

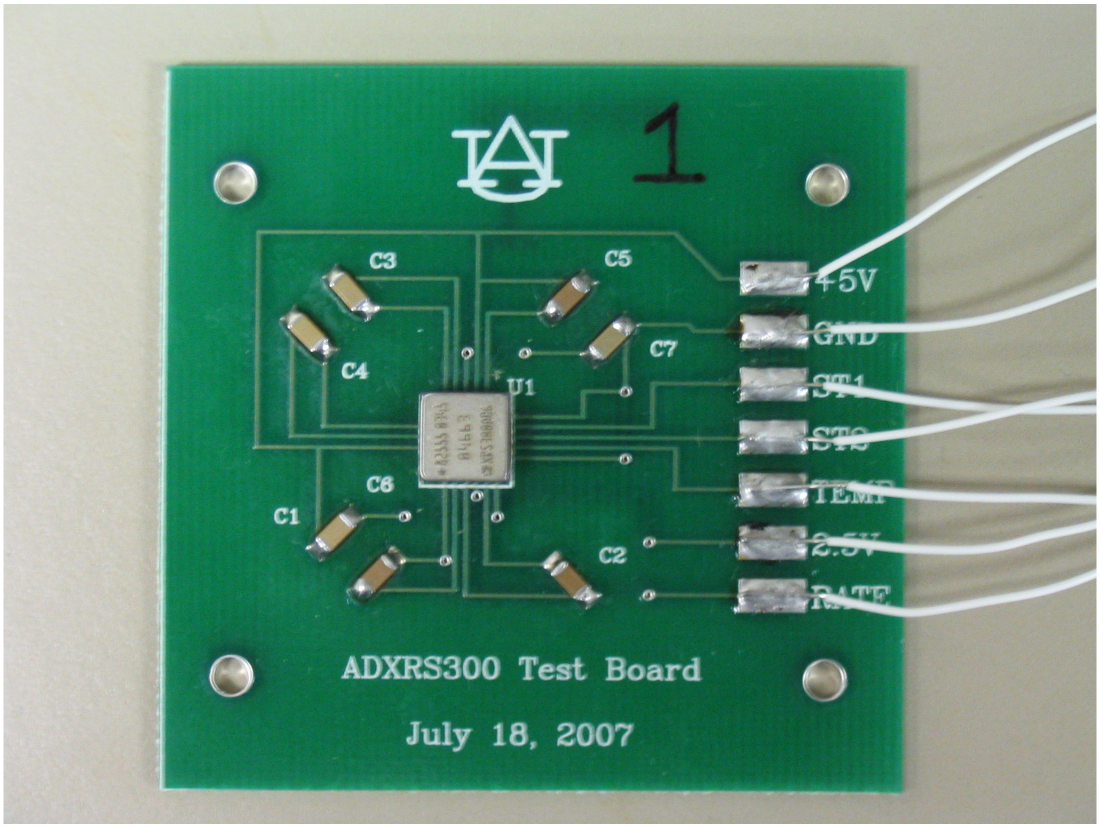

Figure 3.24: Fully Populated evaluation board

between the two doors when closed. There is a small circular port in room for external access. The chamber is shown in Figs. 3.25 and 3.26.

Figure 3.25: Acoustic chamber in Wilmore labs

3.3.4 Rate Table

The rate table used is based on the Aerotech ADR160 mechanical-bearing rotary stage. The ADR160 has a feedback rating of 23,600 lines/revolution. It also has a resolution of 13.1 μrad and an accuracy rating of +/- 24.3 μrad. 800 RPM's (17,280,000 deg/s) is its maximum rotary speed. It is a brushless direct-drive system [33].

Figure 3.26: Acoustic chamber with open doors

3.3.5 Speakers

Four speakers were used in the testing of the gyros. Two of the speakers are high-frequency drivers. There is also a mid-range driver and a low-frequency driver to encompass the acoustic spectrum (200-20 kHz). The mid-range speaker is a Community EM282 high power compression driver. It has a maximum output of 134 dB SPL (sound pressure level) and a frequency response of 1 to 12 kHz. The low-frequency Community M4 high power compression driver has a maximum output of 137 dB SPL and an operating range of 200 to 2000 Hz. The high-frequency Community VHF100 driver has a maximum output of 131 dB SPL and an operating range of 1.8 to 18 kHz. All four drivers have a nominal impedance of 8 Ω [34].

3.3.6 Audio Amplifiers

A pair of 2-channel Crown XTi1000 audio amplifiers are used to power the drivers. These amps are capable of outputting 275 W per channel with an operating range of 20 Hz to 20 kHz. Additionally, they have a signal to noise ratio of 100 dB [35].

3.3.7 Data Acquisition Device

For data acquisition purposes, the National Instruments 6143 multifunction DAQ is utilized. The device uses a PCI interface for connection to a PC. It has 8 analog inputs each capable of recording 250,000 samples/sec simultaneously. LabView software is used to collect the data. Five inputs, one from each gyro in a group, are connected to the DAQ and read into LabView. This setup allows for the collection of five gyro's rate output signals at the same time [36].

3.3.8 Microphone

For measuring the high intensity sound, the onmidirectional Endevco 8510B piezoresistive pressure transducer is used. This transducer employs a four-active arm strain gage bridge diffused into a sculptured silicon diaphragm providing capability for measurement from static pressure throughout the normal audio range. The microphone can measure sound pressure levels up to 181 dB with a 10 VDC supply source [37].

3.3.9 Equipment Setup

The first step in setting up the equipment involves arranging the testbed. The speaker mount is positioned around the rate table as shown in Fig. 3.27. This figure also shows the power supply for the microphone (in the foreground). Next, the drivers are positioned using the threaded bolts and accompanying nuts. The bolts are attached to the drivers with the nuts. The nuts additionally adjust the height of the drivers by positioning them through the pegboard at a specified length from the rate table. This configuration is illustrated in Fig. 3.28. Notice how the two high-frequency drivers are 180 degrees from each others. This arrangement provides an extra 3 dB of sound output as compared to a single driver which approximately doubles the power of the high frequency range sound. The speaker cables are then connected to the amplifiers and sent through the chamber port and into each driver. After the speakers are positioned, the reference gyro (1) is attached to the rate table with screws. The serial connector is connected to the appropriate signal lines through the table (see Appendix C for a circuit diagram of the wiring). Fig. 3.29 shows the reference gyro in place. Next, a gyro group such as the one seen in Fig. 3.30 is interfaced to both the table and the reference gyro (Fig 3.31). The microphone and thermometer are fed through the pegboard and are located as close to the gyros as possible. The thermometer ensures that there are no wild temperature fluctuations during testing. The microphone measures the average and peak sound pressure levels. The microphone is powered by 10 VDC with the output lines going outside the acoustic chamber. The digital thermometer and microphone can be seen in Figs. 3.32 and 3.33, respectively. Lastly, A ribbon cable is used to send all the output and input signal lines through the acoustic chamber's port. The lines are then connected to the NI DAQ units. One unit is for the microphone and another is for the gyros. Thus, two computers are used for collecting data. A 5 VDC supply is used to power the gyros from outside the acoustic chamber. Fig. 3.34 shows the data collection station used during testing. The double doors are closed prior to any testing.

The amplifiers have been programmed with the correct crossover frequencies and delay for each driver. Therefore, to achieve maximum output from the speakers, match the correct driver to the appropriate channel. The gain knobs may be turned to maximum settings safely. A multimeter can be connected to any channel output to monitor voltage spikes if necessary.

3.3.10 Data Collection and Sound Generation Software

This section provides a brief tutorial on the methods used for data collection. Once the PC's have booted up, the user will be presented with desktops on each. For gyro output data collection, four programs are important: NCH Tone Generator, gyro.exe, Gyros.vi,

Figure 3.27: Gyro testbed

Figure 3.28: Configuration of the four drivers relative to the rate table

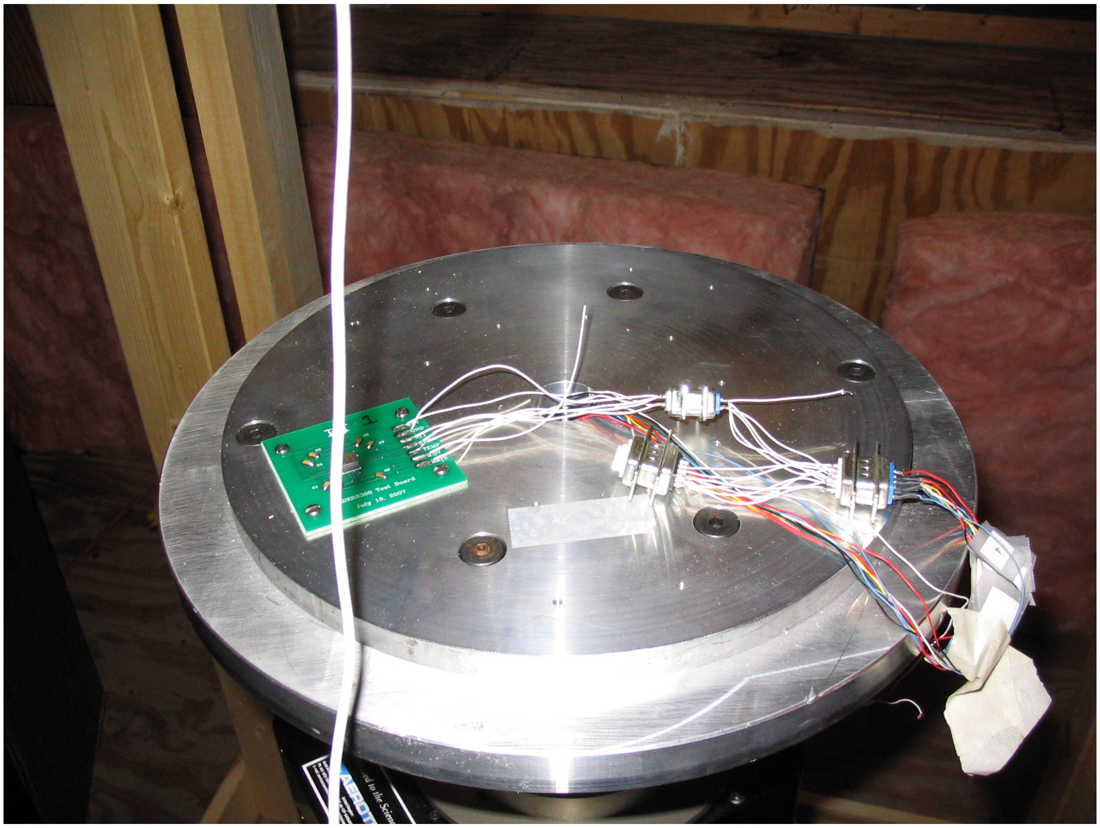

Figure 3.29: Reference gyro attached to the rate table

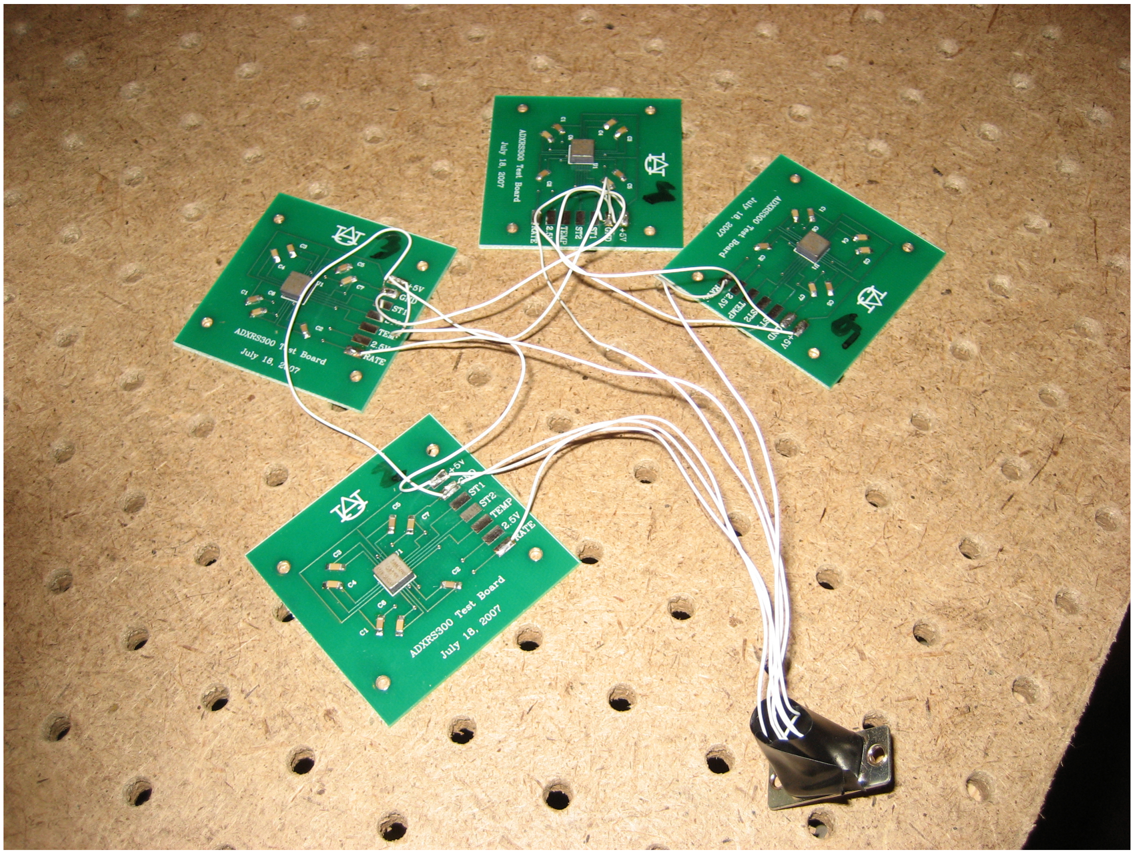

Figure 3.30: Assembled gyro group

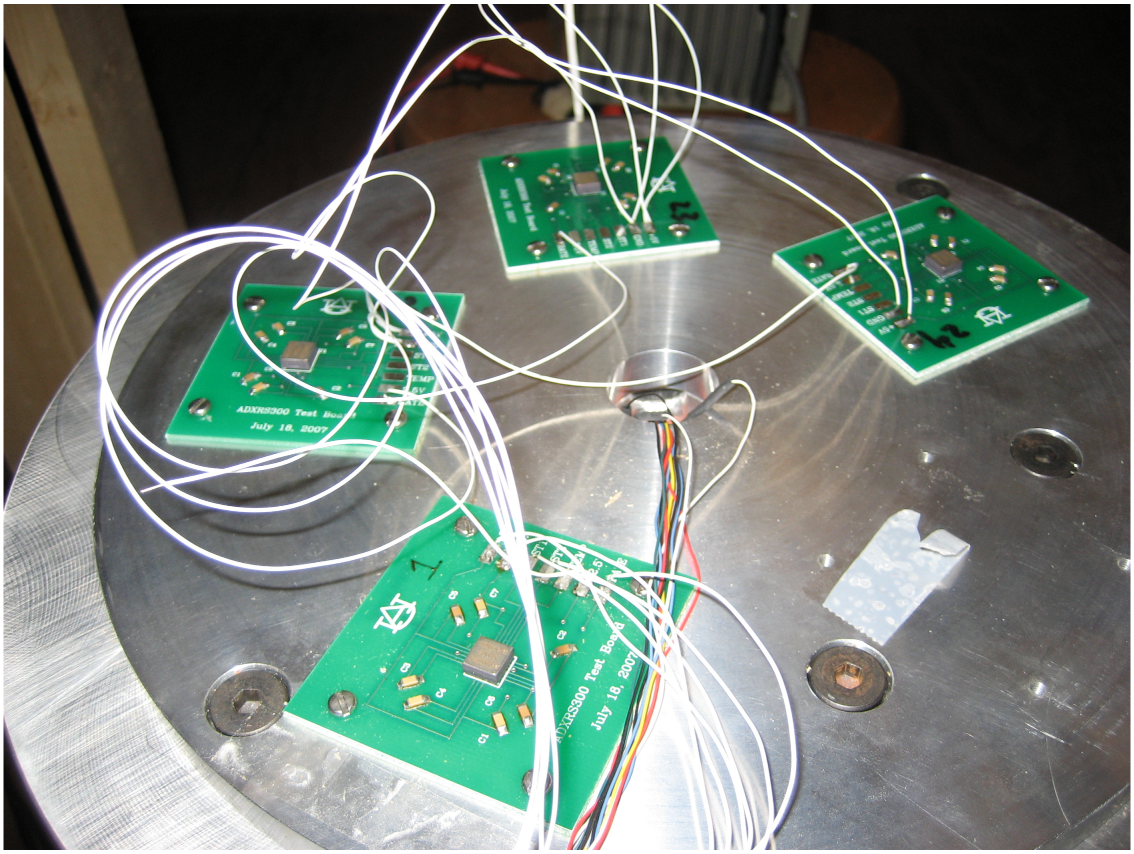

Figure 3.31: Reference gyro and group on table

Figure 3.32: Digital thermometer

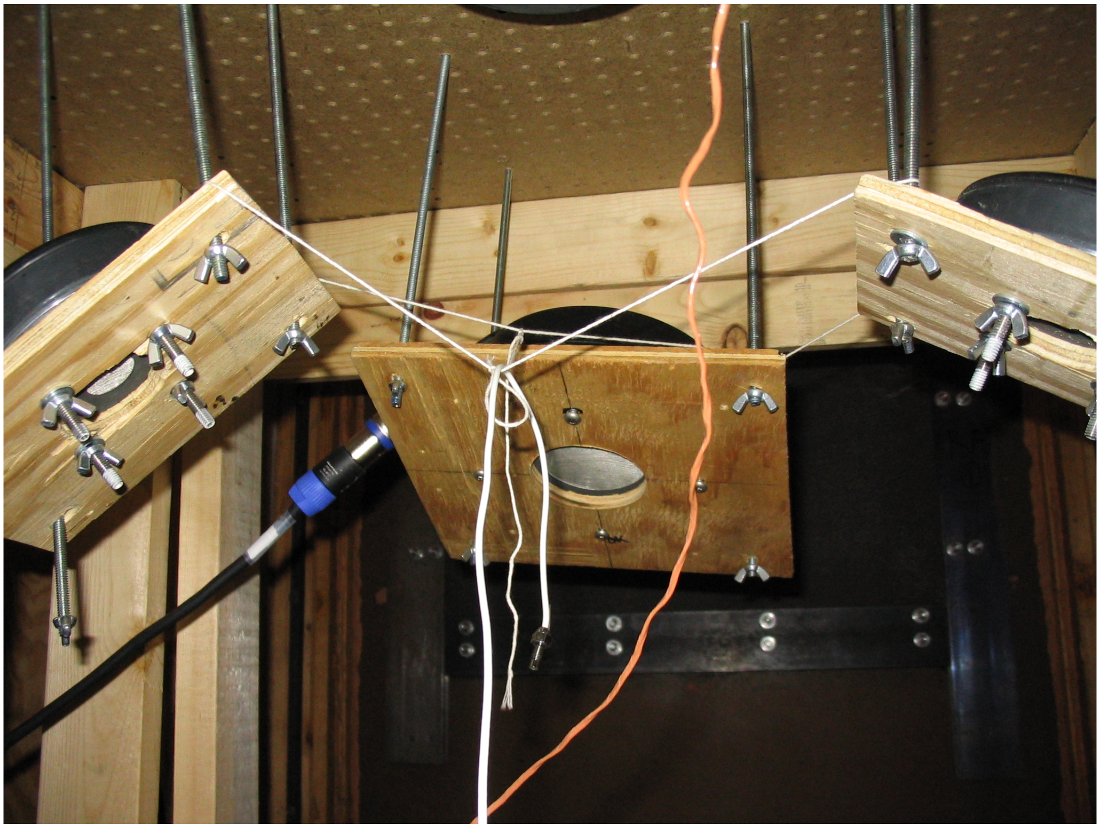

Figure 3.33: Microphone and thermocouple

Figure 3.34: Data collection station

and NViewHMI. Shortcuts for these applications are located on the desktop. Run all four programs.

NView HMI is used to control to spinning speed and direction of the rate table. Once the application has started, click “Manual” or press “F3”. This is shown in Fig. 3.35. Next, enter a distance and velocity and change the jog type to “Distance.” Then, click the small “x” in the top left corner of the window and click either the “+” or “-” sign to spin clockwise or counterclockwise, resp. To stop the spinning, click the “x” once more. A screenshot is presented in Fig. 3.36.

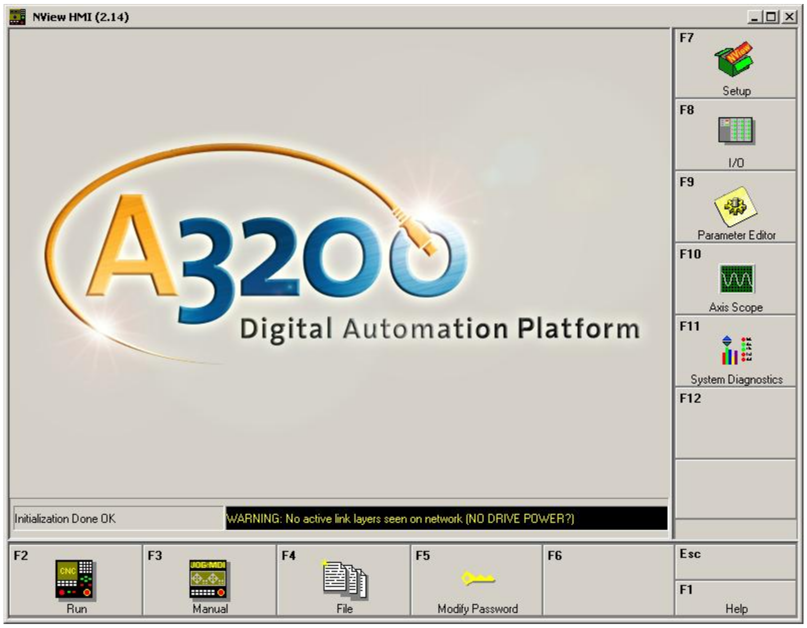

Initialization Done OK

WARNING: No active link layers seen on network (NO DRIVE POWER?)

Figure 3.35: NView HMI for controlling rate table startup screen

NCH Tone Generator is used to generate noise. Set all parameters prior to any testing. These parameters include frequencies, tones, amplitudes, duration, and waveform. Once these parameters are set, click “Play” or press “F9” to generate the sound specified. Fig. 3.37 is an example sound profile.

Gyros.vi is a LabView frontend for collecting data from the (up to) five gyros simultaneously. Simply enter in a file location in the “Path” box and set the test duration (in

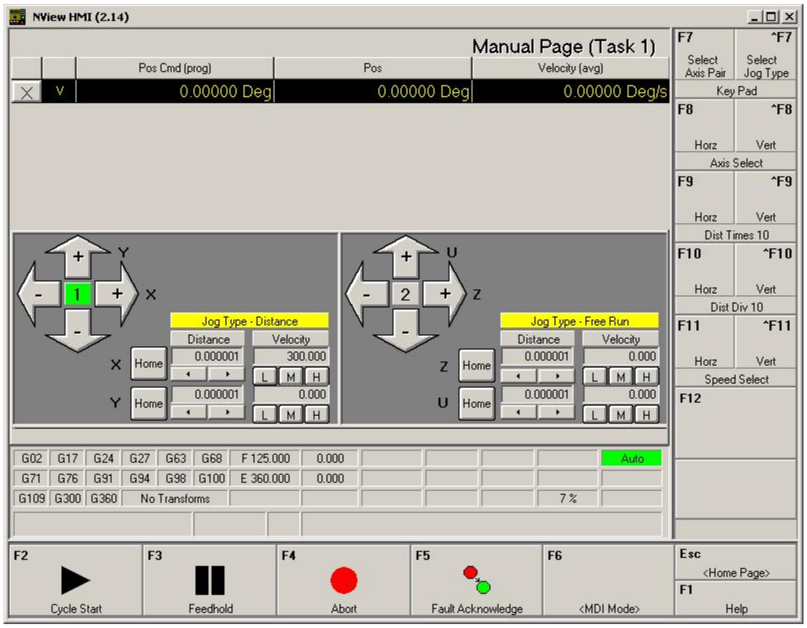

Figure 3.36: NView HMI for controlling rate table

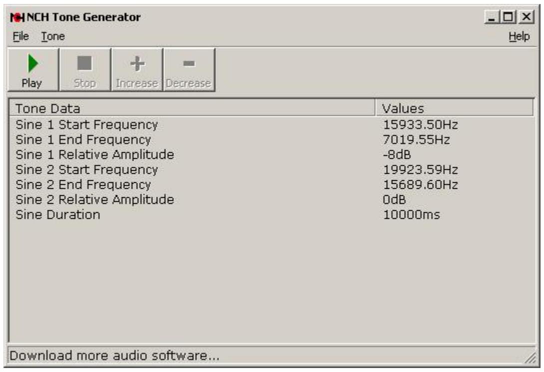

Tone Data	Values
Sine 1 Start Frequency	15933.50Hz
Sine 1 End Frequency	7019.55Hz
Sine 1 Relative Amplitude	-8dB
Sine 2 Start Frequency	19923.59Hz
Sine 2 End Frequency	15689.60Hz
Sine 2 Relative Amplitude	0dB
Sine Duration	10000ms

Figure 3.37: NCH Tone Generator Software

seconds). ST1 and ST2 are used to toggle the self-test inputs of the reference gyro only. All five gyros' outputs will be shown in real-time and saved to the file specified in an Excel readable format. See Appendix D for a block diagram. Run the VI when ready to collect data. Fig. 3.38 shows this interface.

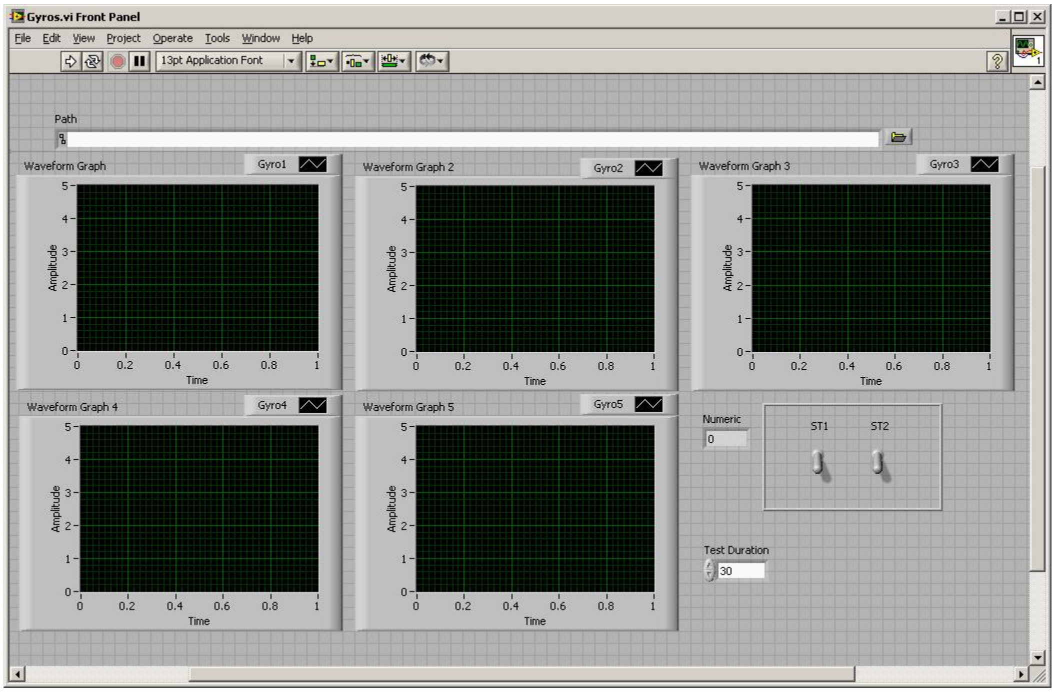

Numeric: 0

Test Duration: 30

Figure 3.38: Gyros.vi data collection screen

The gyro.exe program provides some keyboard hotkeys for test synchronization. For instance, starting and stopping both sound and data collection in discrete intervals. The application also will chart data in Excel automatically. Please see Appendix B for more information.

The other PC is used for sound pressure level measurement via the microphone. PressureTransducerSUM.vi is a LabView application to visually monitor two key elements. The first element is the Current Max Frequency. This displays the single frequency which has acquired the most energy (in Hz). The other element is the Current Max dB value. The number represents the SPL of the aforementioned frequency. This value is expressed in dB. These values are crucial in determining the actual maximum output from the drivers in real-time at a specific frequency. Fig. 3.39 shows a screenshot of the GUI. See Appendix D for the block diagram.

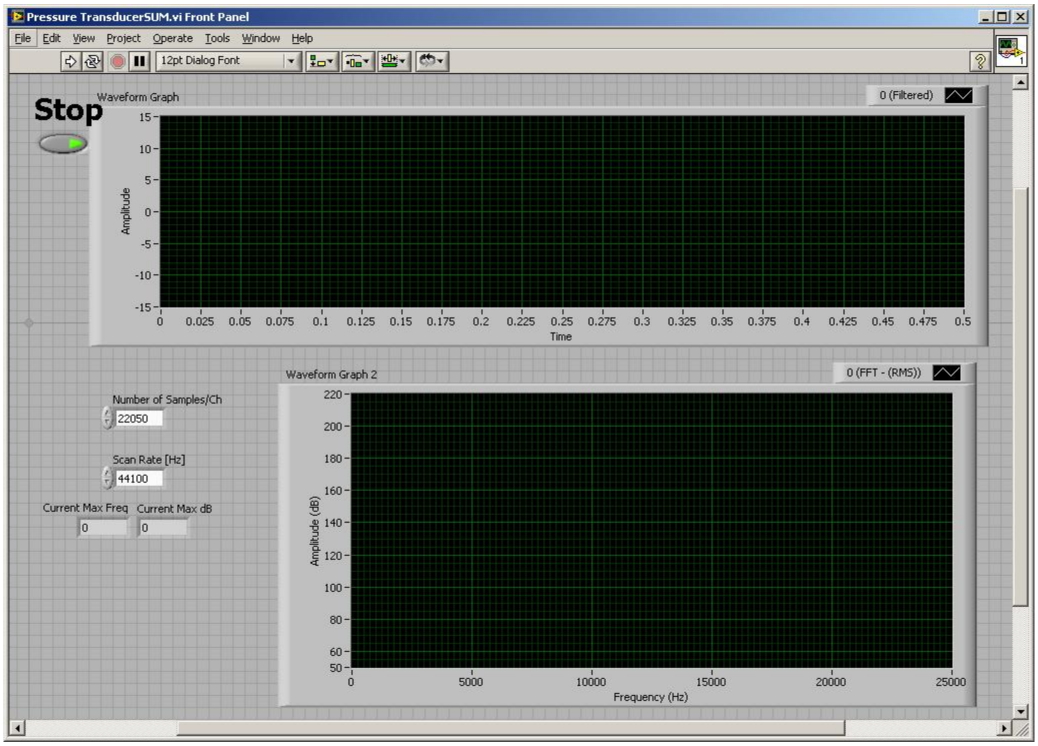

Number of Samples/Ch: 22050

Scan Rate [Hz]: 44100

Current Max Freq: 0

Current Max dB: 0

Figure 3.39: PressureTransducerSUM.vi screen

3.4 Evaluation of the ADXRS300 Gyros

This section is comprised of the pertinent raw data from acoustic tests performed on the ADI ADXRS300 gyros. This data is primarily composed of sound pressure amplitudes across the acoustic frequency spectrum and the corresponding effects on the gyro's rate voltage output.

3.4.1 Minimum and Maximum Sound Pressure Levels

Fig. 3.40 shows the baseline sound pressure levels (SPL), in decibels (dB), versus frequency (Hz) in the absence of sound. Note: the amplitudes for all the following SPL charts are continuously averaged over 10s. In other words, over a period of time, the data in the chart would eventually depict a flat line at a certain amplitude. In this case, the baseline data indicates that the average SPL for the silent acoustic chamber is approximately 68 dB over the acoustic spectrum. This number represents the minimum SPL the Endevco sound pressure transducer is capable of detecting. This is due to its calibration for accurate readings at extremely high SPL's of over 180 dB. For all tests that involve "no sound," Fig. 3.40 is a typical frequency response. This graphed data will be representative of all these cases. Note the spikes in this graph. These spikes are more than likely a result of electronic noise in the test equipment. This noise appears to be present in regular frequency intervals and is more prominent at lower frequencies. These spikes have no bearing on the real world ambient noise present in the tests.

Fig. 3.41 illustrates the maximum sound pressure levels experienced in the presence of white noise. See Appendix A for more information. Here, peaks can be seen as high as 100 dB. This level is equivalent to standing in the front row of a rock concert. White noise is a random distribution of frequencies with equal amplitudes. Therefore, Fig. 3.41 encapsulates the speakers' ability to effectively reproduce mathematically random white noise at a maximum power level. In general, white noise is a good model for a variety of acoustic events. Anything from music concerts to powerful exhaust emissions can be modeled by white noise. Overall, white noise can test the gyros' output in the presence of a large number of random powerful frequencies. Notice how the low frequency spikes from the test electronics is still present. All further white noise tests will use Fig. 3.41 as a reference for typical maximum SPL's of white noise.

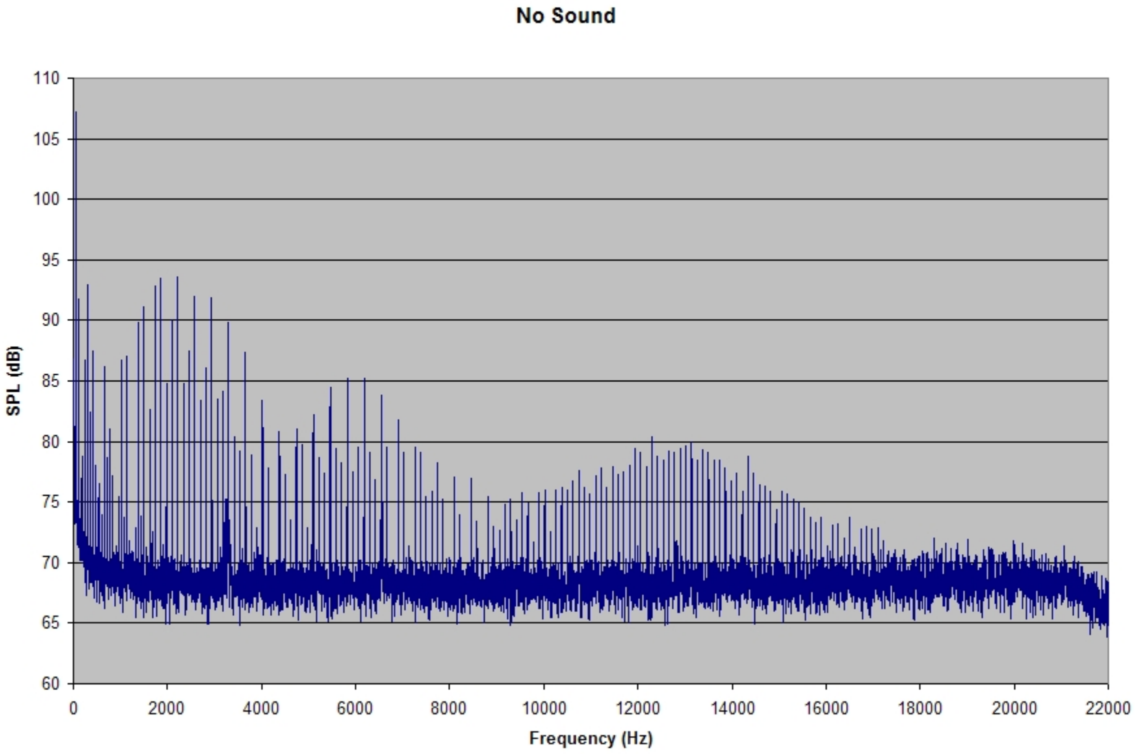

Figure 3.40: 10 Second Average SPL Baseline(No Sound)

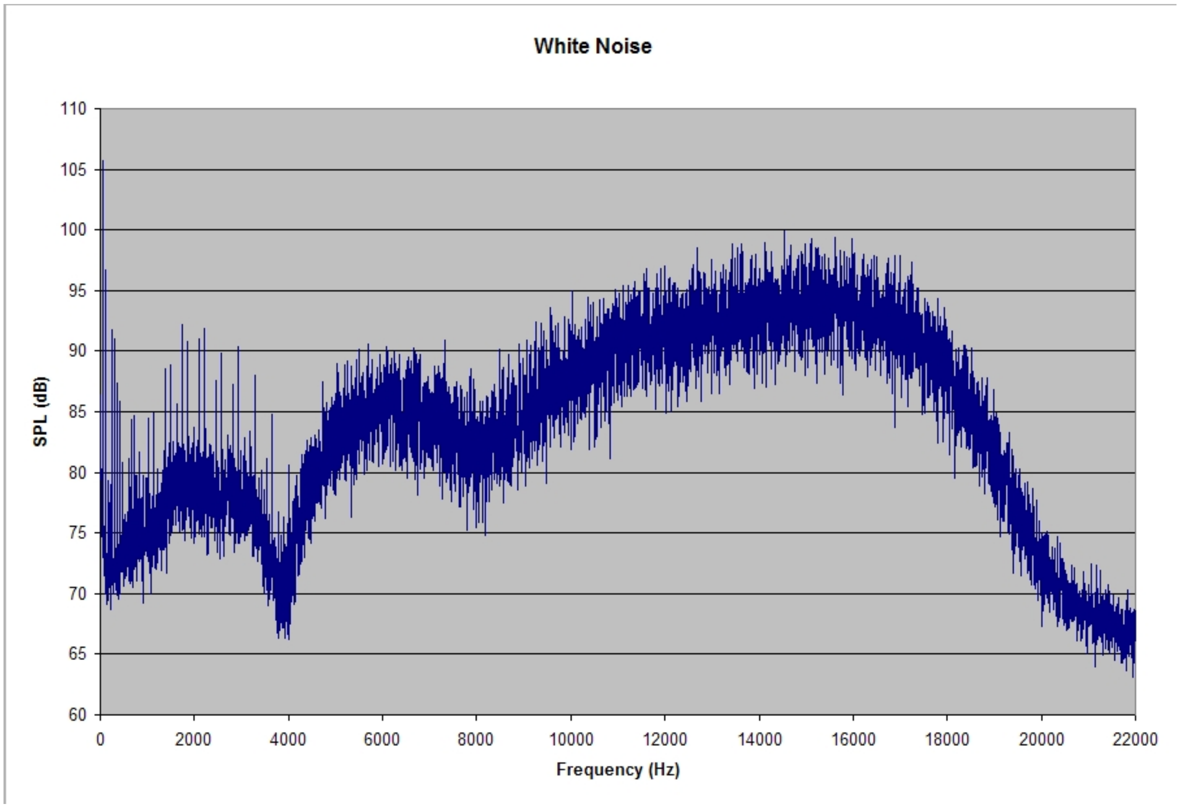

Figure 3.41: White Noise

Fig. 3.42 is an example of the sound pressure level of a single frequency or tone. In this case, the tone is 13,766 Hz and reaches a SPL of nearly 140 dB. 140 dB sound levels are equivalent to a jet engine takeoff and results in immediate hearing damage in humans. This level is well over the threshold of pain, which begins at 125 dB. This sound pressure level is the maximum level that the test equipment can produce. All tone and sine sweep data will use Fig. 3.42 as a model for the maximum SPL of a single frequency tone.

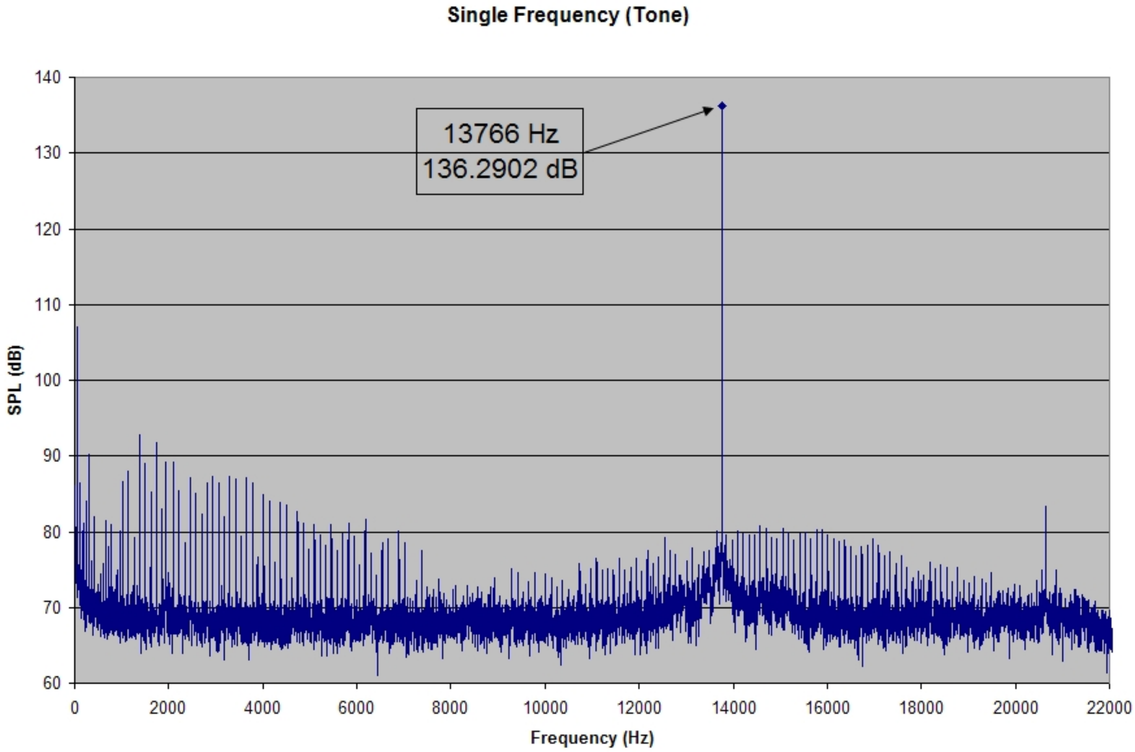

Figure 3.42: Single Frequency (Tone)

3.4.2 Reference Gyro Data

This section will aim to fully characterize the reference gyro as pertains to its acoustic responses. For example, Fig. 3.43 depicts the reference gyro's output rate (V) versus time (s) at various rotational speeds in degrees per second (DPS).

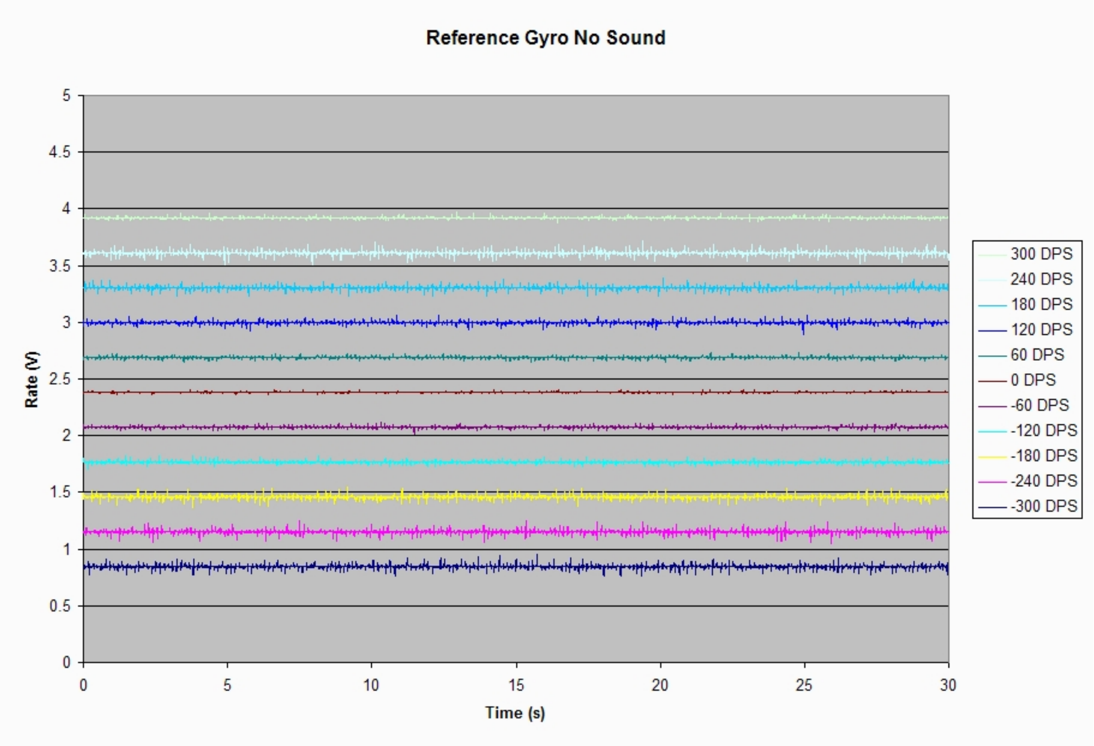

Figure 3.43: Reference gyro's rate output at various angular rates without sound

Fig. 3.44 illustrates the reference gyro's self-test function. Here, the output of ST1 and ST2 are compared to the actual angular rates they are designed to simulate. Clearly, this function does an adequate job.

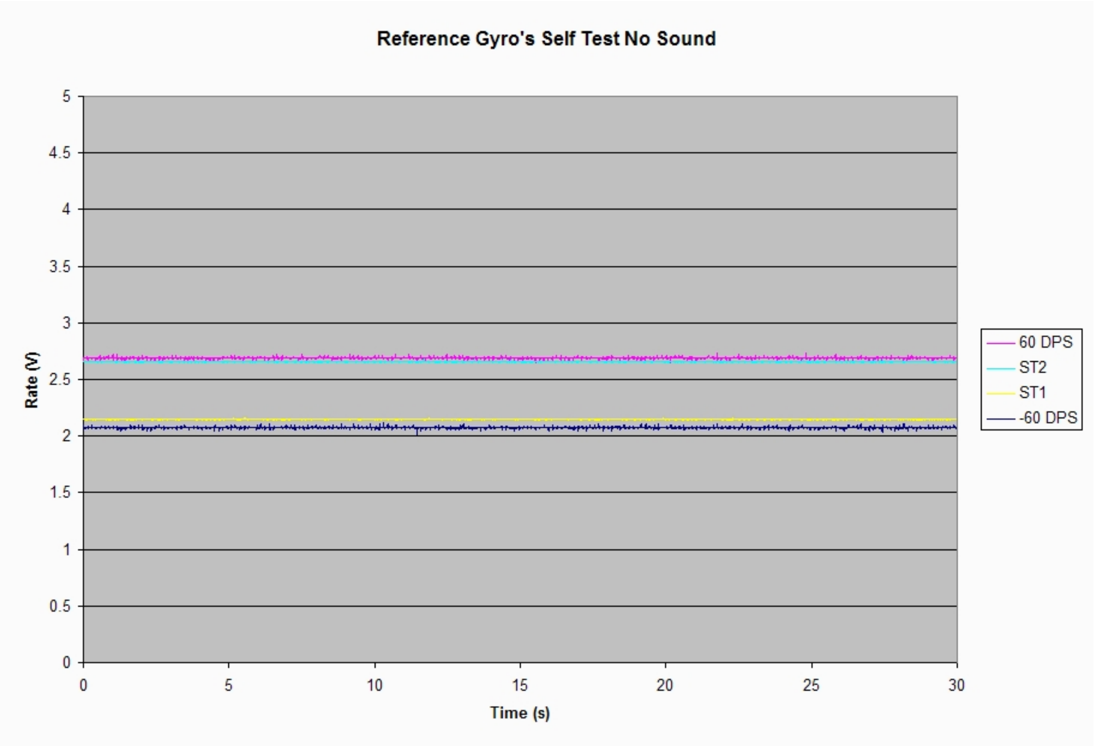

Figure 3.44: Reference gyro's self-test rate out without sound

Fig. 3.47 and 3.48 show how the reference gyro responds to a sine sweep signal from 6000 Hz to 18000 Hz in 30 seconds. It can be seen that a clear disruption occurs at certain frequencies near 14000 Hz which corresponds to the gyro's natural frequency.

After a trial and error period, the reference gyro's resonant frequency can be found. The resonant frequency is reached when the gyro's rate output becomes a steady-state signal as shown in Fig. 3.50. In this case, the resonant frequency occurs at 13903.77 Hz.

In addition, the gyros exhibit a noticeable harmonic frequency at roughly half the resonant frequency. In the reference gyro's case, this first sub-harmonic occurs at 6951.95 Hz as seen in Fig. 3.51.

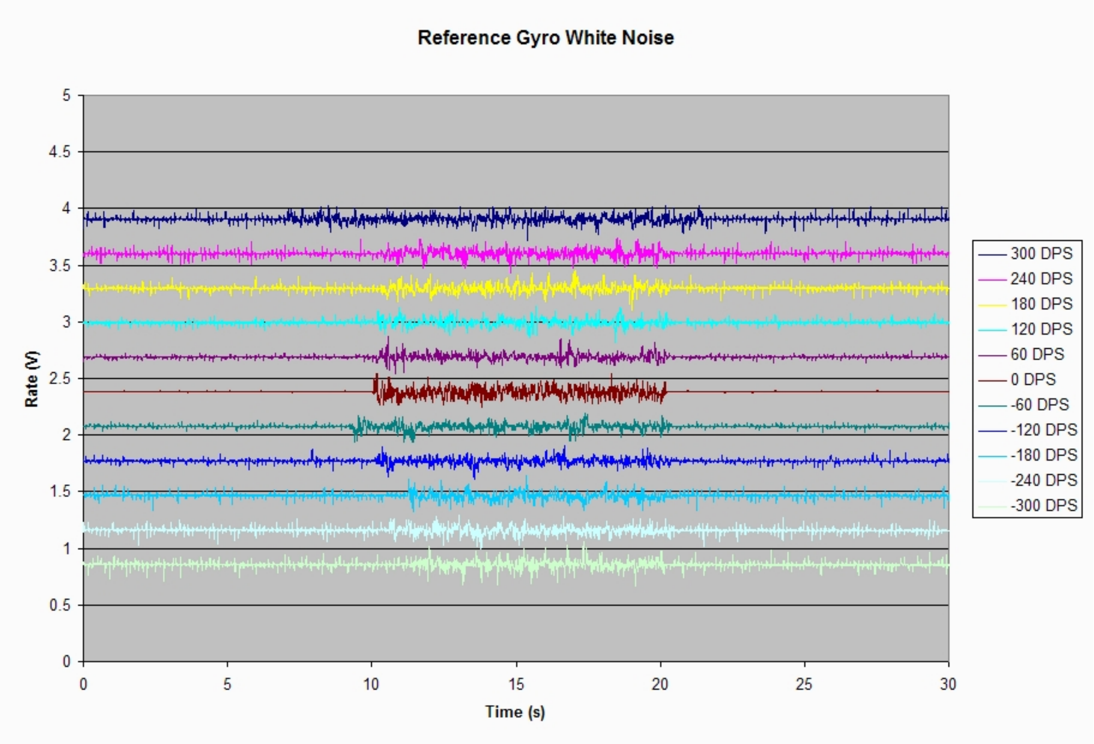

Figure 3.45: Reference gyro with white noise

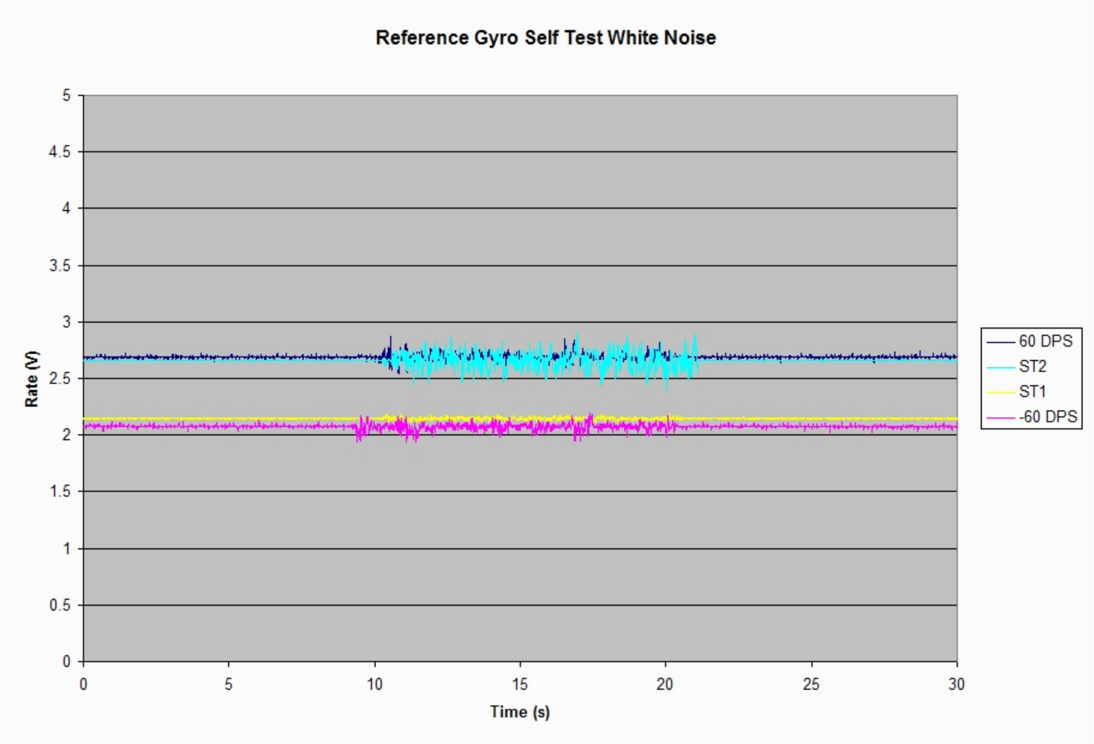

Figure 3.46: Reference gyro's self-test with white noise

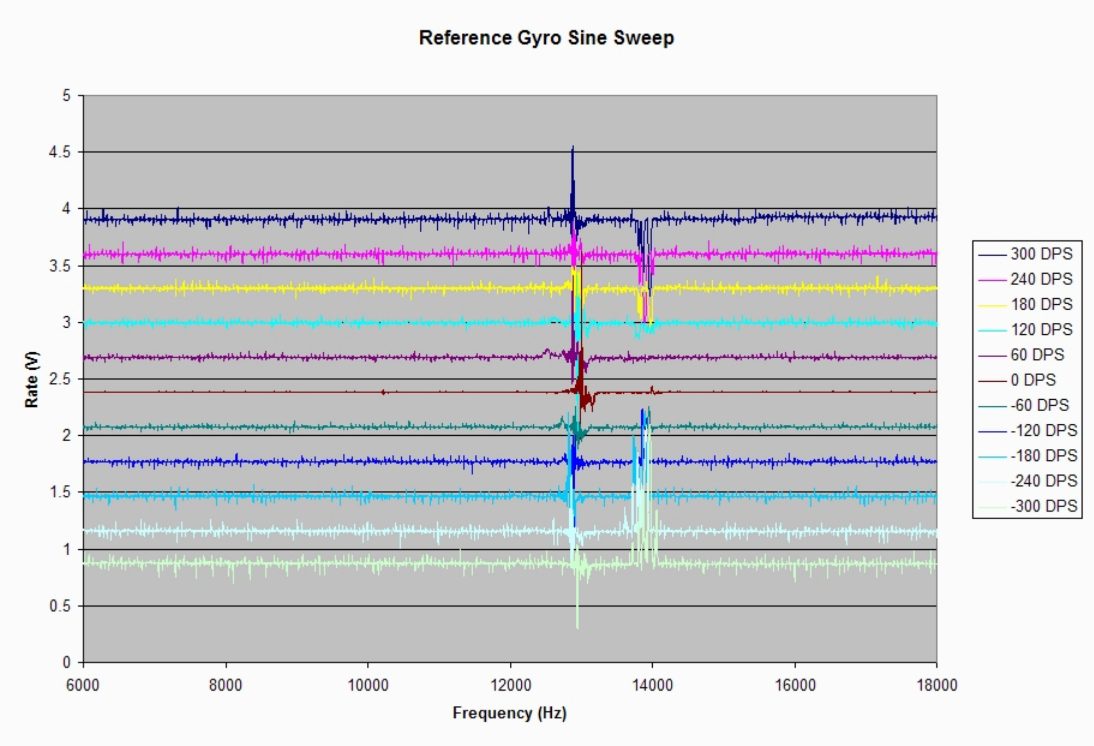

Figure 3.47: Reference gyro sine sweep

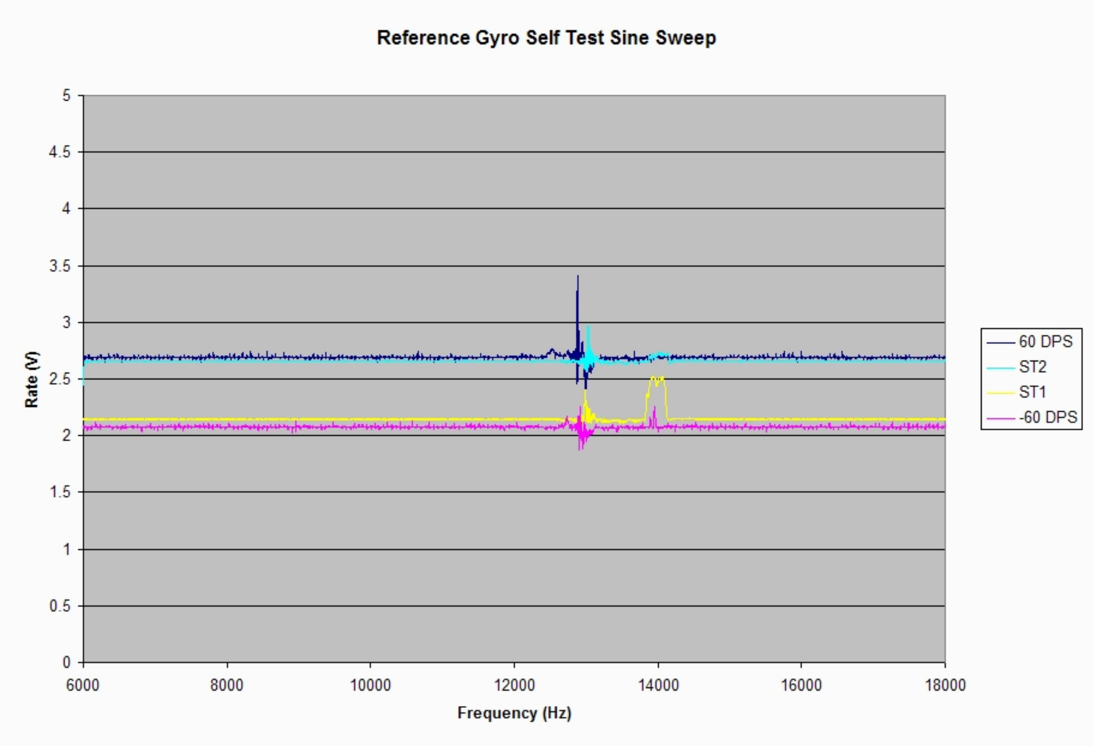

Figure 3.48: Reference gyro’s self-test sine sweep

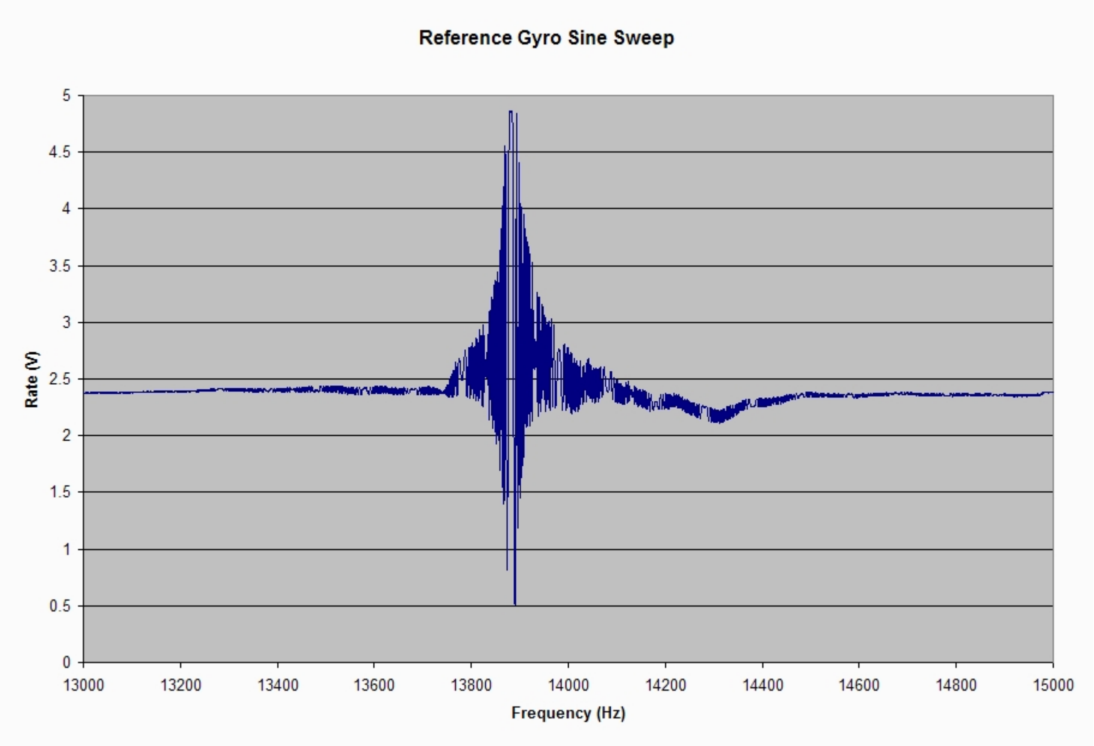

Figure 3.49: Reference gyro sine sweep near resonant frequency (0 DPS)

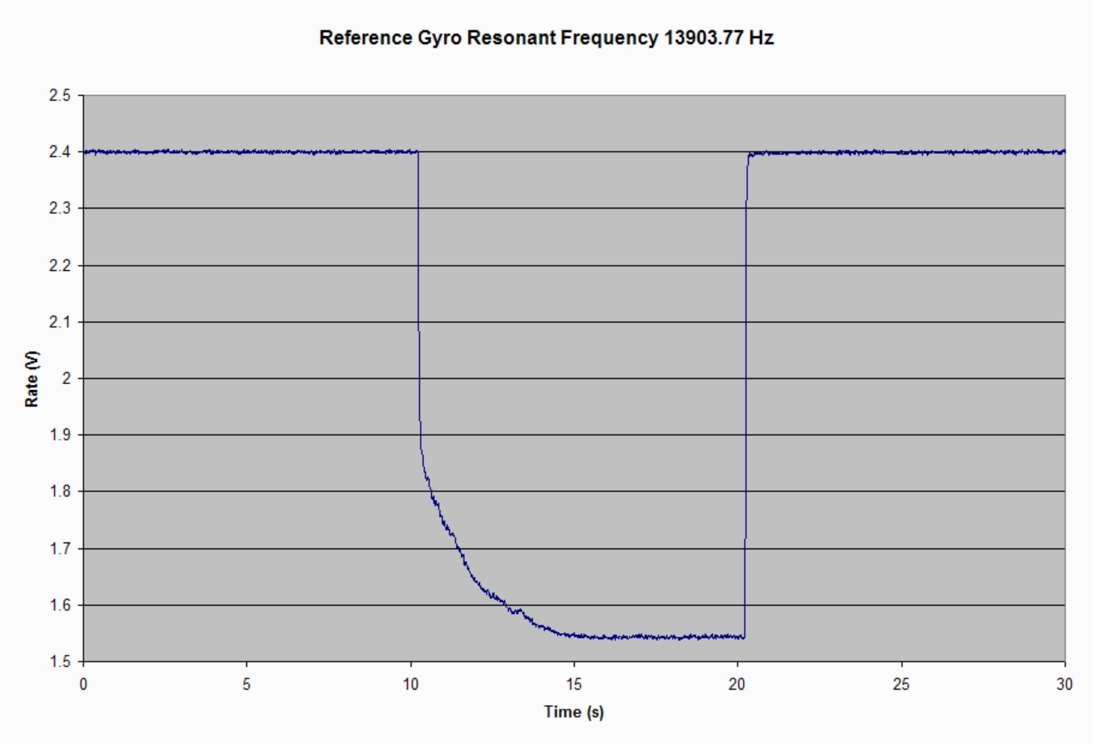

Figure 3.50: Reference gyro’s resonant frequency (0 DPS)

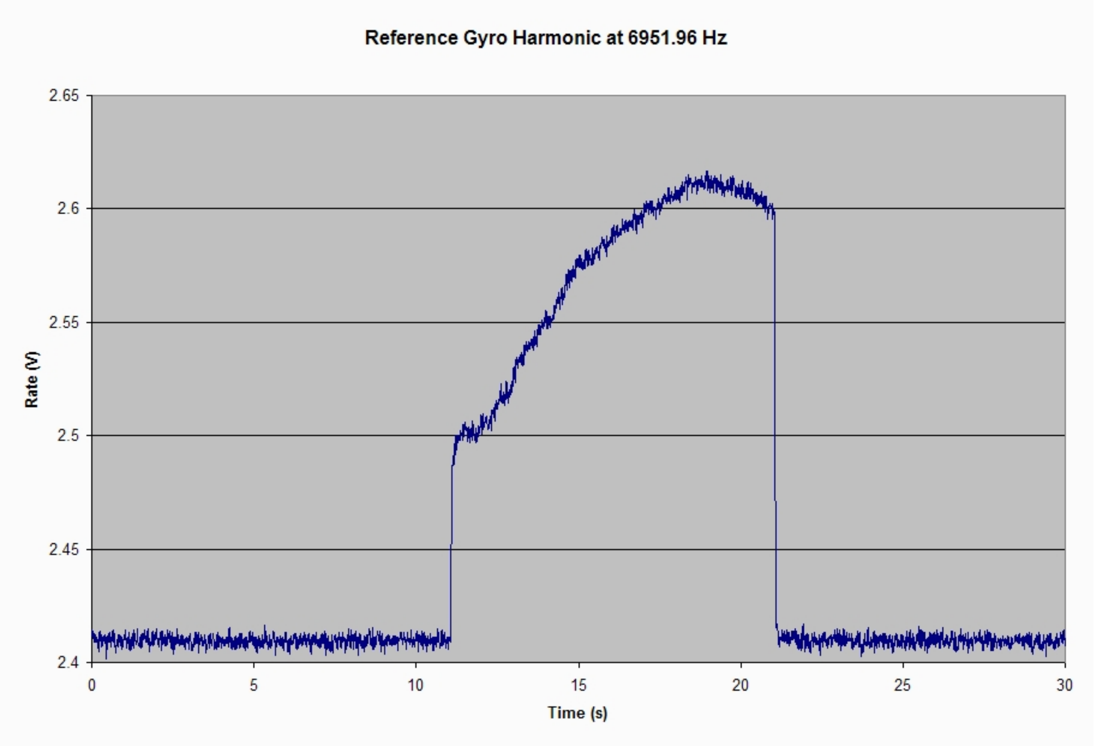

Figure 3.51: Reference gyro's 1st harmonic at 6951.95 Hz (0 DPS)

Fig. 3.52 shows the reference gyro's output response to a linear increase in sound pressure levels over 100 seconds.

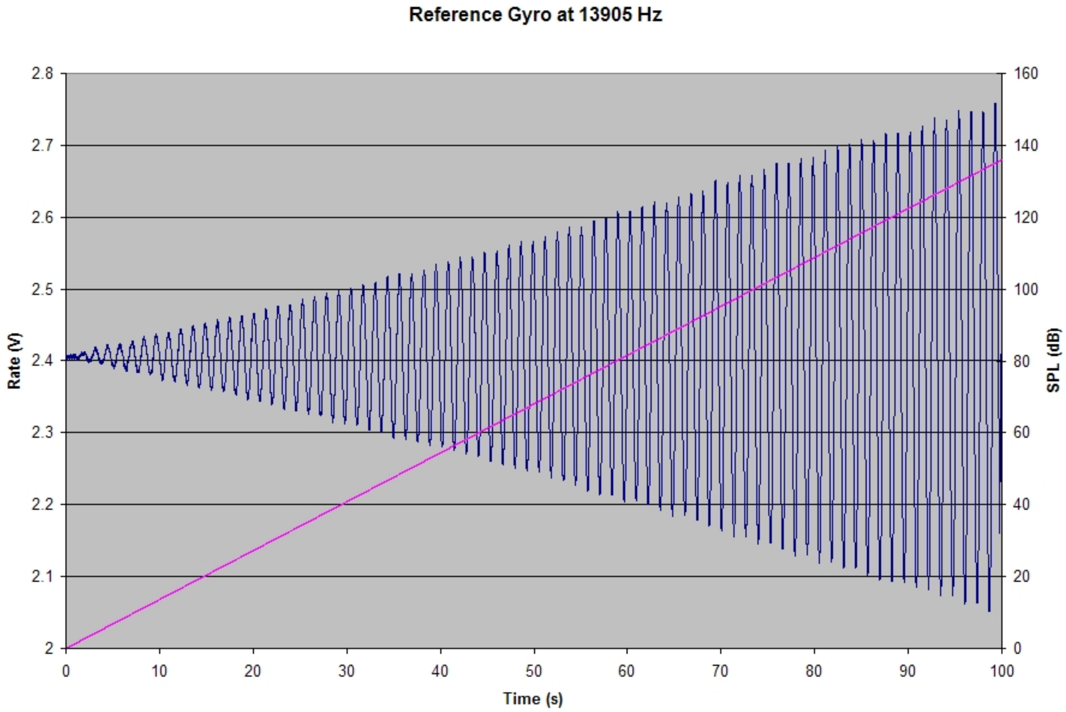

Figure 3.52: Reference gyro output at various sound pressure levels (0 DPS)

Fig. 3.53 to Fig. 3.61 represent a two tone test. Two tones equidistant from the resonant frequency are generated and the gyro's output response is plotted.

3.4.3 Baseline (No Sound and 0 DPS)

Fig. 3.62 provides a baseline look at the gyros. Baseline indicates that there is no rotation and no noise. These readings provide a default output voltage bias for each gyro relative to each other.

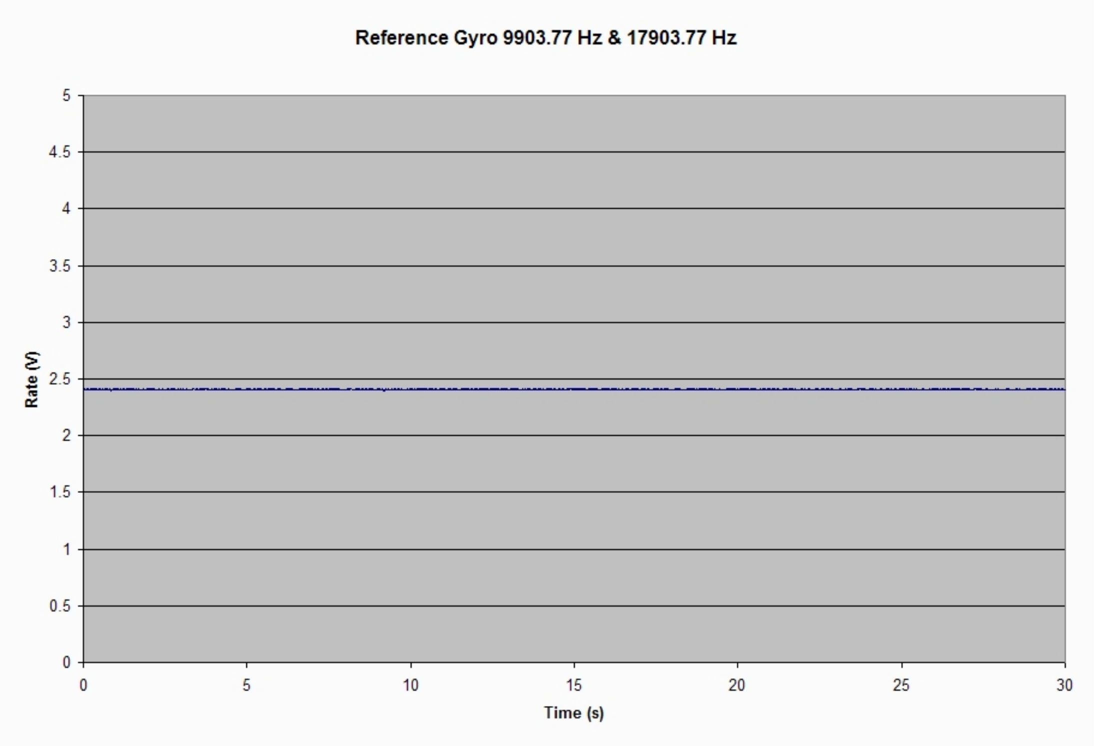

Figure 3.53: Reference gyro two tone test (+/- 4 kHz)

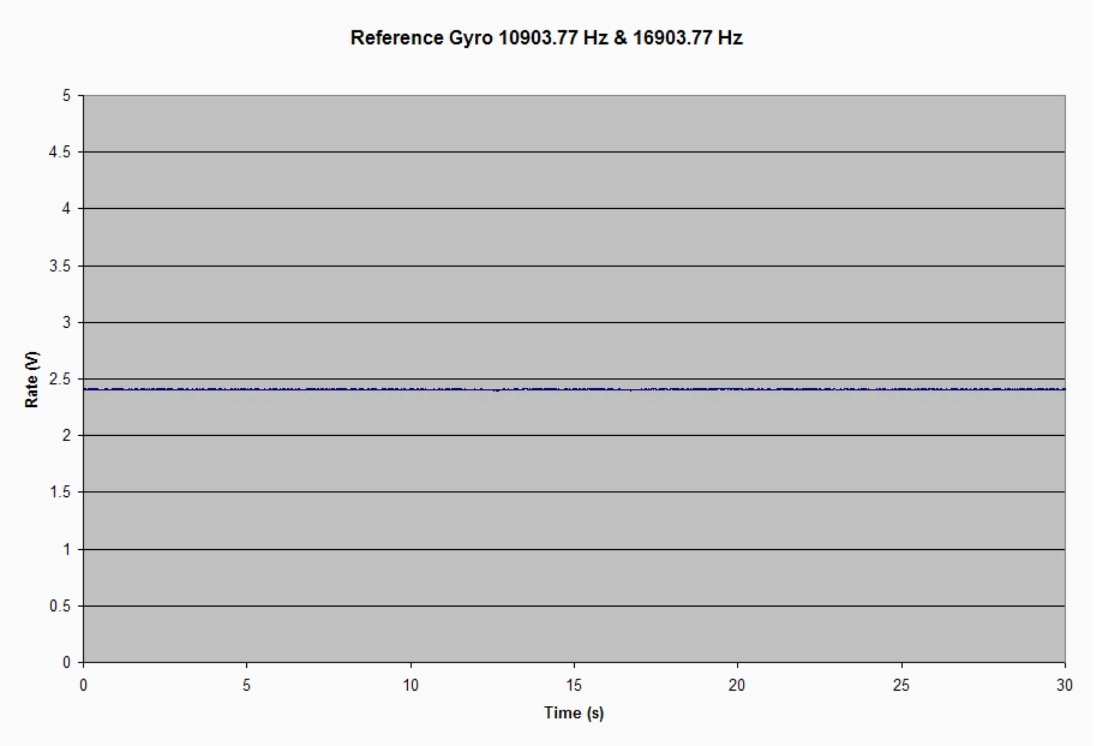

Figure 3.54: Reference gyro two tone test (+/- 3 kHz)

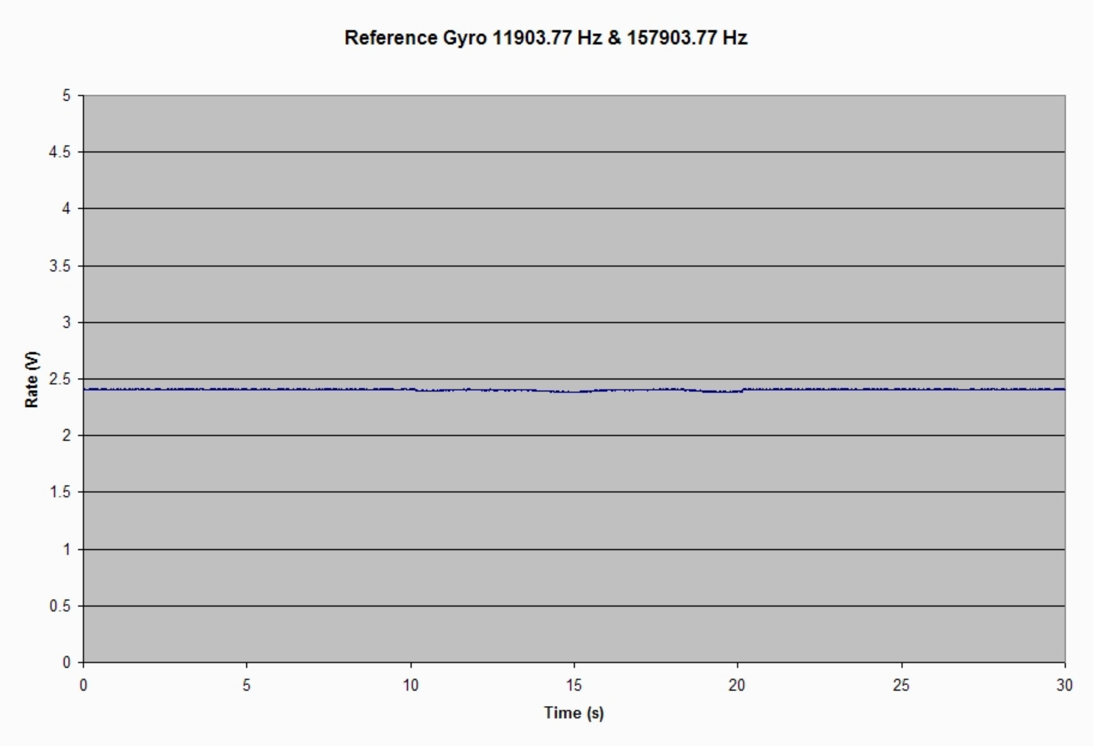

Figure 3.55: Reference gyro two tone test (+/- 2 kHz)

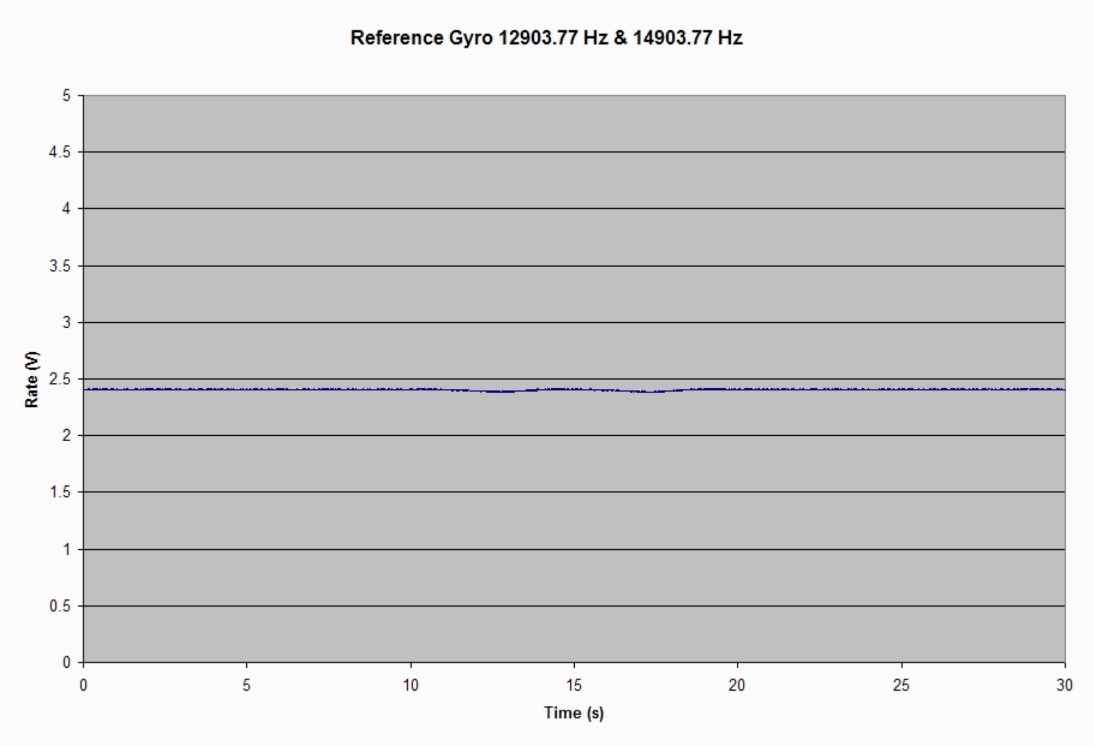

Figure 3.56: Reference gyro two tone test (+/- 1 kHz)

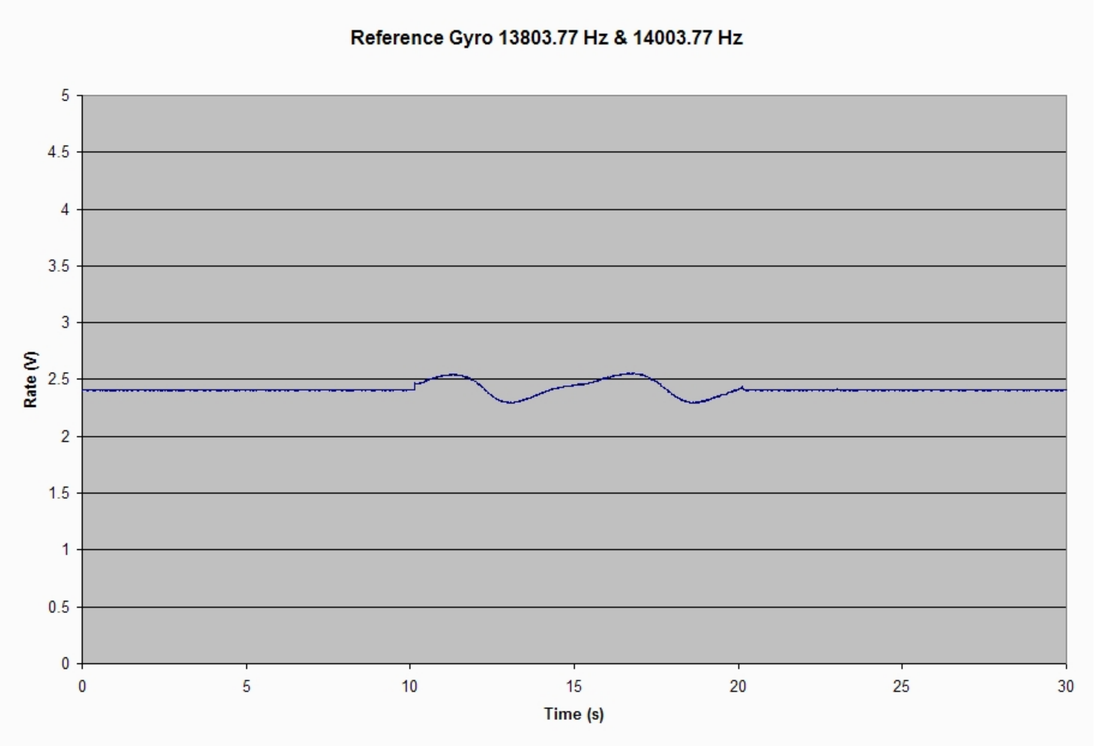

Figure 3.57: Reference gyro two tone test (+/- 100 Hz)

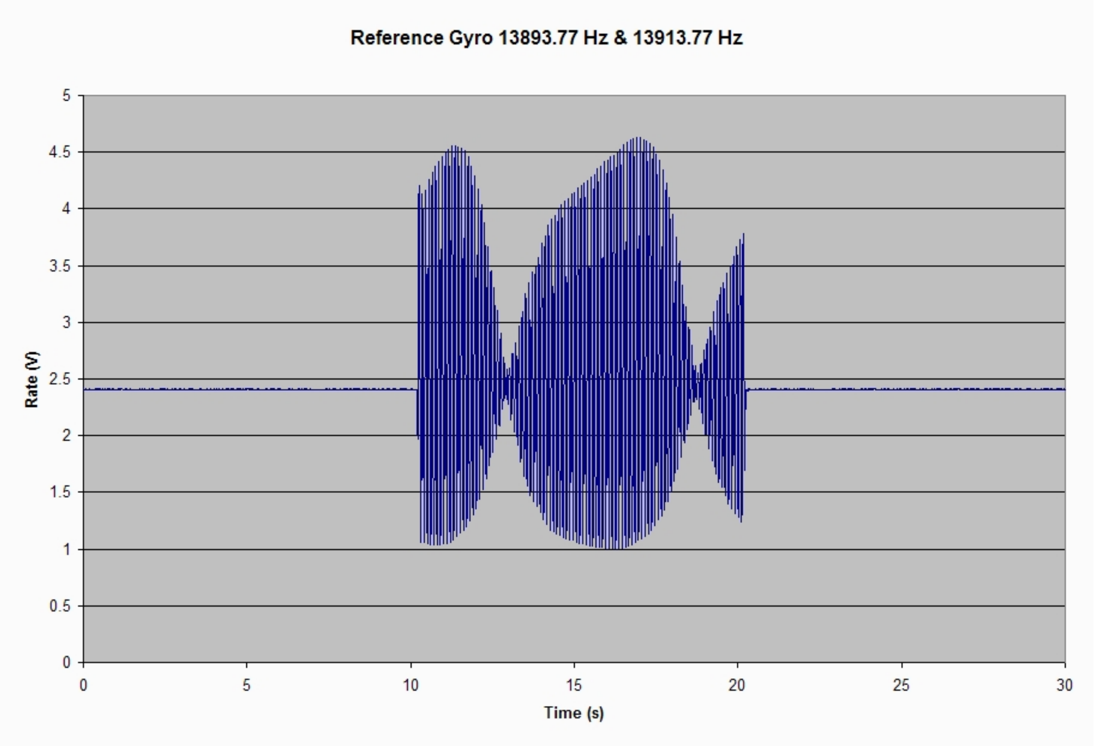

Figure 3.58: Reference gyro two tone test (+/- 10 Hz)

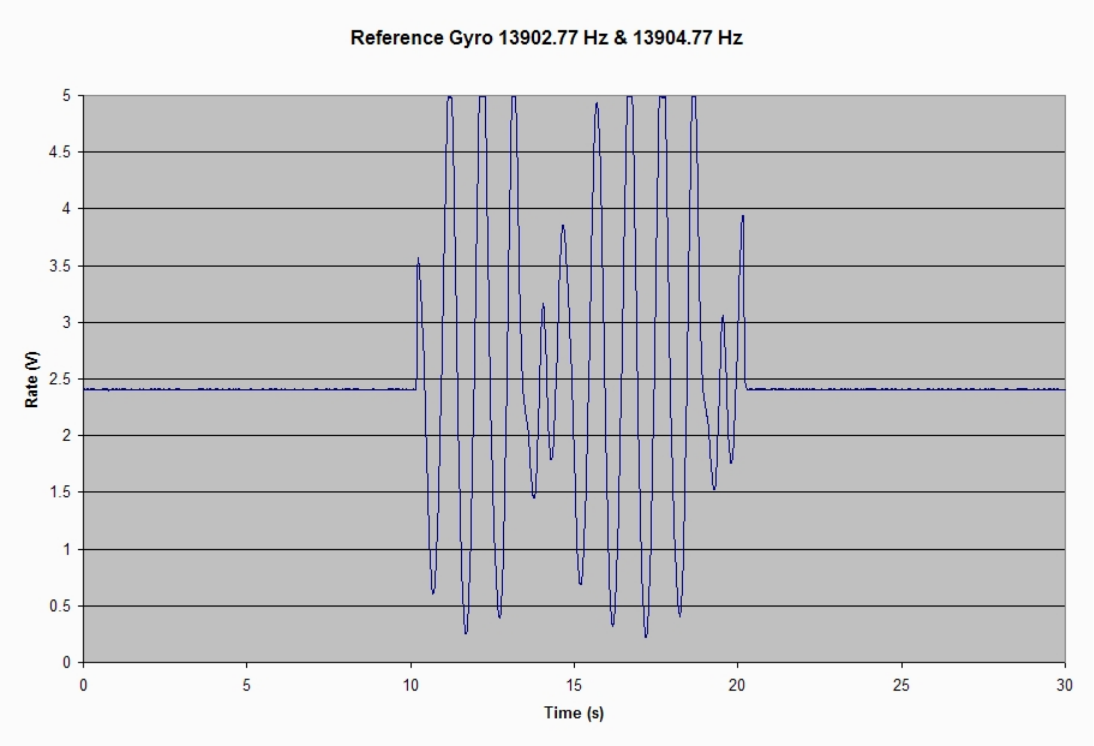

Figure 3.59: Reference gyro two tone test (+/- 1 Hz)

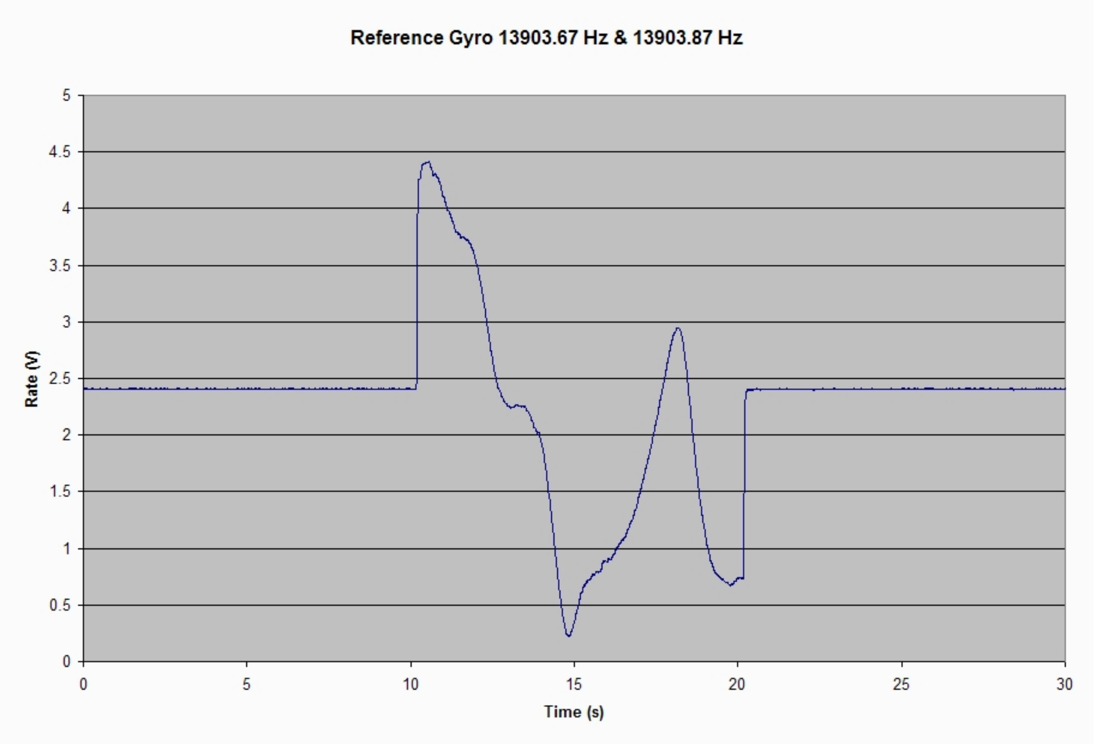

Figure 3.60: Reference gyro two tone test (+/- 0.1 Hz)

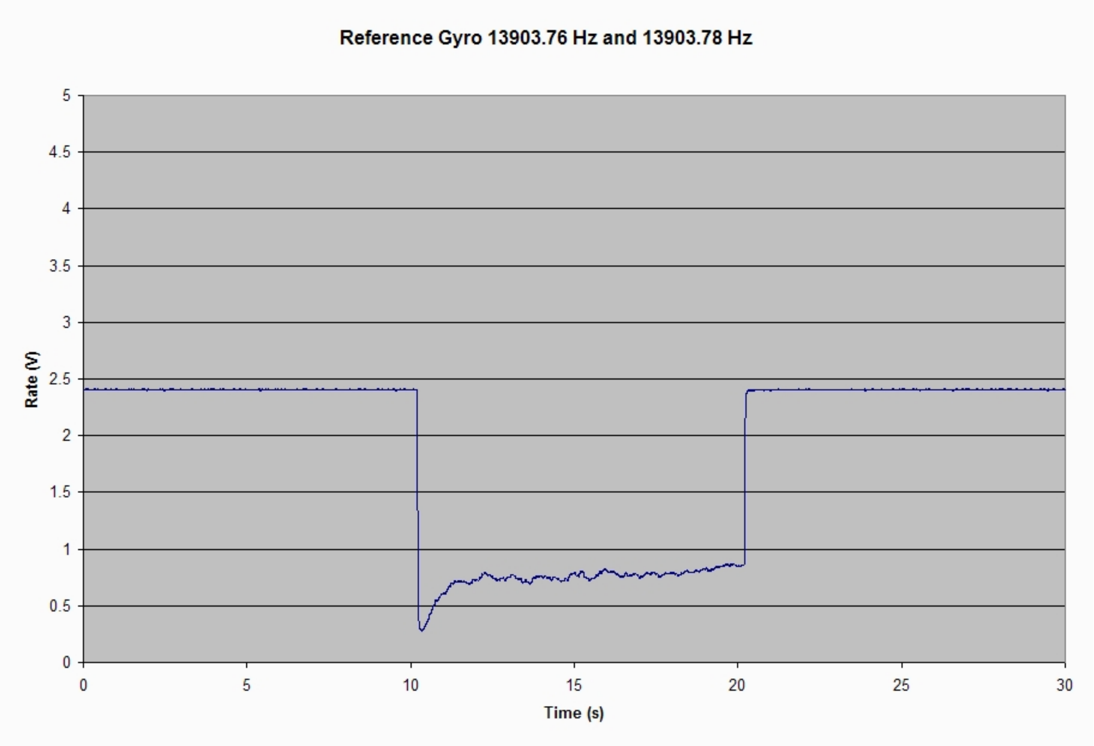

Figure 3.61: Reference gyro two tone test (+/- 0.01 Hz)

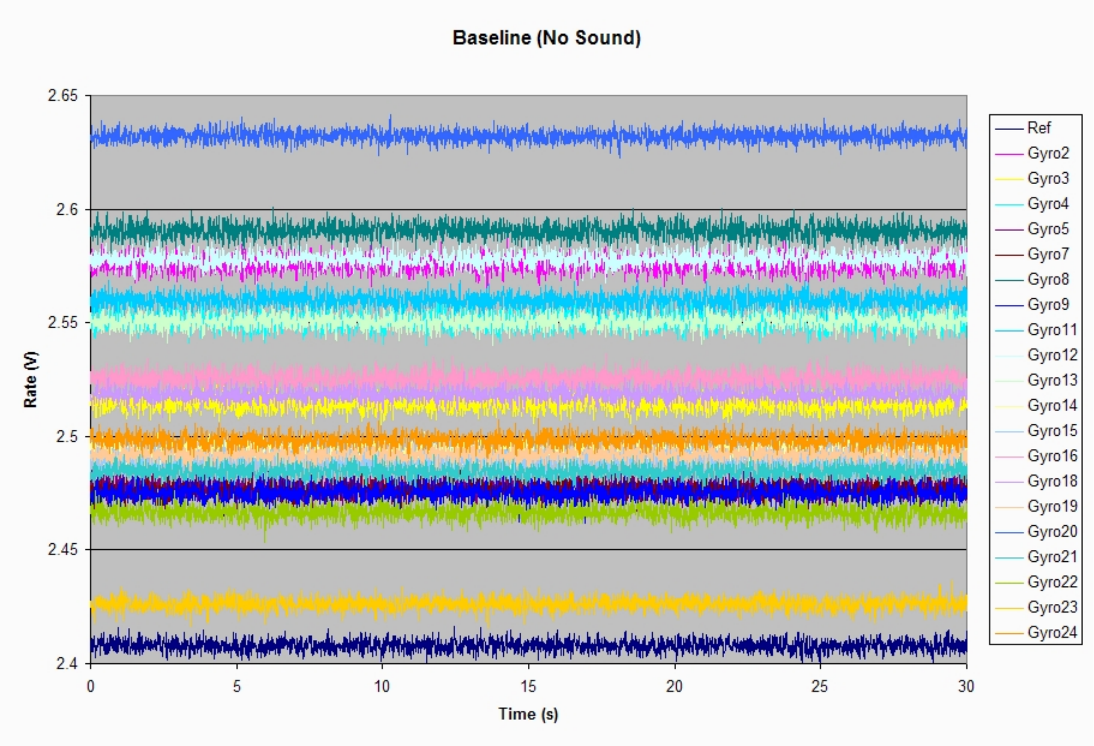

Figure 3.62: Baseline (No Sound and 0 DPS)

3.4.4 White Noise

Here, each gyro is subjected to full power white noise at various angular rates from -300 DPS to +300 DPS. The resulting rate output voltage is shown in Fig. 3.63 to Fig. 3.73.

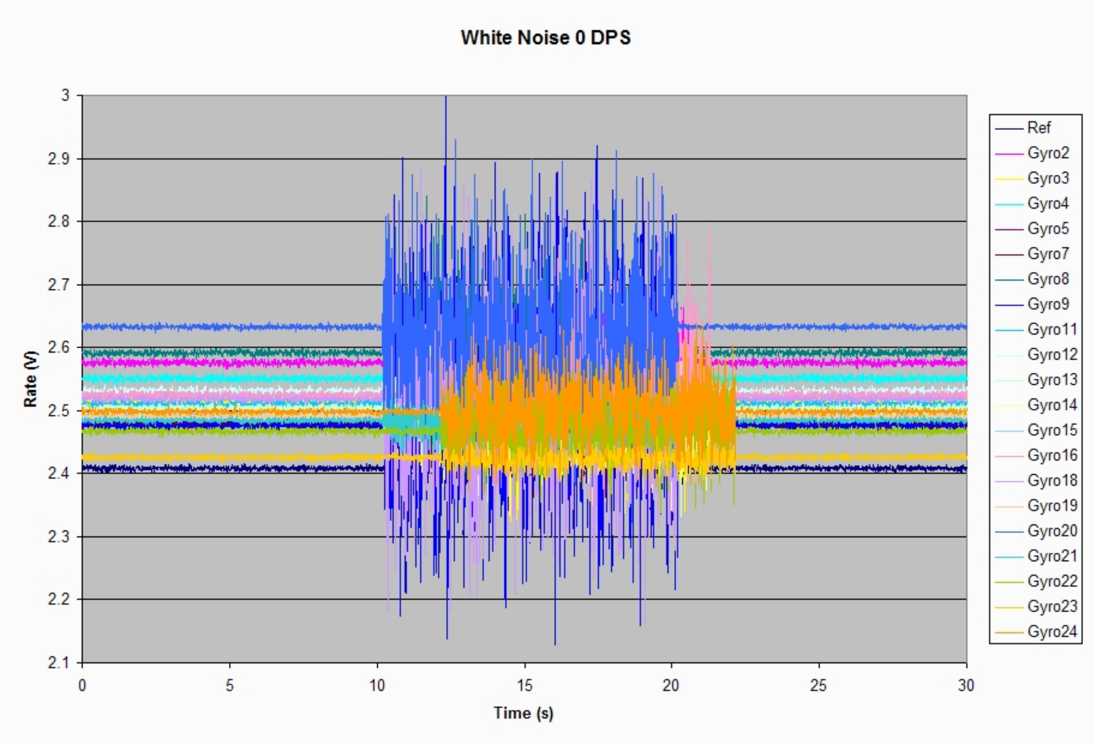

Figure 3.63: White Noise at 0 DPS

3.4.5 Resonant Frequencies

Fig. 3.74 shows each gyro's response to a sine wave whose frequency matches that of its resonant frequency.

3.4.6 First Sub-Harmonics

In this section, Fig. 3.75 will show each gyro's output response to a sine wave whose frequency matches that of its first sub-harmonic frequency. The first sub-harmonic frequency is mathematically half the resonant frequency.

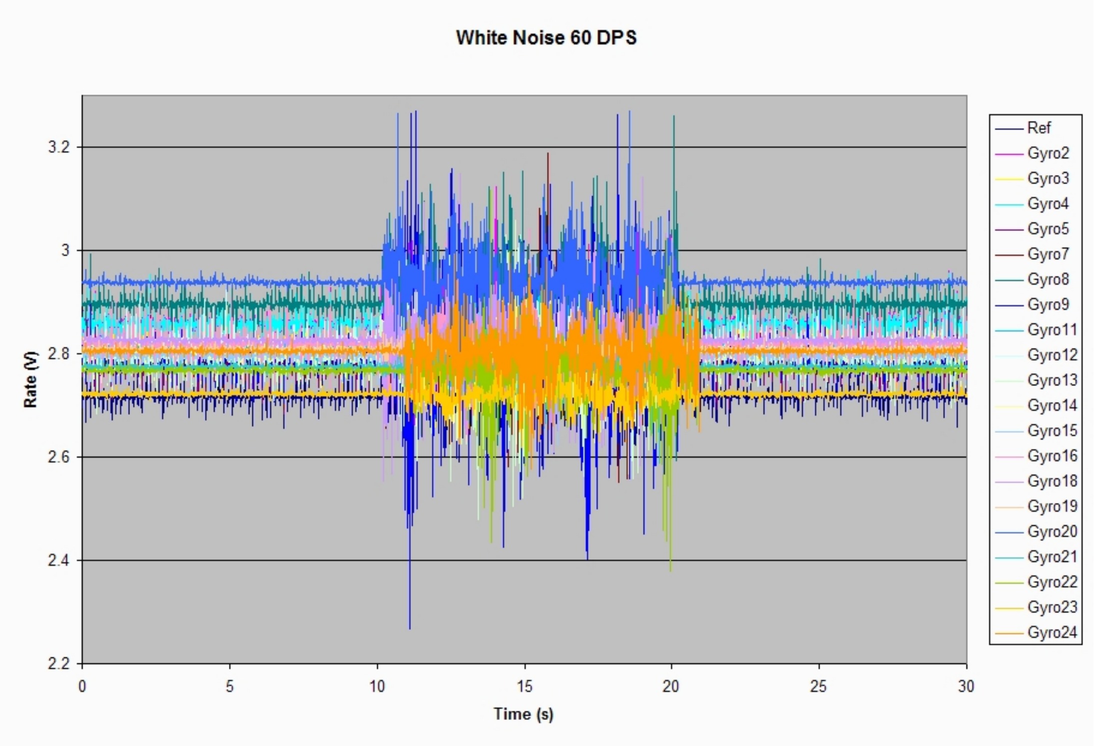

Figure 3.64: White Noise at 60 DPS

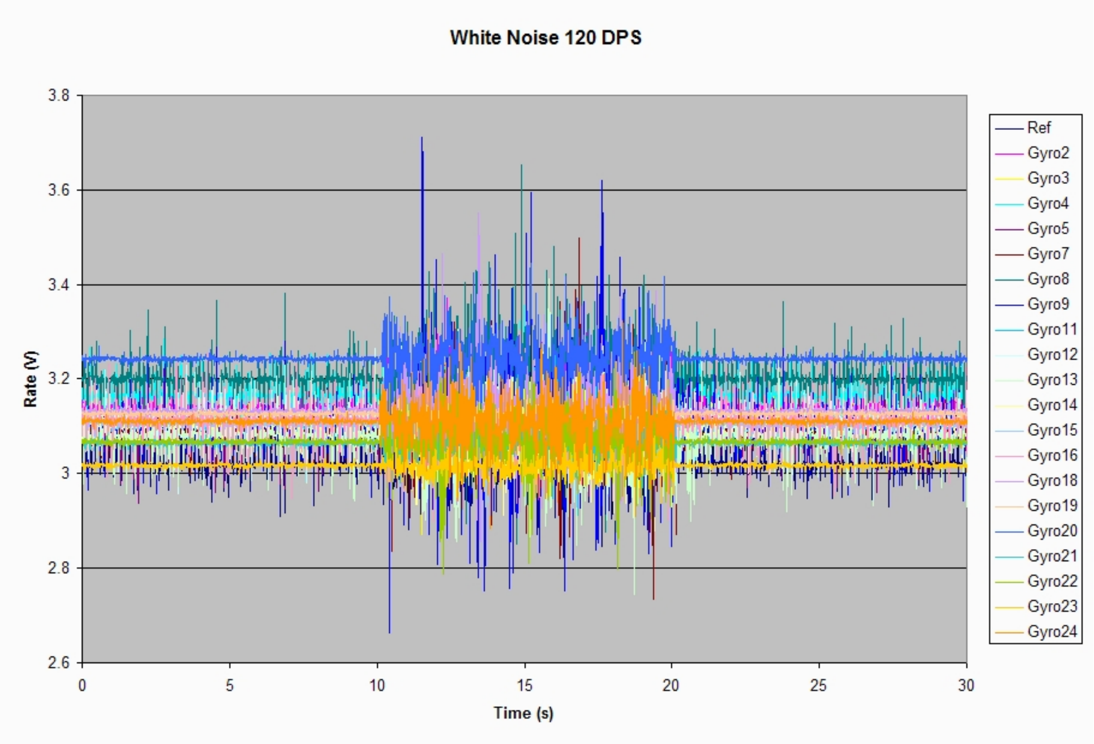

Figure 3.65: White Noise at 120 DPS

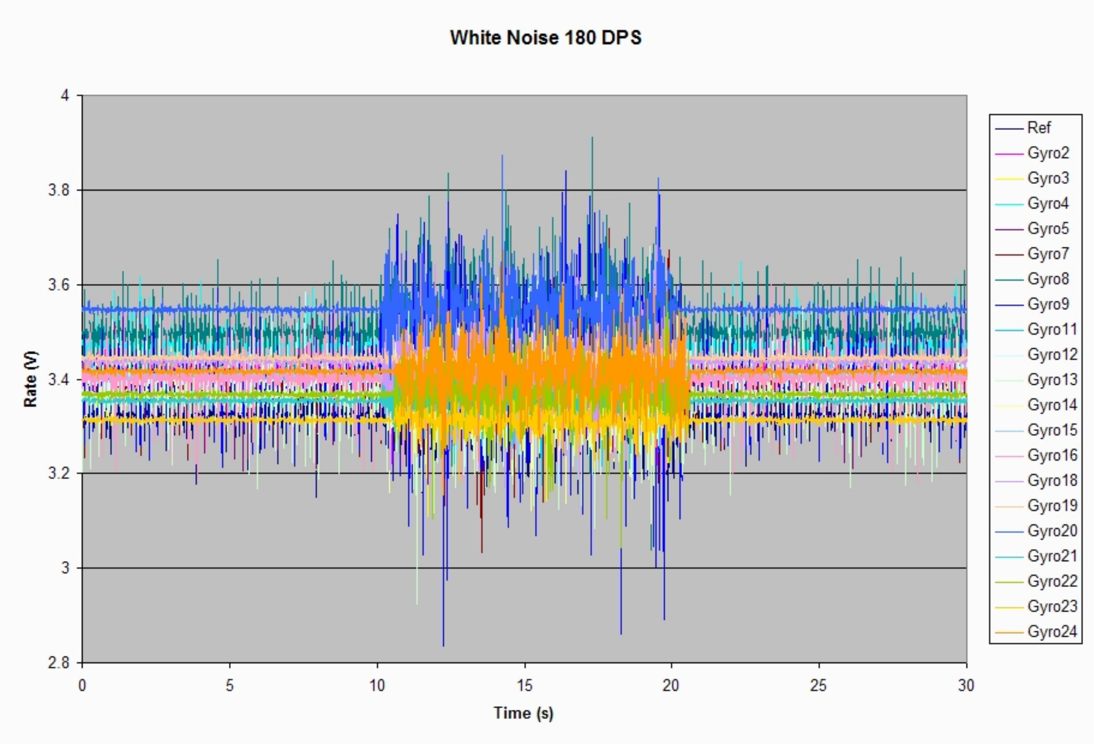

Figure 3.66: White Noise at 180 DPS

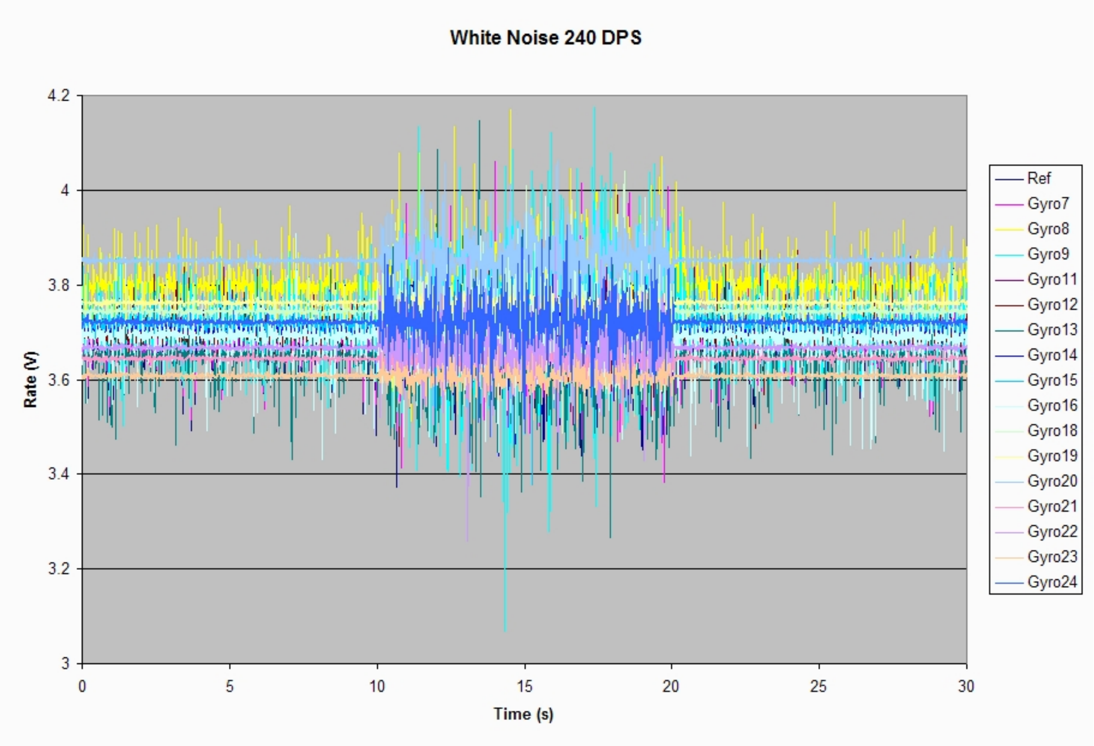

Figure 3.67: White Noise at 240 DPS

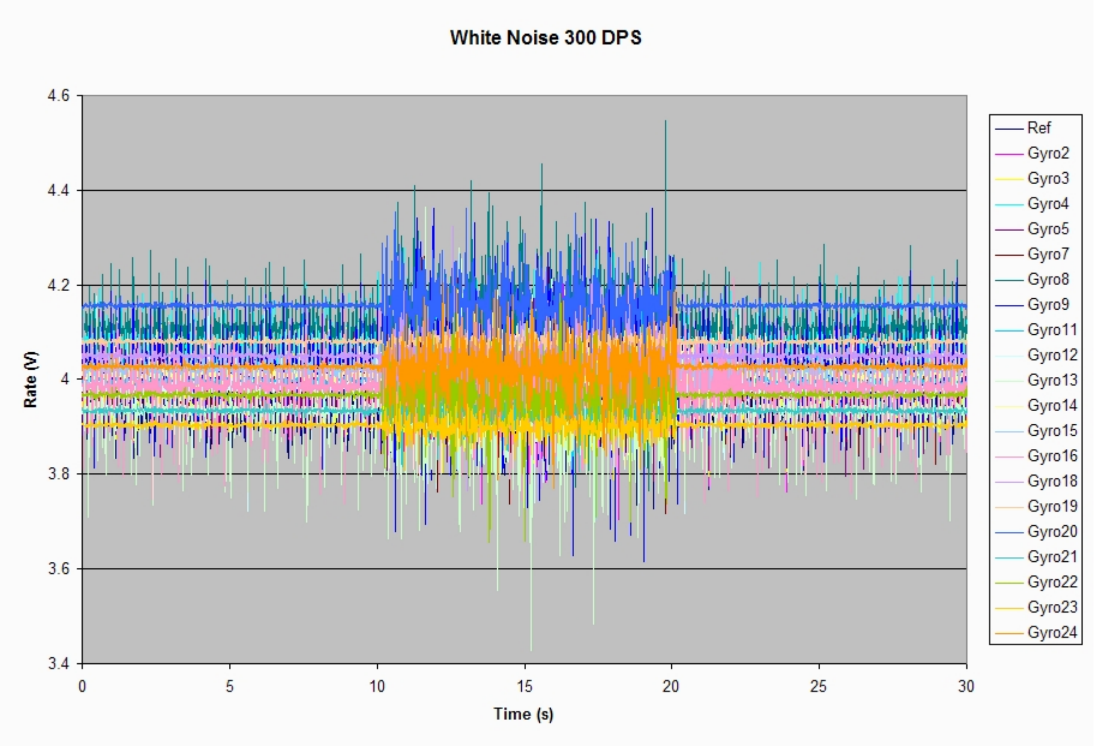

Figure 3.68: White Noise at 300 DPS

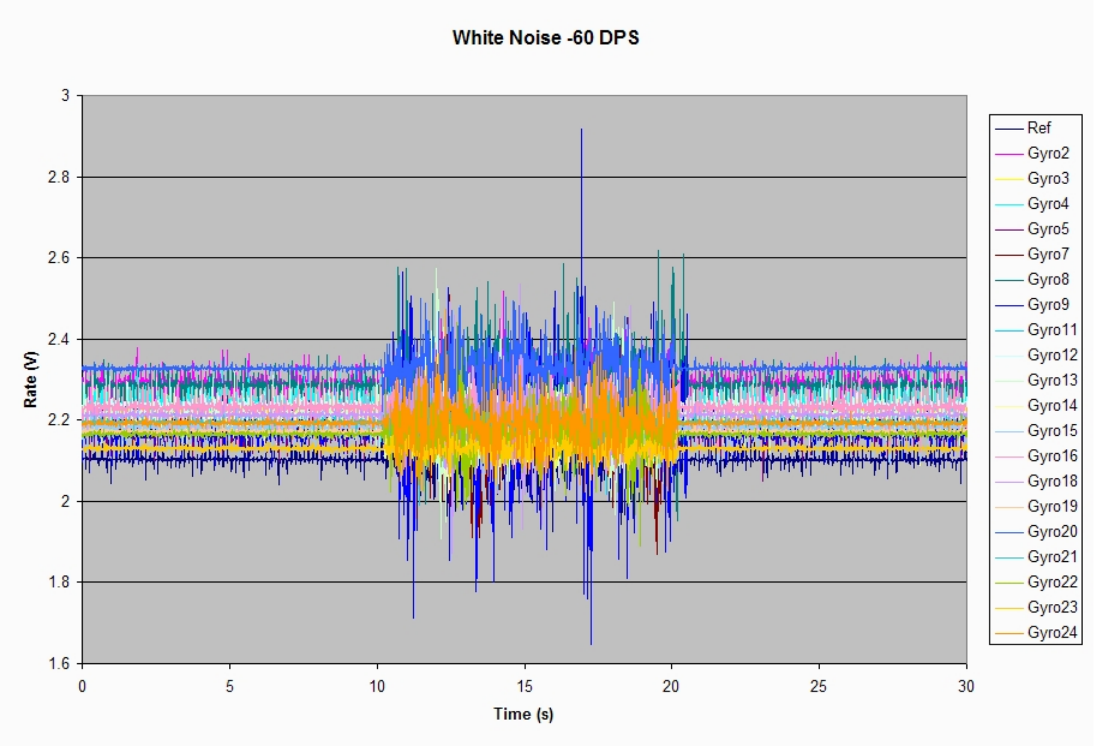

Figure 3.69: White Noise at -60 DPS

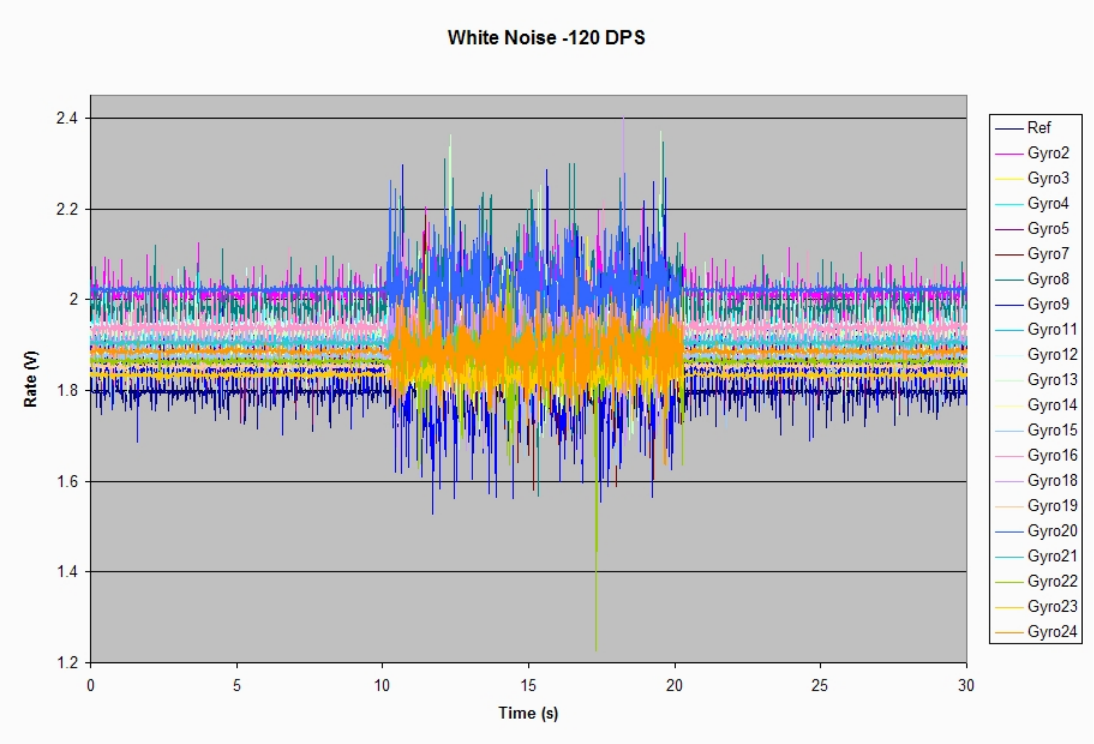

Figure 3.70: White Noise at -120 DPS

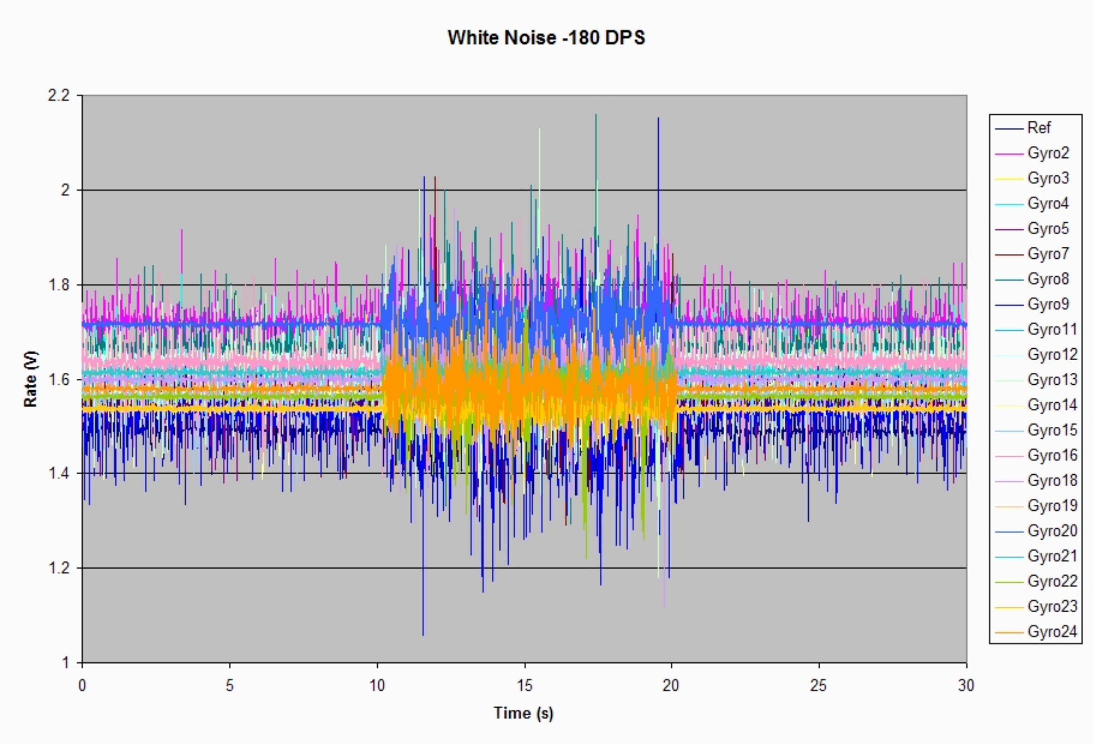

Figure 3.71: White Noise at -180 DPS

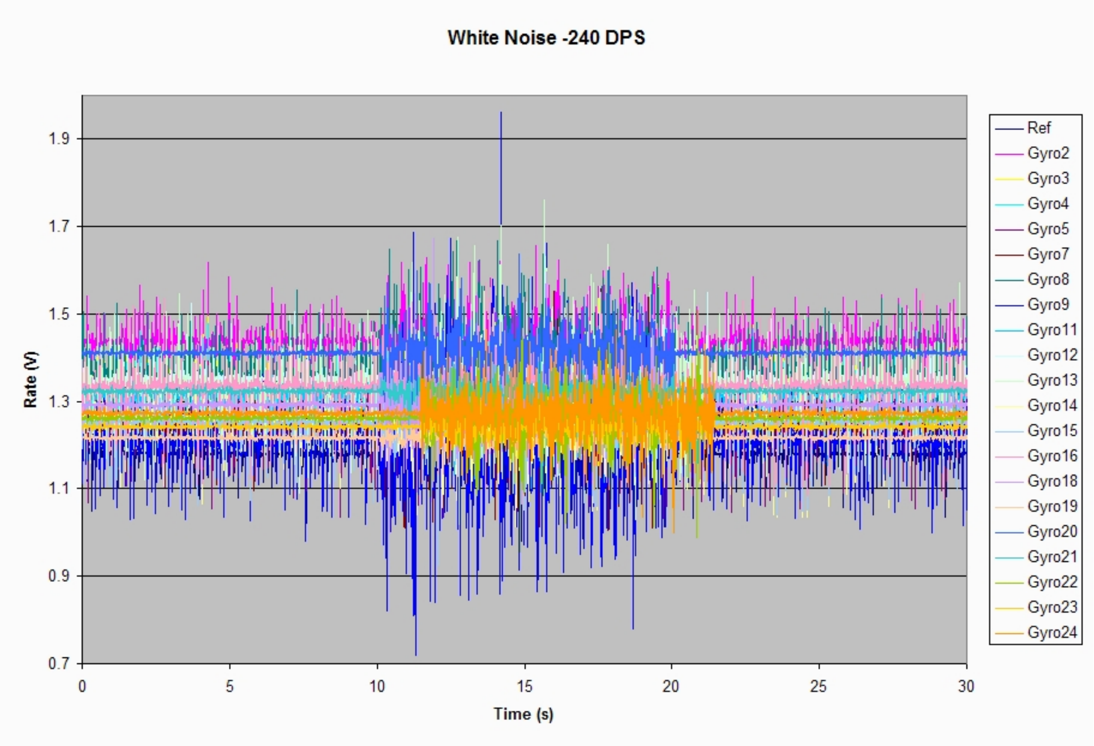

Figure 3.72: White Noise at -240 DPS

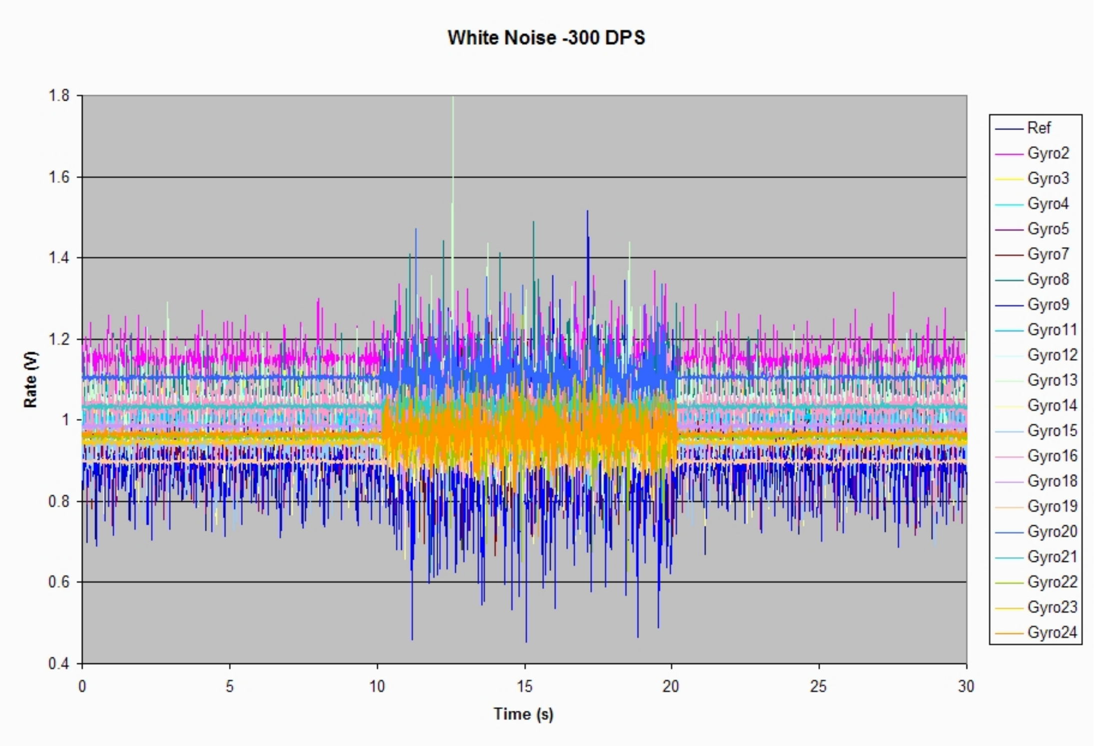

Figure 3.73: White Noise at -300 DPS

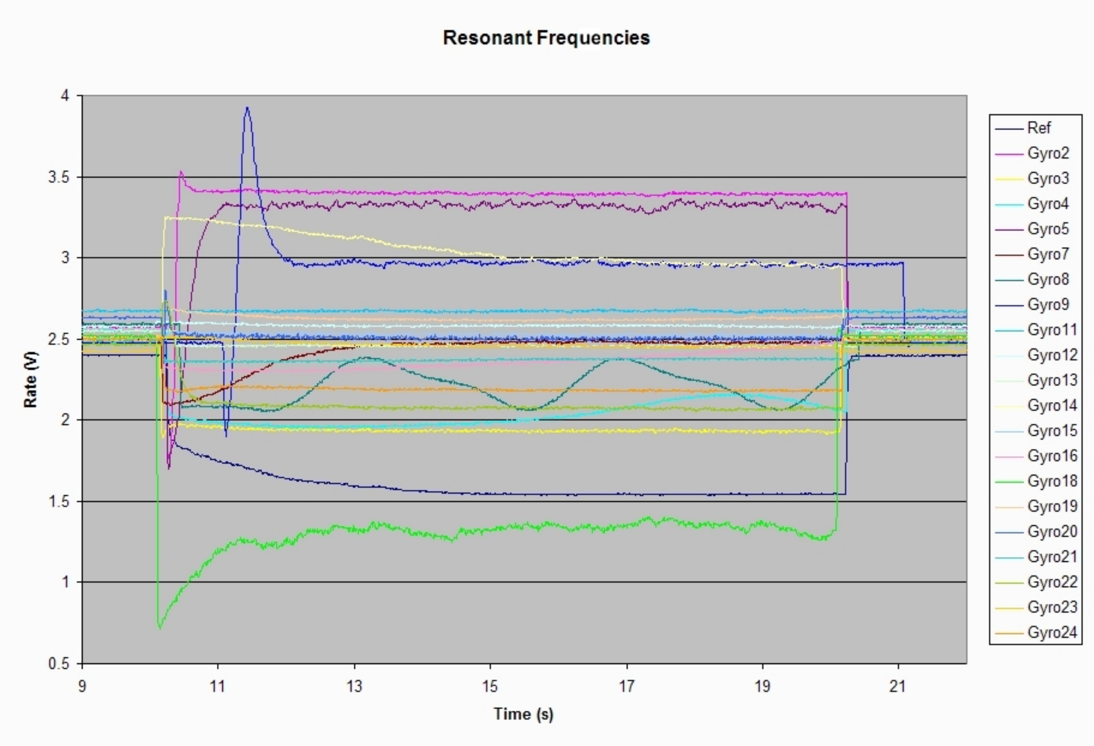

Figure 3.74: Resonant Frequency Response

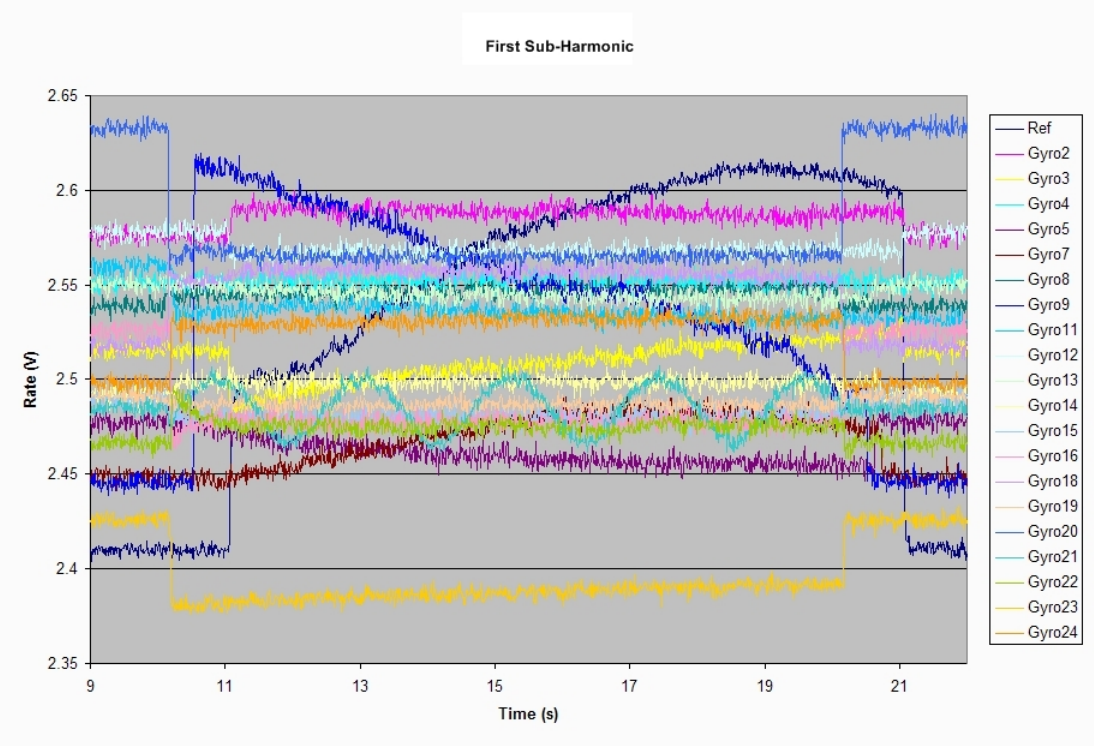

Figure 3.75: First Sub-Harmonics

3.4.7 Sine Sweeps

Fig. 3.76 illustrates each gyro's response to a sine sweep signal. This sine wave is swept from 0 to 20,000 Hz in 5 minutes (300 seconds) at maximum power. Harmonic and resonant frequencies can be seen in detail in this figure.

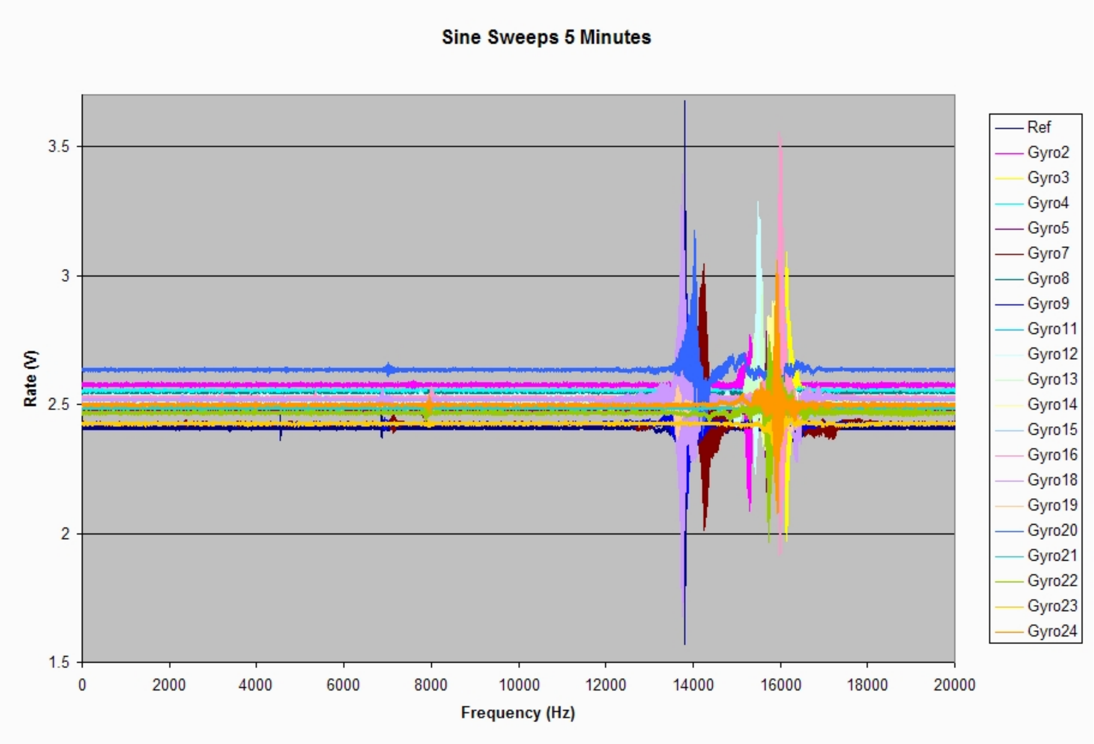

Figure 3.76: Sine sweeps

3.5 Evaluation Data Analysis and Results

This section will provide a statistical analysis of the gyros. Of primary concern will be mean and standard deviation values.

3.5.1 Bias Voltage

Fig. 3.77 describes the bias voltage for each gyro. These are the mean values of the baseline test results. Equ. 3.1 shows the standard deviation of these mean bias voltages. Finally, Fig. 3.78 shows the standard deviation of each gyro's baseline rate output voltage.

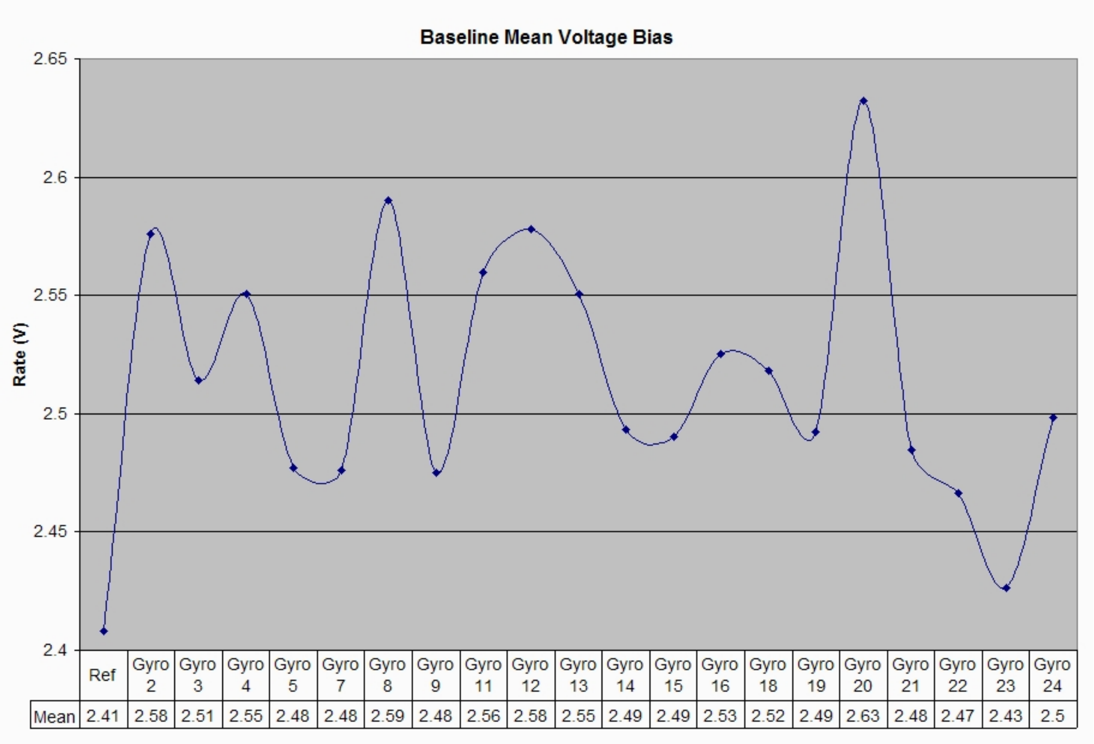

	Ref	Gyro 2	Gyro 3	Gyro 4	Gyro 5	Gyro 7	Gyro 8	Gyro 9	Gyro 11	Gyro 12	Gyro 13	Gyro 14	Gyro 15	Gyro 16	Gyro 18	Gyro 19	Gyro 20	Gyro 21	Gyro 22	Gyro 23	Gyro 24
Mean	2.41	2.58	2.51	2.55	2.48	2.48	2.59	2.48	2.56	2.58	2.55	2.49	2.49	2.53	2.52	2.49	2.63	2.48	2.47	2.43	2.5

Figure 3.77: Baseline mean bias voltages

$$BaselineBiasVoltage : \sigma = 0.055096862 \tag{3.1}$$

3.5.2 No Noise Standard Deviations

In this section, the standard deviations of the rate output voltage of each gyro at various rotation speeds without noise will be presented in Tbl. 3.1 and 3.2.

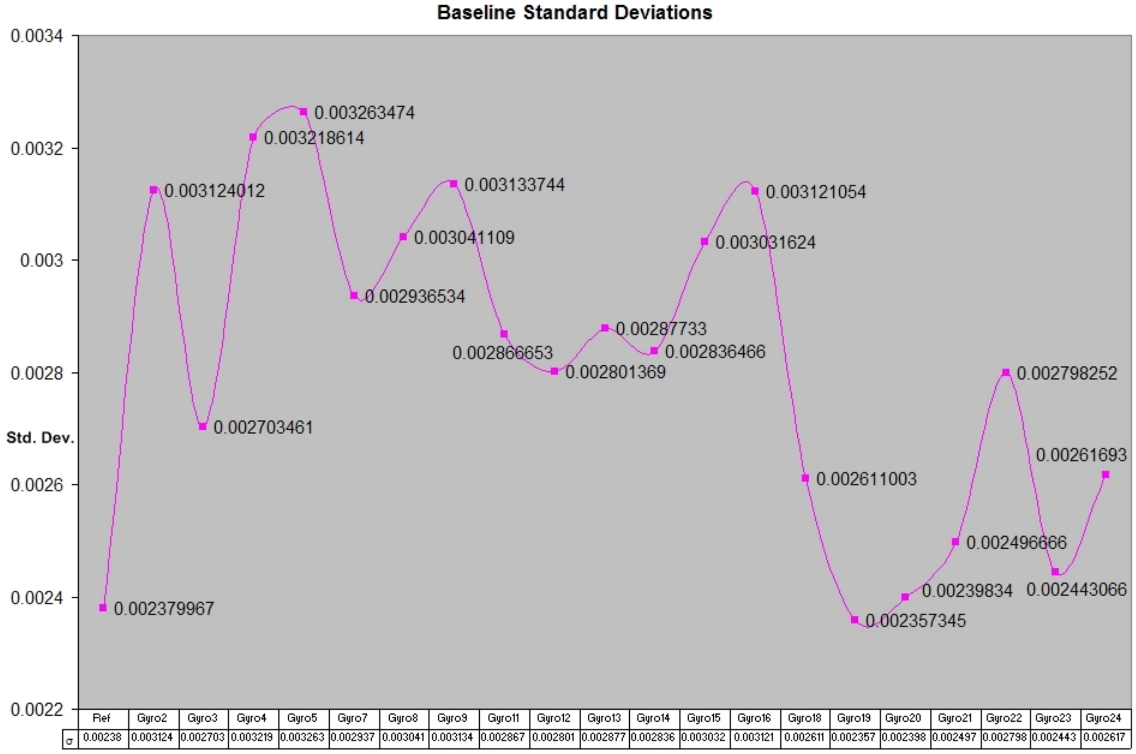

	Ref	Gyro2	Gyro3	Gyro4	Gyro5	Gyro7	Gyro8	Gyro9	Gyro11	Gyro12	Gyro13
σ	0.00238	0.003124	0.002703	0.003219	0.003263	0.002937	0.003041	0.003134	0.002867	0.002801	0.002877

	Gyro14	Gyro15	Gyro16	Gyro18	Gyro19	Gyro20	Gyro21	Gyro22	Gyro23	Gyro24
σ	0.002836	0.003032	0.003121	0.002611	0.002357	0.002398	0.002497	0.002798	0.002443	0.002617

Figure 3.78: Baseline standard deviations of rate output

Gyro	-300	-240	-180	-120	-60	0	60	120
Ref	0.0264	0.0218	0.0212	0.0158	0.0106	0.0025	0.0109	0.0164
2	0.0323	0.0264	0.0252	0.0182	0.0160	0.0032	0.0155	0.0197
3	0.0283	0.0237	0.0235	0.0175	0.0155	0.0028	0.0150	0.0185
4	0.0361	0.0294	0.0285	0.0203	0.0171	0.0033	0.0164	0.0213
5	0.0365	0.0334	0.0314	0.0210	0.0174	0.0033	0.0170	0.0227
7	0.0353	0.0330	0.0286	0.0192	0.0136	0.0028	0.0131	0.0203
8	0.0428	0.0419	0.0354	0.0225	0.0152	0.0030	0.0147	0.0236
9	0.0442	0.0430	0.0393	0.0249	0.0157	0.0031	0.0153	0.0264
11	0.0363	0.0339	0.0280	0.0206	0.0154	0.0030	0.0155	0.0219
12	0.0420	0.0371	0.0332	0.0240	0.0174	0.0031	0.0173	0.0255
13	0.0445	0.0425	0.0356	0.0261	0.0185	0.0033	0.0181	0.0266
14	0.0398	0.0349	0.0327	0.0217	0.0162	0.0029	0.0168	0.0216
15	0.0352	0.0324	0.0297	0.0216	0.0161	0.0031	0.0169	0.0217
16	0.0479	0.0421	0.0391	0.0261	0.0192	0.0032	0.0201	0.0263
18	0.0042	0.0045	0.0044	0.0043	0.0041	0.0027	0.0042	0.0043
19	0.0035	0.0037	0.0035	0.0035	0.0033	0.0024	0.0035	0.0034
20	0.0042	0.0043	0.0044	0.0042	0.0038	0.0025	0.0041	0.0042
21	0.0041	0.0043	0.0043	0.0040	0.0039	0.0025	0.0040	0.0041
22	0.0039	0.0037	0.0038	0.0038	0.0038	0.0029	0.0036	0.0036
23	0.0038	0.0033	0.0036	0.0036	0.0035	0.0025	0.0034	0.0035
24	0.0041	0.0038	0.0040	0.0042	0.0038	0.0027	0.0040	0.0041

Table 3.1: No noise standard deviations

Gyro	180	240	300
Ref	0.0211	0.0301	0.0229
2	0.0246	-	0.0257
3	0.0232	-	0.0245
4	0.0269	-	0.0279
5	0.0291	-	0.0300
7	0.0295	0.0324	0.0305
8	0.0356	0.0390	0.0370
9	0.0380	0.0386	0.0406
11	0.0256	0.0277	0.0335
12	0.0292	0.0297	0.0366
13	0.0335	0.0352	0.0432
14	0.0294	0.0302	0.0348
15	0.0267	0.0285	0.0319
16	0.0354	0.0376	0.0439
18	0.0044	0.0042	0.0038
19	0.0037	0.0035	0.0032
20	0.0042	0.0040	0.0037
21	0.0042	0.0040	0.0038
22	0.0038	0.0036	0.0036
23	0.0033	0.0035	0.0032
24	0.0040	0.0041	0.0035

Table 3.2: No noise standard deviations (cont.)

3.5.3 White Noise

In this section, the standard deviations of the rate output voltage of each gyro while being subjected to white noise at various rotation speeds will be presented in Tbl. 3.3 and 3.4.

Gyro	-300	-240	-180	-120	-60	0	60	120
Ref	0.0413	0.0442	0.0439	0.0367	0.0424	0.0111	0.0397	0.0450
2	0.0571	0.0610	0.0600	0.0549	0.0518	0.0418	0.0495	0.0534
3	0.0455	0.0458	0.0422	0.0404	0.0390	0.0641	0.0378	0.0427
4	0.0400	0.0373	0.0329	0.0270	0.0266	0.0108	0.0230	0.0285
5	0.0446	0.0422	0.0385	0.0307	0.0313	0.0261	0.0296	0.0312
7	0.0743	0.0681	0.0724	0.0676	0.0702	0.0481	0.0663	0.0677
8	0.0973	0.0899	0.0905	0.0872	0.0722	0.0748	0.0720	0.0805
9	0.1242	0.1304	0.1166	0.1046	0.1166	0.1376	0.1078	0.1116
11	0.0499	0.0505	0.0445	0.0429	0.0421	0.0126	0.0406	0.0374
12	0.0522	0.0512	0.0444	0.0408	0.0385	0.0231	0.0316	0.0382
13	0.0959	0.0885	0.0838	0.0758	0.0749	0.0260	0.0792	0.0716
14	0.0579	0.0577	0.0502	0.0428	0.0455	0.0569	0.0427	0.0459
15	0.0481	0.0449	0.0368	0.0366	0.0292	0.0174	0.0315	0.0354
16	0.0735	0.0683	0.0634	0.0541	0.0511	0.0554	0.0566	0.0608
18	0.0712	0.0678	0.0721	0.0731	0.0727	0.1227	0.0711	0.0763
19	0.0114	0.0116	0.0113	0.0121	0.0111	0.0098	0.0108	0.0131
20	0.0558	0.0548	0.0514	0.0594	0.0568	0.0988	0.0589	0.0491
21	0.0193	0.0204	0.0187	0.0197	0.0217	0.0215	0.0191	0.0207
22	0.0556	0.0535	0.0571	0.0607	0.0554	0.0396	0.0537	0.0545
23	0.0202	0.0218	0.0208	0.0206	0.0205	0.0124	0.0215	0.0187
24	0.0547	0.0548	0.0546	0.0508	0.0602	0.0470	0.0561	0.0529

Table 3.3: White noise standard deviations

3.5.4 Resonant Frequencies

Fig. 3.79 lists the resonant frequencies of each gyro. Equ. 3.2 shows the standard deviation of those frequencies.

Gyro	180	240	300
Ref	0.0447	0.0678	0.0397
2	0.0513	-	0.0594
3	0.0467	-	0.0460
4	0.0341	-	0.0373
5	0.0366	-	0.0404
7	0.0692	0.0746	0.0727
8	0.0916	0.0822	0.0878
9	0.1177	0.1224	0.1004
11	0.0466	0.0476	0.0503
12	0.0450	0.0467	0.0500
13	0.0786	0.0867	0.0882
14	0.0525	0.0544	0.0489
15	0.0422	0.0430	0.0452
16	0.0651	0.0668	0.0674
18	0.0690	0.0641	0.0707
19	0.0111	0.0101	0.0114
20	0.0576	0.0539	0.0488
21	0.0216	0.0203	0.0208
22	0.0523	0.0549	0.0577
23	0.0224	0.0197	0.0191
24	0.0594	0.0520	0.0542

Table 3.4: White noise standard deviations (cont.)

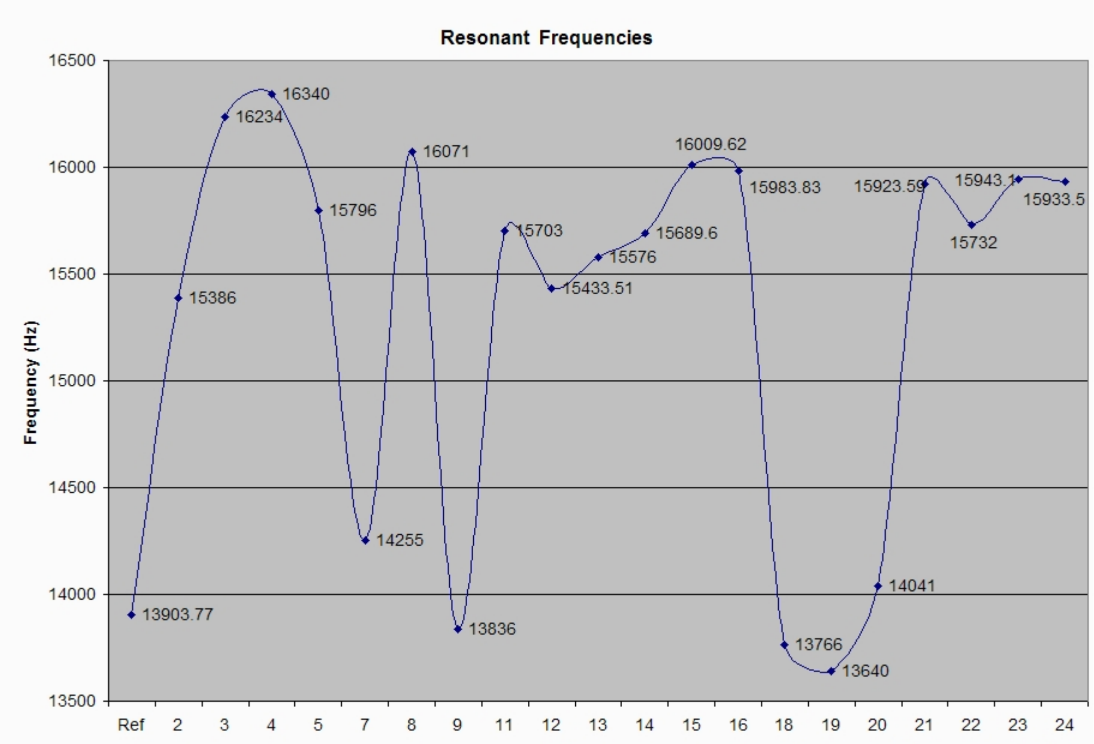

Figure 3.79: Resonant frequencies of each gyro

$$ResonantFrequencies : \sigma = 934.0686737 \tag{3.2}$$

3.5.5 First Sub-Harmonics

Fig. 3.80 lists the first sub-harmonic frequencies of each gyro. Equ. 3.3 shows the standard deviation of those frequencies.

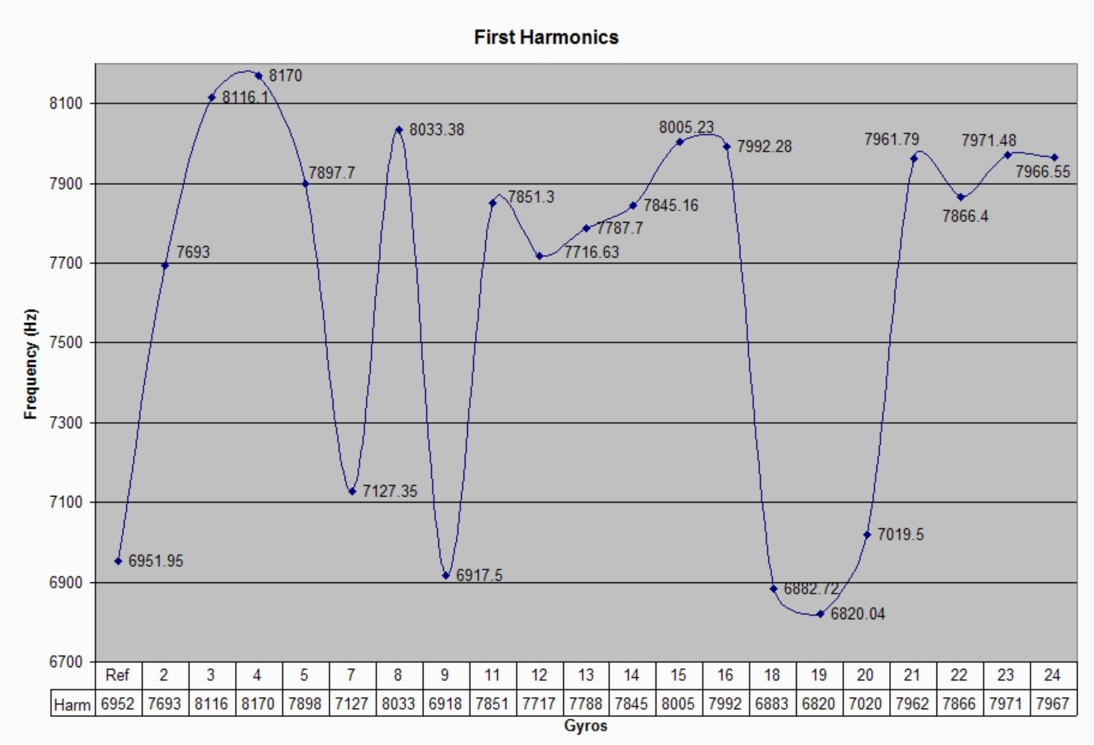

	Ref	2	3	4	5	7	8	9	11	12	13	14	15	16	18	19	20	21	22	23	24
Harm	6952	7693	8116	8170	7898	7127	8033	6918	7851	7717	7788	7845	8005	7992	6883	6820	7020	7962	7866	7971	7967

Figure 3.80: First sub-harmonic frequencies of each gyro

$$FirstSubHarmonicFrequencies : \sigma = 467.0496657 \tag{3.3}$$

CHAPTER 4

CONCLUSIONS

In this section, the following questions, first stated in Section 3.2, will addressed:

1. Is the frequency or amplitude of the sine wave in the output signal sound level dependent?
2. How close above and below the resonant frequency of the sensor does this occur?
3. Does it occur at the two other minor resonant frequencies?
4. What happens if a two-tone signal is applied, where one tone is above and one below the resonant frequency?
5. Does a single tone far away from the resonant frequencies have any effect on the gyro output at any realistic sound power level?
6. What is the probability distribution of the natural frequency for the gyros tested?
7. Does the standard deviation of the output rate increase in proportion to the applied angular rate?

Fig. 3.52 provides the answer to Question 1. Based on the data acquired from the reference gyro, a gyro's output will be sinusoidal when subjected to a single tone near its resonant frequency. It is seen that as the SPL's increase, the amplitude of the gyro's output increases linearly. In fact, the rate at which it increases is 0.0026 V/dB (0.0052 Vpp/dB).

The output frequency, on the other hand, is not affected at all. The reference gyro's gathered data shows that the output frequency is a function of the frequency of the ambient noise.

Question 2 can be answered by referring to Fig. 3.76. In this figure, it can be seen exactly when each gyro's output starts to become affected by a single high-pressure tone. As the tone frequency nears the resonant frequency, the gyros' output become increasingly erratic at an exponential rate. In general, the gyros are dramatically affected within 1 kHz of its resonant frequency. Slight sinusoidal tendencies can be seen as far away as 3 kHz.

The answer to Question 3 is "yes." Examining the first sub-harmonic plots will reveal that the other minor frequencies are indeed affected by noise near this frequency. Please refer to Figs. 3.76 and 3.75.

Question 4 is answered by examining the reference gyro output. As two tones equidistant from its resonant frequency become closer, the gyro's output begins to behave as in Figs. 3.53 to Fig. 3.61.

Once again, the Question 5 can be illuminated by Fig. 3.76. Even at maximum SPL's there are certain frequencies which have no discernible impact on the gyros' output. Namely, these frequencies exist well outside their resonant and harmonic frequencies.

In order to answer Question 6, we examine Fig. 4.1 which shows, Fig. 4.1 shows the normal distribution (Gaussian) of the natural frequencies of the tested gyros. The graph concisely shows the probabilities of the various natural frequencies centered around 15.3 kHz, the mean natural frequency of the gyros. This typical range of frequency values fluctuates significantly from the manufacturer's stated nominal 14 kHz resonating frequency of each ADXRS300 MEMS gyro [28].

Question 7 is answered by examining the data in Fig. 4.2. The graph shows the output rate standard deviation of each gyro as the angular rate increases from 0 to 300 degrees per second. Curiously, there seems to be two trends amongst the gyros. Groups A through D experience relatively linear increases in standard deviation as the angular rate increases.

However, Groups E and F show little change in their standard deviations by comparison. By examining Figs. 3.63 through 3.68, the "no sound" output levels of groups E and F at the various angular rates remain somewhat constant throughout. The other groups, however, show a trend of increasing standard deviations. Evidently, there is some variation in the output rate standard deviations between each gyro grouping. As to the question, Fig. 4.2 and 4.3 seem to affirm that indeed the standard deviation of the output rate of each gyro increases in proportion to the applied angular rate, however, by varying amounts.

Finally, Table 4.1 shows the typical response of the gyros as they are subjected to acoustic noise. The "baseline" value represents the standard deviation of the gyros' rate output voltages while stationary and without noise. The "white noise 0 DPS" value represents the the gyros' standard deviations while stationary but in the presence of white noise. Therefore, the "factor" value illustrates how the presence of high power white noise can affect the rate output voltage by various magnitudes. The table shows that standard deviations can increase by a factor of 3 to 44 by applying high power white noise to a working ADXRS300 MEMS gyro. This noise level could make the device unusable in this environment. The effects are even more dramatic for frequencies near each gyro's natural frequency. In fact, for these frequencies the gyros become quite useless as the output voltages begin to swing wildly rendering the typical response of each gyro's reported rate value to be inaccurate and unstable. So, in summary, a MEMS gyro's rate output voltage is adversely affected by high-frequency acoustic noise and responds typically as shown throughout the data presented in this thesis.

Gyro	Baseline	White Noise 0 DPS	Factor
Ref	0.002379967	0.011107925	4.667260644
2	0.003124012	0.041399207	13.25193704
3	0.002703461	0.063574897	23.51611362
4	0.003218614	0.010999183	3.417366751
5	0.003263474	0.025725922	7.882986219
7	0.002936534	0.047046402	16.02106444
8	0.003041109	0.076378647	25.11539056
9	0.003133744	0.139176035	44.4120594
11	0.002866653	0.01266741	4.41888532
12	0.002801369	0.023007011	8.212774079
13	0.00287733	0.025415162	8.832898624
14	0.002836466	0.055376522	19.52306744
15	0.003031624	0.017602752	5.806376995
16	0.003121054	0.055384876	17.74556995
18	0.002611003	0.123223407	47.19389924
19	0.002357345	0.009739161	4.131411633
20	0.00239834	0.097153155	40.50849104
21	0.002496666	0.021466124	8.597914718
22	0.002798252	0.038315134	13.69252357
23	0.002443066	0.012001517	4.91248101
24	0.00261693	0.045410077	17.35242405

Table 4.1: Comparison of standard deviations between baseline and white noise

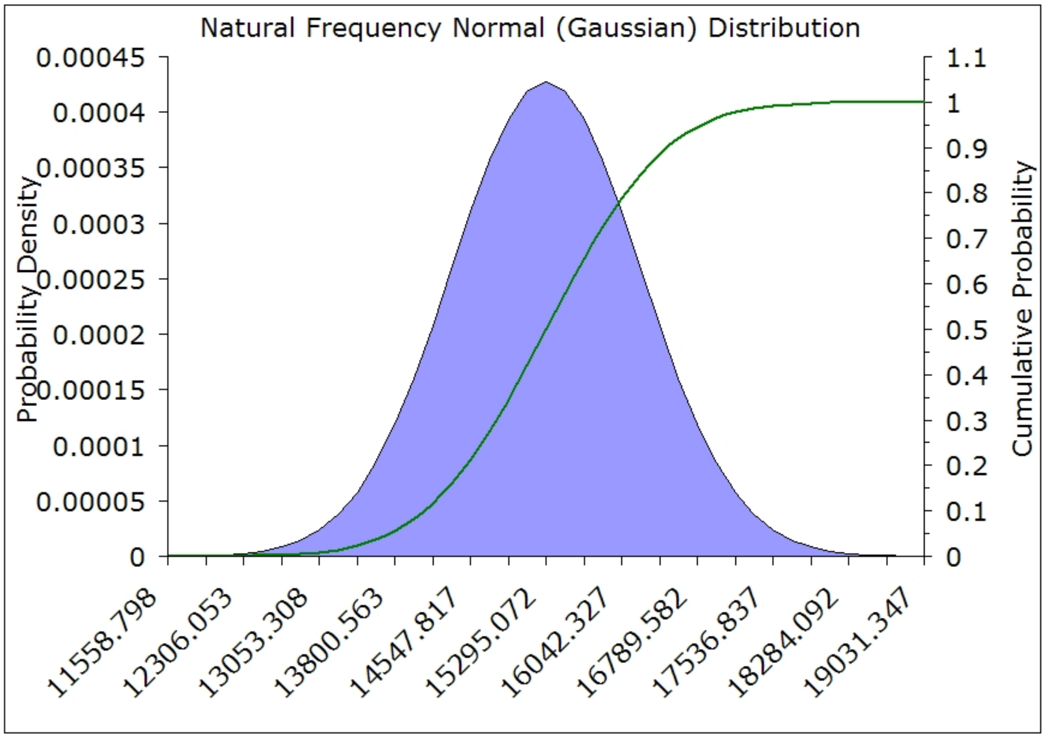

Figure 4.1: Natural frequency normal distribution

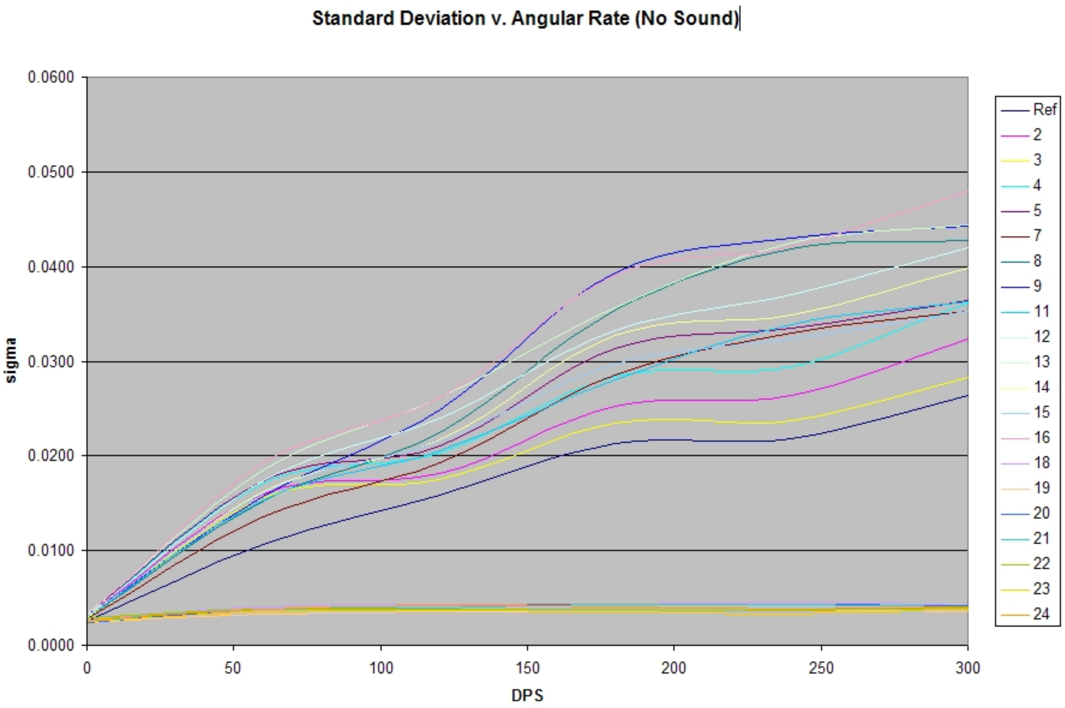

Figure 4.2: Standard deviation of gyros at increasing angular rates

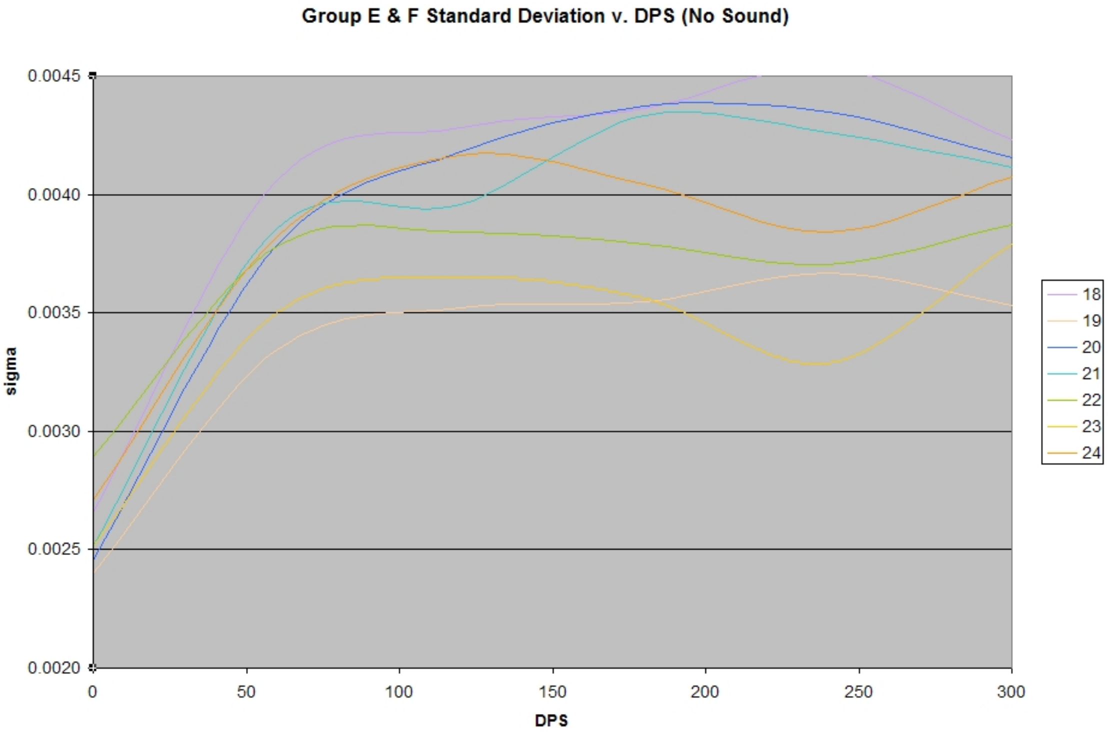

Figure 4.3: Standard deviation of groups E and F at increasing angular rates

CHAPTER 5

FUTURE WORK

In the future, the main goal of this research is to develop and understand methods for negating the affects of acoustic noise on MEMS gyros. This may be done through packaging or design. Sufficiently high natural frequencies designed well above the acoustic spectrum or high frequency shielding could both potentially be used to achieve this.

BIBLIOGRAPHY

[1] http://www.memsindustrygroup.org/.

[2] *Gyros, Platforms, and Accelerometers*, Little Falls: The Singer Company, 1967.

[3] V. E. Johnson, *The Gyroscope*, London: E. and F. N. Spon, 1911.

[4] R. F. Deimel, *Mechanics of the Gyroscope*, USA: Dover Publications, 1950.

[5] J. B. Scarborough, *The Gyroscope Theory and Applications*, New York: Interscience Publishers, 1958.

[6] P. C. Muller, *Special Problems of Gyrodynamics*, New York: Udine, 1970.

[7] F. C. Roan, *Phase Stabilization of a Gyro Blender Using RC Commutated Networks*, Auburn: Auburn University,1965.

[8] K. Magnus, *Gyrodynamics*, New York: Udine, 1970.

[9] P. Y. Willems, *Gyrodynamics*, New York: Springer-Verlag, 1974.

[10] A. Gray, *A Treatise on Gyrostatics and Rotational Motion*, New York: Dover Publications, 1959.

[11] R. N. Arnold and L. Maunder, *Gyrodynamics and Its Engineering Applications*, New York: Academic Press, 1961.

[12] G. Greenhill, *Gyroscopic Theory*, New York: Chelsea Publishing Company, 1966.

[13] S. Beeby, G. Ensell, M. Kraft and N. White, *MEMS Mechanical Sensors*, Boston: Artech House, 2004.

[14] N. Maluf, K. Williams, *An Introduction to Microelectromechanical Systems Engineering*, Boston: Artech House, 2004.

[15] J. J. Allen, *Microelectromechanical System Design*, Boca Raton: Taylor and Francis, 2005.

[16] S. Nasiri, "A Critical Review of MEMS Gyroscopes Technology and Commercialization Status," InvenSense.

[17] "Angular Rate Sensors for Roll-Over Applications - SMG040," Robert Bosch GmbH SMG040 Datasheet, 2006.

[18] "Silicon Sensing MEMS angular rate sensors, CRG20 and CRS09," Electronics Weekly, RBI Limited, 2008.

[19] http://www.systron.com/.

[20] http://www.melexis.com/.

[21] "InvenSense IDG-600 Motion Sensing Solution Showcased in Nintendo'S New Wii MotionPlus," Thomson Reuters Press Release, 2008.

[22] http://www.honeywell.com/.

[23] "ADXRS610 300o/sec yaw rate gyro, Analog Devices Data Sheet," D06520-0-4/07(0), 2007, (12pp).

[24] http://www.northropgrumman.com/.

[25] R. Dean, G. Flowers, A. Ahmed, A. Hodel, G. Roth, S. Castro, R. Zhou, R. Rifki, A. Moreira, B. Grantham, D. Bittle and J. Brunsch, "On the Degradation of MEMS Gyroscope Performance in the Presence of High Power Acoustic Noise," Proc. of the 2007 IEEE Int. Symposium on Industrial Electronics (ISIE 2007), Vigo, Spain, June 4-7, 2007, pp. 1435-1440.

[26] http://www.gyro.ru/.

[27] R. Dean, G. Flowers, and S. Castro, "Recent Developments in MEMS Gyroscopic Sensor Technology," ABR Manuscript, Dynetics, 2007.

[28] "ADXRS300 300o/sec yaw rate gyro, Analog Devices Data Sheet," C0322603/04(B), 2004, (12pp).

[29] T. Braman and M. Grossman, "Designing Vibration and Shock Isolation Systems for Micro Electrical Machined Based Inertial Measurement Units," Honeywell Int.: Minneapolis, Minnesota.

[30] M. S. Weinberg and A. Kourepenis, "Error Sources in In-Plane Silicon Tuning-Fork MEMS Gyroscopes," Journal of Microelectromechanical Systems, Vol. 15, No. 3, June 2006.

[31] J. Green and D. Krakauer, "New iMEMS Angular-Rate-Sensing Gyroscope," ADI Micromachined Products Division.

[32] M. Weber, M. Bellrichard, and C. Kennedy, "High Angular Rate and High G Effects in the MEMS Gyro," Honeywell: Minneapolis, Minnesota. Coventor: Cary, North Carolina.

[33] http://www.aerotech.com/.

[34] http://www.loudspeakers.net/.

[35] http://www.crownaudio.com/.

[36] http://www.ni.com/.

[37] http://www.endevco.com/.

APPENDICES

APPENDIX A

MATLAB NOISE GENERATION CODE

```
%---------------------------------------------------------
clear
clc
%---------------------------------------------------------

%---------------------------------------------------------
F1=13000;   %Low Limit Frequency
F2=18000;   %High Limit Frequncy
time=10;    %Duration Of Signal
%---------------------------------------------------------

%---------------------------------------------------------
rate=44100;
rate_adj = time*rate;
white = randn(1,rate_adj);
W1 = 2*F1/rate;
W2 = 2*F2/rate;
Wn = [W1 W2];
[B,A] = butter(19, Wn);
wideband = filter(B,A,white);
sound(white,rate_adj/time);
%---------------------------------------------------------
```

APPENDIX B

DATA COLLECTION CODE

```
; AutoHotkey Version: 1.x
; Language:       English
; Platform:       Win9x/NT
; Authors:        S. T. Castro & G. Roth
;
; Script Function:
; Template script (you can customize this template by editing
; "ShellNew\Template.ahk" in your Windows folder)

#NoEnv
; Recommended for performance and compatibility
; with future AutoHotkey releases.
SendMode Input
; Recommended for new scripts due to its
; superior speed and reliability.
SetWorkingDir %A_ScriptDir%
; Ensures a consistent starting directory.

^!g::

WinWait, Microsoft Excel,
IfWinNotActive, Microsoft Excel, , WinActivate, Microsoft Excel,
WinWaitActive, Microsoft Excel,
Send, ^{HOME}{SHIFTDOWN}{DOWN 20}{CTRLDOWN}{RIGHT}{CTRLUP}{SHIFTUP}
Send, !ed
Send, {RIGHT 6}{SHIFTDOWN}^{DOWN}{SHIFTUP}
Send, !ed
Send, {HOME}{SHIFTDOWN}{CTRLDOWN}{DOWN}{RIGHT}{SHIFTUP}{CTRLUP}
Send, {ALTDOWN}i{ALTUP}h
WinWait, Chart Wizard - Step 1 of 4 - Chart Type,
IfWinNotActive, Chart Wizard - Step 1 of 4 - Chart Type, ,
WinActivate, Chart Wizard - Step 1 of 4 - Chart Type,
```

```
WinWaitActive, Chart Wizard - Step 1 of 4 - Chart Type,
Send, {DOWN 4}{TAB}{DOWN}{RIGHT}{ENTER 4}
return

^!1::

WinWait, NCH Tone Generator
WinActivate, NCH Tone Generator
WinWaitActive, NCH Tone Generator
Send, !t{DOWN 5}{ENTER}
Sleep 100
Send, {DOWN 3}{ENTER}10000{ENTER}
WinActivate, Gyros.vi
Send, ^r
Sleep 10000
WinActivate, NCH Tone Generator
Send, {F9}
Return

^!2::

WinWait, NCH Tone Generator
WinActivate, NCH Tone Generator
WinWaitActive, NCH Tone Generator
Send, !t{DOWN 5}{ENTER}
Sleep 100
Send, {DOWN 5}{ENTER}10000{ENTER}
WinActivate, Gyros.vi
Send, ^r
Sleep 10000
WinActivate, NCH Tone Generator
Send, {F9}
Return

^!l::

WinWait, NCH Tone Generator
WinActivate, NCH Tone Generator
WinWaitActive, NCH Tone Generator
Send, !t{DOWN 6}{ENTER}
Sleep 100
Send, {DOWN 4}{ENTER}300000{ENTER}
```

```
WinActivate, Gyros.vi
Send, ^r
WinActivate, NCH Tone Generator
Send, {F9}
Return

^!s::

WinWait, NCH Tone Generator
WinActivate, NCH Tone Generator
WinWaitActive, NCH Tone Generator
Send, !t{DOWN 6}{ENTER}{DOWN 4}{ENTER}30000{ENTER}
WinActivate, Gyros.vi
Send, ^r
WinActivate, NCH Tone Generator
Send, {F9}
Return

^!w::

WinWait, NCH Tone Generator
WinActivate, NCH Tone Generator
WinWaitActive, NCH Tone Generator
Send, !tw{DOWN}{ENTER}10000{ENTER}
WinActivate, Gyros.vi
Send, ^r
Sleep 10000
WinActivate, NCH Tone Generator
Send, {F9}
Return

^!p::

WinWait, NCH Tone Generator
WinActivate, NCH Tone Generator
WinWaitActive, NCH Tone Generator
Send, !t{DOWN 5}{ENTER}
Send, {F9}
SoundSet, 0, MASTER
WinActivate, Gyros.vi
Send, ^r
```

```
Loop, 100
{

   Sleep, 1000
   SoundSet, +1, MASTER

}

SoundSet, 100, MASTER

Return
```

APPENDIX C

GYROS TO NI DAQ SCHEMATIC

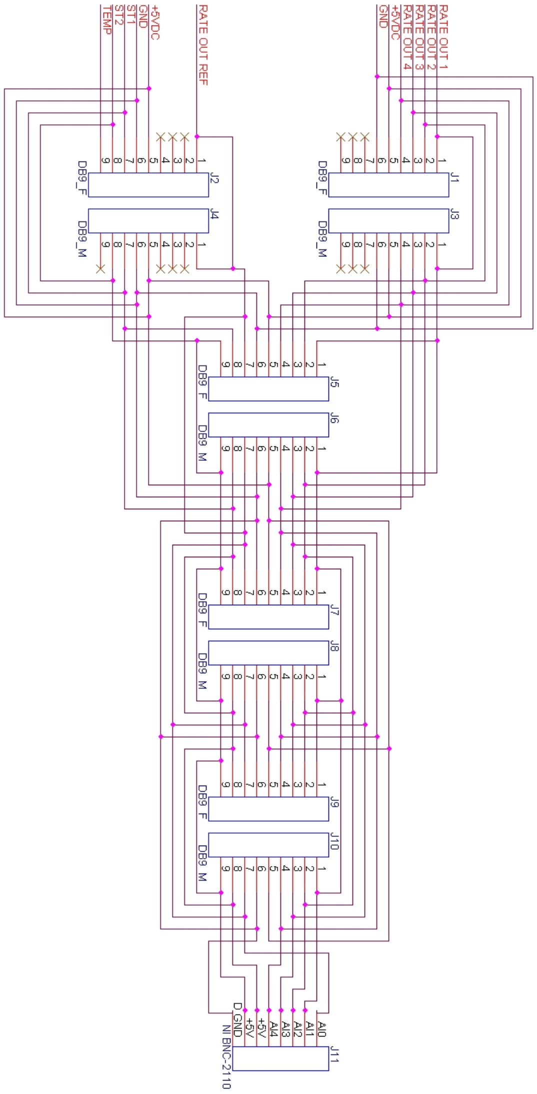

Figure C.1: Wiring diagram for gyros to NI BNC-2110

APPENDIX D

LABVIEW BLOCK DIAGRAMS

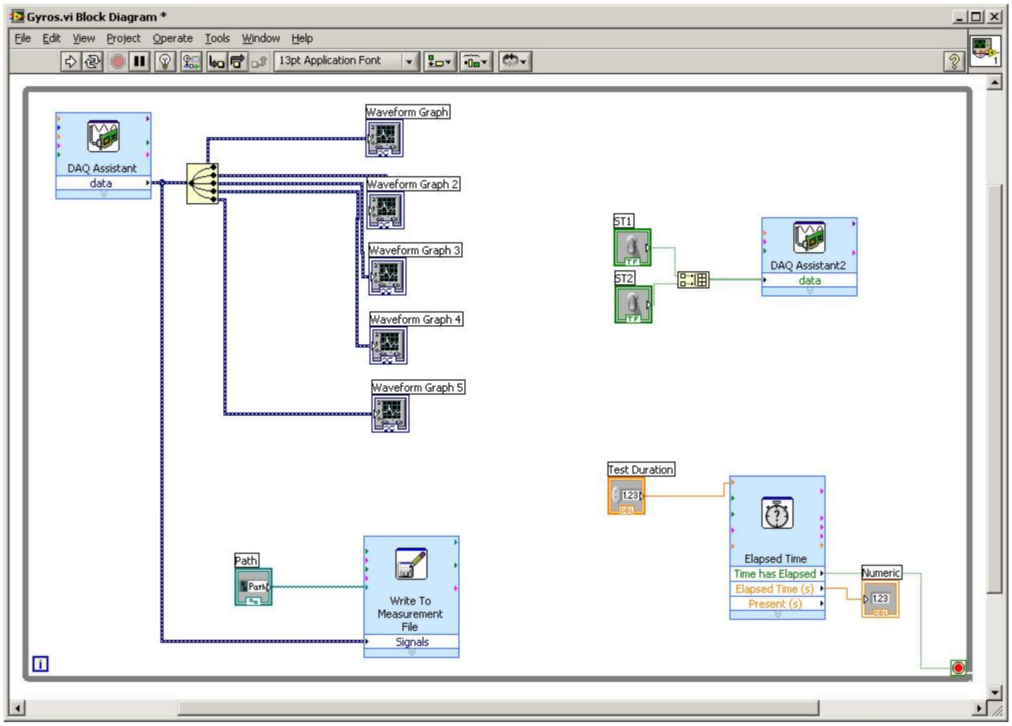

Figure D.1: Gyros.vi block diagram

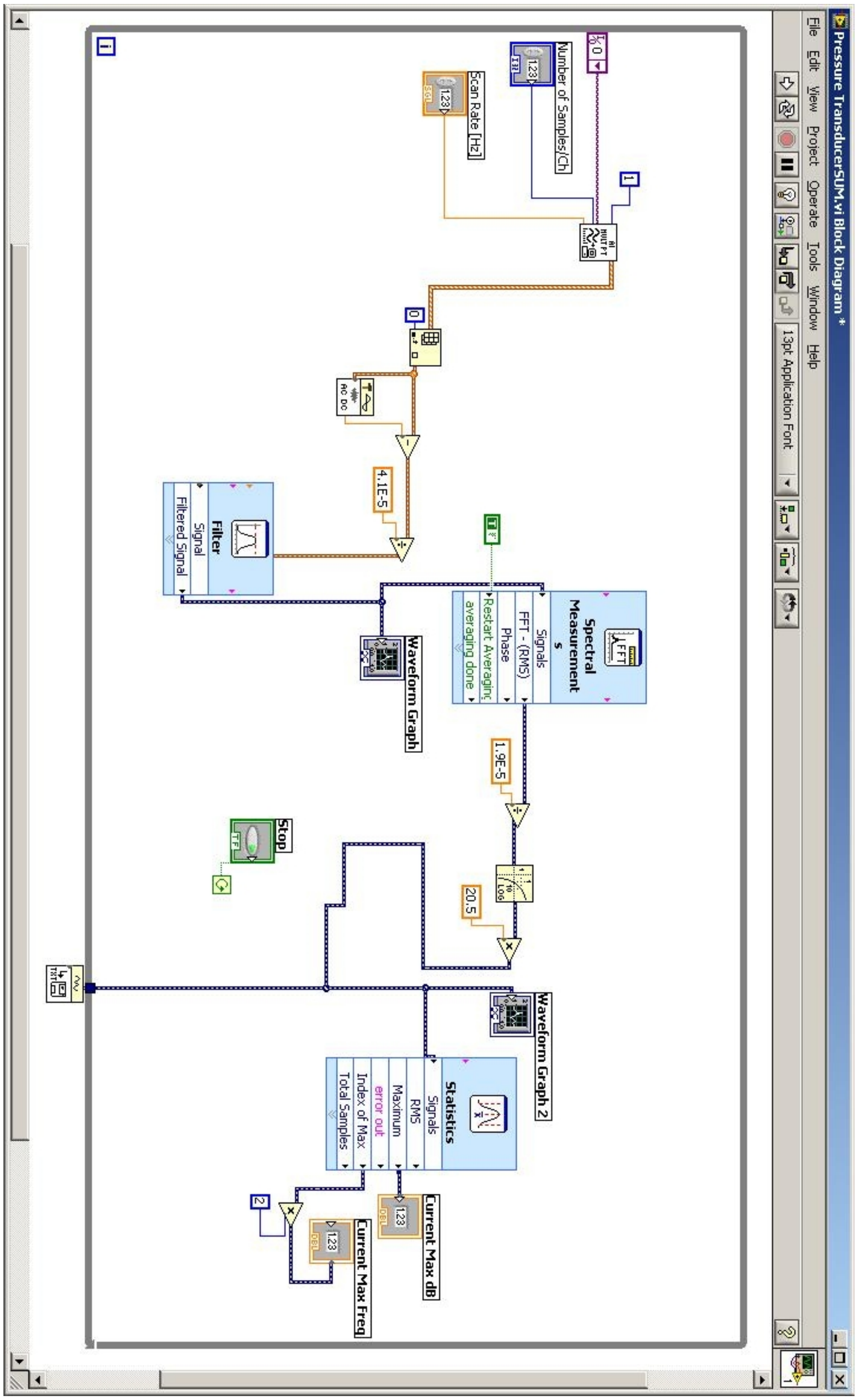

Figure D.2: Gyros.vi block diagram